Seismic structure of the crust and the uppermost mantle beneath Kyushu, Japan, as derived from receiver function analyses:

Implications for volcanic processes

Yuki Abe

Abstract

Receiver function analyses are performed for understanding the processes of volcanic activity in Kyushu, Japan.

We develop a new method to estimate geometries of dipping seismic velocity discontinuities from common conversion point stacking of receiver function and apply the method to detect discontinuities in the uppermost mantle beneath the Kyushu subdution zone. The multistage fast-marching method is applied to the ray tracing with taking account of refraction at dipping interfaces. We apply this method to synthetic data and confirm that geometries of dipping interfaces are successfully estimated. Although geometry of interfaces dipping at 30-70º cannot be correctly estimated with a 1-d velocity model, it can be correctly estimated when refraction at dipping interfaces is taken into account. The Philippine Sea slab subducting beneath Kyushu is young (26-50 Ma) and steeply dipping (at greater than 30º). We detect a seismic velocity contrast larger than 10% corresponding to the oceanic Moho down to 70-90 km in depth, implying that the subducting oceanic crust contains more than 3.0 wt.% of water down to this depth. We delineate the continental Moho with downward decreasing seismic velocity and the upper boundary of the slab with upward decreasing seismic velocity beneath the forearc region, implying the existence of serpentinite and/or free fluid which causes high pore pressure in the forearc mantle. Beneath the central Kyushu region, we also detect a discontinuity with downward decreasing seismic velocity at depths of 60-80 km, which is parallel to the oceanic Moho and 10 km shallower than it. This finding indicates that there is a sharp discontinuity between the anhydrous mantle wedge and the hydrous oceanic crust. The existence of such a sharp discontinuity would

require a large temperature gradient around the boundary or a permeability barrier at the upper boundary of the slab.

Aso Volcano experienced a huge pyroclastic eruption 90 thousand years ago, and formed a large caldera (18 km × 25 km). In order to examine the hypothesis of a magma body in the mid and lower crust that has been suggested geophysically and geochemically, we set seismic stations in Aso caldera and investigated the velocity structure beneath Aso caldera with a genetic algorithm inversion of receiver functions from the observed data. As a result, we detect a low velocity layer with S-wave velocity of 2.5 km/s at depths between 15 km and 20 km beneath the western and the northern parts of the caldera. We estimate that the low velocity layer contains at most 15 percent melt or 30 percent aqueous fluid. Fluid contained in the layer might be related to huge pyroclastic eruptions of Aso volcano.

Contents

I. General Introduction

Kyushu island is located on the eastern margin of the Eurasian plate, and the Philippine Sea (PHS) plate is west-northwesterly subducting at a rate of 5 cm/year beneath Kyushu [*Seno et al.,* 1993]. The distribution of intermediate-depth earthquakes shows that the PHS slab subducts down to 70-90 km in depth at dip angles of 30-40º, and extends from this depth down to 150-250 km at dip angles of greater than 65º. The PHS slab subducting beneath Kyushu is separated into two parts by a remnant island arc, the Kyushu-Palau ridge, and the ages of the north and south portions are estimated to be 26 Ma and 50 Ma, respectively [*Hilde and Lee,* 1984; *Okino et al.,* 1994] (Figure 1). In Kyushu, there are active volcanoes in the backarc region and on a volcanic front which transects in a NNE-SSW direction, subparallel to the isodepth lines of Wadati-Benioff zone. Many of the volcanoes have a large caldera (e.g. Aira, Aso, Chijiwa, Kakuto).

The processes of volcanic activity, where and how magma is generated, conveyed and accumulated in Kyushu, is still controversial. A purpose of studies in this thesis is to examine the crustal structure and the uppermost mantle structure with receiver function analyses, and contribute to revealing the processes.

Arc volcanism is interpreted to be caused by fluid dehydrated from the subducting oceanic crust [e.g. *Tatsumi,* 1986; *Iwamori,* 2007]. *Nakada and Kamata* [1991] analyzed chemical compositions of basalts of the northern part of Kyushu and interpreted that the basalt from Kuju is generated in the mantle contaminated by slab-derived materials. *Miyoshi et al.* [2008] revealed that basaltic rocks from volcanoes on the volcanic front in Kyushu have abundant boron content, and interpreted that the basaltic rocks are contaminated by fluid dehydrated from the subducting oceanic

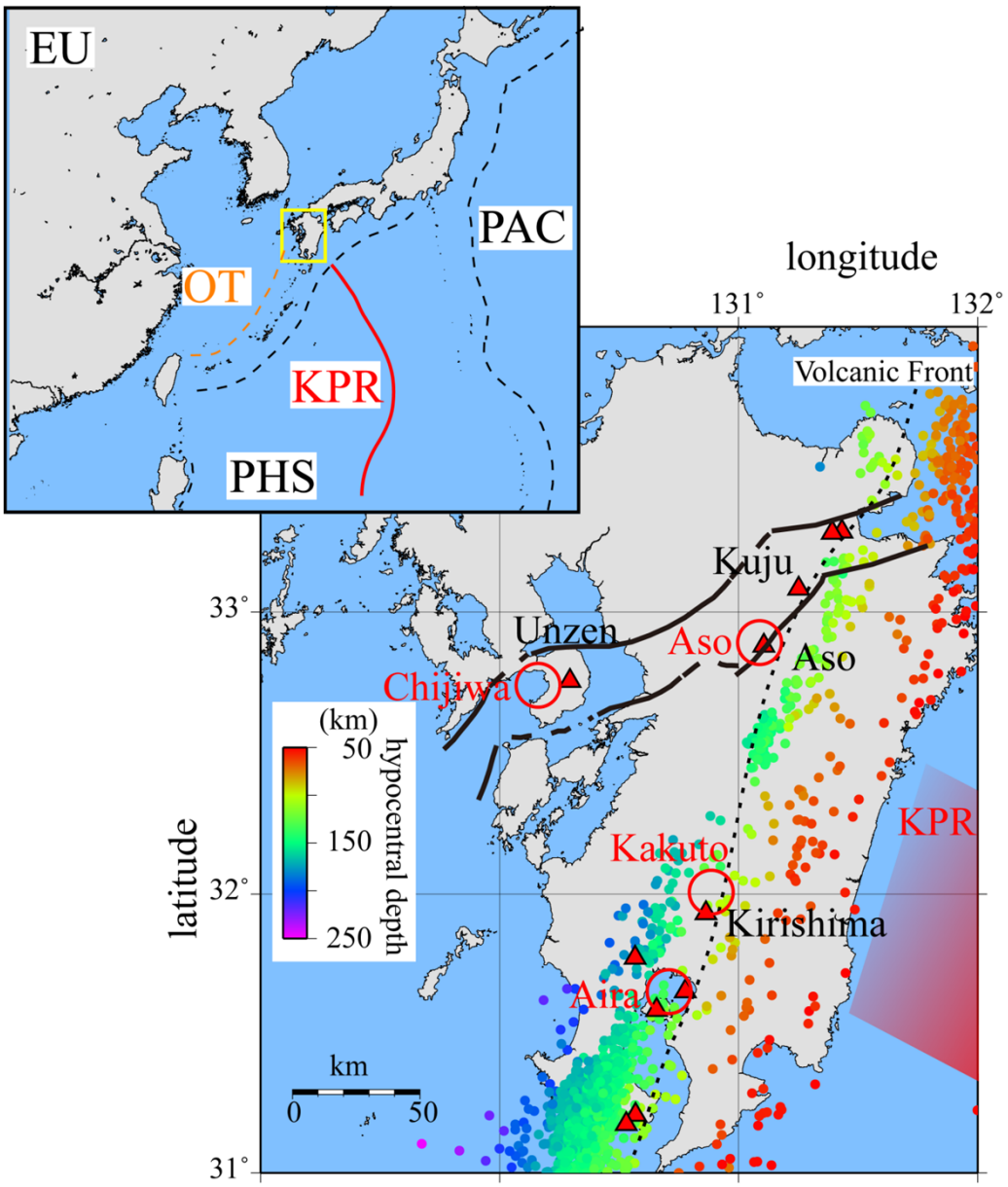

Figure 1 The top-left insert map shows the tectonic environment around the investigated region; EU: Eurasian plate, PHS: Philippine Sea plate, PAC: Pacific plate, KPR: the Kyushu-Palau ridge, OT: Okinawa trough. The yellow box indicates the area shown in the map in the map of Kyushu island. The bottom-right panel shows map of Kyushu. The dotted line indicates the volcanic front. The red shaded region indicates the location of the oceanic crust with heterogeneous velocity structure corresponding to the Kyushu-Palau ridge detected by *Tahara et al.* [2008]. Colored circles indicate hypocenter location detected by Japan Meteorological Agency (JMA); focal depths are deeper than 50 km and indicated with the color bar; magnitudes are greater than 2; origin times are from Oct. 1997 to Mar. 2007. Black solid and dashed lines indicate boundaries of Beppu-Shimabara graben defined by *Matsumoto et al.* [1979].

sediments. Therefore, fluid dehydrated from the subducting slab would have some relationships with volcanism in Kyushu. However, *Nakada and Kamata* [1991] interpreted that basalt from Unzen is not contaminated by slab-derived materials. *Tada* [1993] interpreted the Beppu-Shimabara graben [*Matsumoto*, 1979] as a rift valley stretching N-S direction, on the basis of the crustal deformation of Kyushu island from 1885 to 1985 and gravity anomaly in the Shimabara peninsula. *Yoshida and Seno* [1992] also interpreted that volcanic activity along the Beppu-Shimabara graben is caused by rifting. Therefore, volcanic activity along the graben might be caused by ascending of mantle itself.

Although the processes of magma generation in Kyushu are still unknown, magma would be generated in the mantle and ascend to the continental crust. In northeastern Japan, *Nakajima et al.* [2001] estimated with seismic tomography the velocity structure of the mantle wedge, and detected a low velocity region which is interpreted to be a pathway of fluid or melt to the continental crust. However, *Wang and Zhao* [2006] estimated with seismic tomography the velocity structure of the uppermost mantle beneath Kyushu, and revealed that the velocity distribution is heterogeneous. Pathways of melt and fluid in the mantle wedge beneath Kyushu have not been revealed.

Magma would be accumulated somewhere in the crust or the uppermost mantle before eruption. In Kyushu, there are several calderas, which are interpreted to be depressions formed by ejection of large volume of material. *Petford et al.* [2000] and *Takahashi* [2008] indicated that such a large eruption is caused by magma generated from the partially molten crust. *Kaneko et al.* [2008] analyzed trace element of volcanic rocks of Aso volcano and indicated that magma of its large eruption was also generated from the partially molten crust. Although a part of the processes of magma

accumulation in the crust has been revealed geochemically, it has not been well examined from geophysical exploration of the subsurface structure. The locations and the volumes of magma chambers or partially molten regions in the crust have not been clarified yet.

For revealing the processes of volcanism in Kyushu, the issues mentioned above should be resolved. Those results will contribute to understanding material circulation caused by a subducting young oceanic plate and processes of caldera forming eruption.

First, we try to detect seismic velocity discontinuities, namely, such as the continental Moho, the upper and lower boundaries of the subducting oceanic crust, beneath Kyushu. This study is explained in chapter II. We also try to reveal the S-wave velocity structure of the crust beneath the Aso caldera, and this is explained in chapter III. In order to examine subsurface structure, we use receiver function technique [*Langston,* 1979]. This technique enhances shear waves in a coda of teleseismic P-wave converted at discontinuities beneath a seismic station. This technique has not been applied to estimate the subsurface structure beneath Kyushu with data from a dense seismic network. Structural exploration with this technique can detect seismic velocity discontinuities with a higher resolution than that with seismic tomography which has been applied in Kyushu in the previous studies. Tomographic studies in Kyushu have revealed that the slab mantle of the PHS plate has high velocity and the mantle wedge beneath the forearc region has low velocity [e.g. *Zhao et al.,* 2000; *Honda and Nakanishi,* 2003; *Wang and Zhao,* 2006; *Nakajima and Hasegawa,* 2007; *Xia et al.,* 2008; *Hirose et al.,* 2008; *Tahara et al.,* 2008].

The geometries of discontinuities in the uppermost mantle have been estimated in some other subduction zones [e.g. *Yuan et al.,* 2000; *Bostock et al.,* 2002; *Kawakatsu*

and Watada, 2007; *Audet et al.,* 2009]. *Bostock et al.* [2002] revealed that polarity of velocity contrast at the continental Moho is reversed, thus the mantle has lower velocity than the continental lower crust, beneath the forearc region of Cascadia subduction zone. The hydrated mantle is expected to have extremely low S-wave velocity and they interpreted that the mantle below the "inverted Moho" is highly serpentinized. The hydrated oceanic crust is expected to have lower S-wave velocity than the surrounding anhydrous mantle [e.g. *Hacker et al.,* 2003a]. Therefore, the oceanic crust which is detected as a low velocity layer is interpreted to be hydrated [e.g. *Kawakatsu and Watada,* 2007]. Water transportation through the subducting oceanic crust will be revealed from the detected geometry of discontinuities in the uppermost mantle.

The portion containing aqueous fluid or molten rocks also have lower S-wave velocity than the surrounding portion [e.g. *Watanabe,* 1994; *Takei,* 2002]. We expect to elucidate the processes of accumulation of magma in the crust beneath a caldera with receiver functions. A large eruption cycle has a long repose time (10^3-10^6 year) [*Takahashi,* 1995]. In order to understand the process of large eruptions, we should examine subsurface structures beneath several calderas which have different repose times or different time lengths from the latest large eruptions. At the first step of the exploration of the crustal structure beneath several calderas, we operate a dense seismic network to observe seismic events in the Aso caldera and estimate S-wave velocity structure from the waveform data with receiver function analyses.

II. Receiver function imaging of the uppermost mantle of the Kyushu subduction zone, Japan: Implications for water transportation through the Philippine Sea slab

1. Introduction

In order to understand the mechanism of water transportation through a young and steeply dipping slab, it is important to identify where the hydrated subducting oceanic crust and the hydrated mantle exist beneath Kyushu. Recently, stable temperature and pressure conditions of rock facies of the hydrated oceanic crust and mantle have been revealed in detail [e.g. *Hacker et al.*, 2003a]. It is known that hydrated mantle material is rheologically weak with a low density [*Hyndman and Peacock*, 2003]. Therefore, it is also useful to detect the hydrated portion for constraining the temperature structure and convection regime of the mantle in the subduction zone.

In some subduction zones in the world, the geometry of the upper and lower boundaries of the subducting oceanic crust is estimated by detecting and mapping seismic velocity discontinuities [e.g., *Yuan et al.*, 2000; *Bostock et al.*, 2002; *Kawakatsu and Watada*, 2007; *Audet et al.*, 2009]. Hydrous and anhydrous portions of the oceanic crust and the mantle wedge were obtained from examining the discontinuities in the uppermost mantle.

However, the geometry of the discontinuities in the uppermost mantle has not been well examined for Kyushu, Japan. In this study, we estimate the geometry with receiver function (RF) analyses and detect where fluid is contained in the oceanic crust and in

the mantle wedge.

2. Development of a method for stacking RFs

In many studies, refraction of seismic waves at dipping interfaces has not been taken into account when RFs are stacked. Seismic rays traced assuming horizontal interfaces would have different paths from those of true rays that pass through dipping interfaces. Refraction of seismic waves at dipping interfaces should be taken into account for accurate estimation of interface geometry.

In the following, we stack RFs, which are synthesized with a velocity model containing dipping interfaces, and show the error in the interfaces geometry estimated with a horizontally layered 1-d model of ak135 [*Kennett et al.,* 1995]. To reduce the error, we develop a new method for stacking RFs using the multistage fast-marching method (FMM) [*de Kool et al.,* 2006].

2.1 Synthesizing RFs for a velocity model with dipping interfaces (Slab Model)

2.1.1 Assumed velocity model

We assume a model, which has the width of 5° in both latitude and longitude (the center of the model is at latitude 32.5°) and the thickness of 315 km (0-315 km in depth). The model contains a slab subducting toward the west and we show a part of the model in Figure 2. We call this model the "Slab Model". The model contains 5 interfaces dividing the model region into 6 parts. The seismic velocities of the slab mantle are

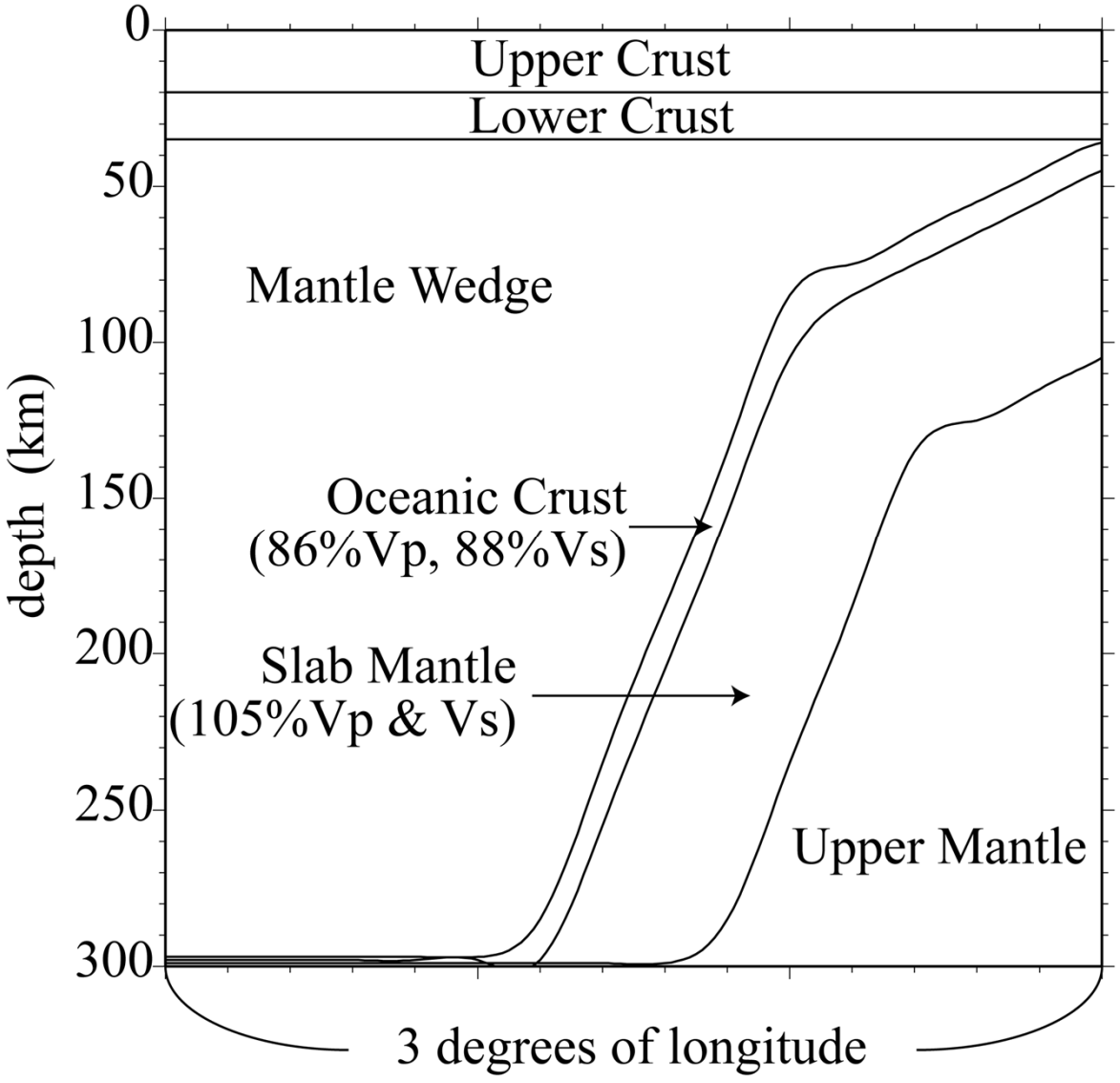

Figure 2 The assumed seismic velocity structure, in which a high velocity slab mantle with a low velocity oceanic crust is subducting (Slab Model). Assuming this structure, we synthesize RFs with the Gaussian Beam Method. This structure is modeled after the Philippine Sea slab subducting beneath Kyushu, southwest Japan.

105% of those of ak135. This velocity anomaly of the slab mantle is consistent with regional tomographic studies in Japan [e.g. *Nakajima et al.*, 2001; *Nakajima and Hasegawa*, 2007]. P and S wave velocities of the subducting oceanic crust are assumed as 86% and 88% of those of ak135, respectively, so that the assumed velocity contrast at the oceanic Moho is the same magnitude as the velocity contrast at the Moho in ak135. The other regions have the same velocities as the ak135 model. The slab is assumed to be bending, and the dip angle changes from 30˚ to 70˚ around a depth of 80 km (Figure 2). We assume the seismic velocity structure extends in the latitude direction. In this respect, our modeling is 2.5 dimensional.

We construct the synthetic waveforms arising from 9 synthetic teleseismic events whose back-azimuths from the modeled region are 105˚, 135˚, 165˚ and whose epicentral distances from the region are 40˚, 60˚, 80˚. Hypocenters of these events are assumed to be on the ground surface. Teleseismic rays impinge from the south-east onto the slab subducting toward the west. We explain about the assumed epicentral distribution in 2.1.2.

26 stations are assumed to be on an E-W line spaced evenly at a separation of 0.1˚ longitude. The locations of the synthetic seismic stations are aligned perpendicularly to the strike of the assumed subducting slab.

2.1.2 Synthetic teleseismic events and seismic stations

In order to select hypocenters and the components of RFs which are suitable for detecting the assumed interfaces, we examine how RF amplitudes are affected by dipping interfaces assuming a simple half space model with two layers. S-wave velocities of the upper and lower layers are assumed to be 4.0 km/s (Vp = 6.9 km/s) and

4.5 km/s (Vp = 8.1 km/s). 4.5 km/s and 8.1km/s are the same as the S-wave and P-wave velocities of the uppermost mantle in the ak135 model, respectively. The interface is assumed to exist at a depth of 70 km beneath a station and to dip at 10˚, 20˚ or 30˚ toward the west. We synthesize teleseismic waves whose ray parameters are 0.042 s/km (corresponding to the epicentral distance of 90˚) with generalized ray theory (GRT) [*Helmberger,* 1974], and calculate RFs from the synthetic waveforms with the extended-time multitaper method [*Shibutani et al.*, 2008]. In Figure 3, we show synthetic RFs, on which Ps phases converted at the assumed interface appear at 6-8 s. *Cassidy* [1992] also examined dipping layer effects on RFs. Amplitudes of Ps phases on our synthetic RFs (Figure 3) have the same dependence on back-azimuths as those of his study.

If the dip angle of the interface is 10˚ (Figure 3a), Ps phases on radial RFs have larger positive amplitude than those on transverse ones. The amplitude of radial RFs with down-dip back-azimuth (around 90˚) is very small when the interface dips at 20˚ (Figure 3c), and their polarity is reversed when the interface dips at 30˚ (Figure 3e). Since the polarity of a radial RF with a larger ray parameter would not be reversed until the interface dips more steeply, radial RFs are suitable for geometric estimation of interfaces dipping at less than 20°. However, we should not use radial RFs with down-dip back-azimuth for geometric estimation of interfaces dipping at larger than 20°, because some of them which have very small or reversed amplitude corresponding to the dipping interface would disturb the estimation.

In contrast, the polarity of transverse RFs does not change depending on the dip angle of the interface, although it changes depending on back-azimuth (Figure 3b, d, f). Therefore, radial RFs with up-dip back-azimuth or transverse RFs with the restricted

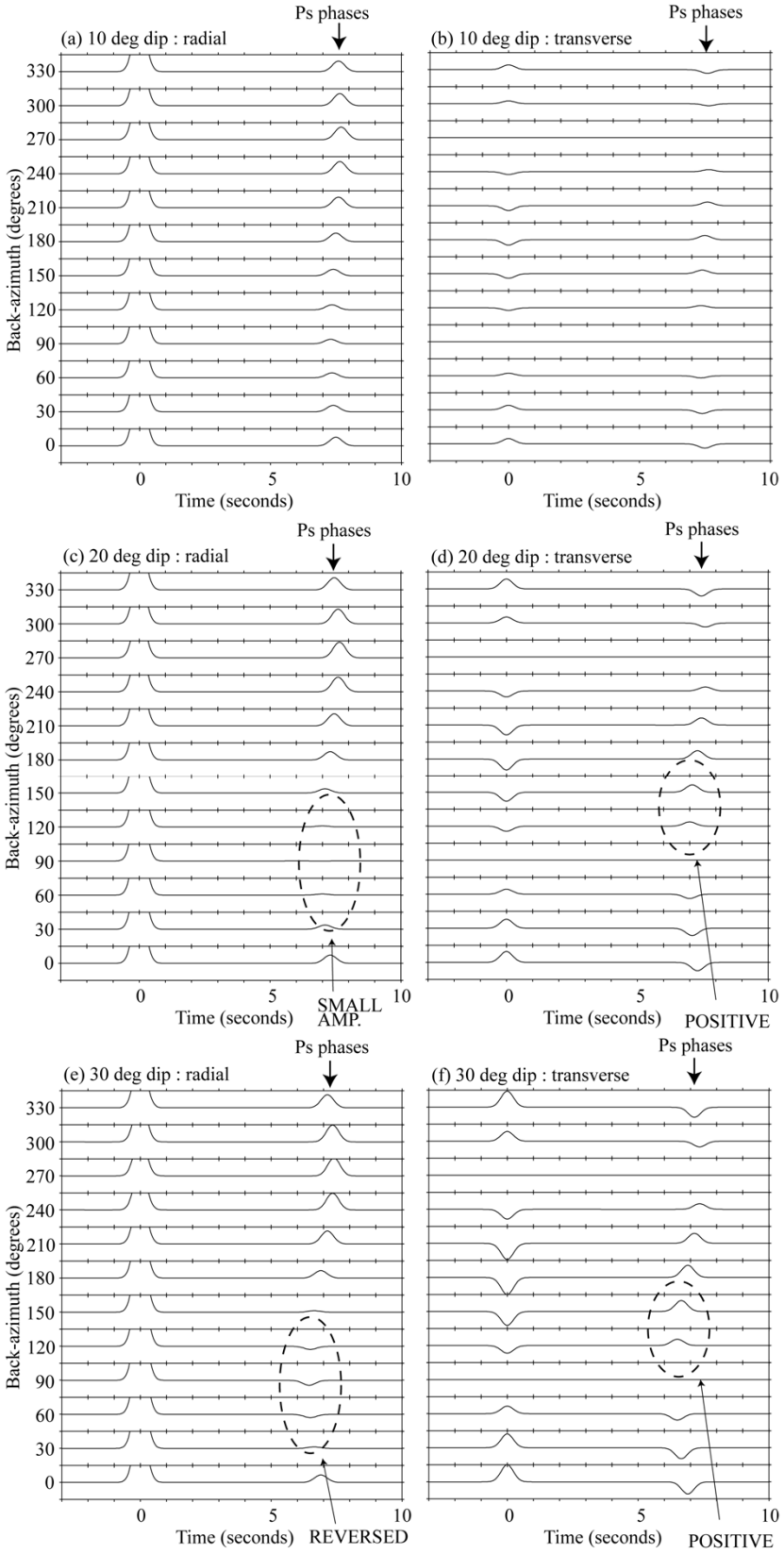

Figure 3 RFs synthesized with generalized ray theory assuming the two layered half space model. In each plate, RFs are shown in each 30˚ of back-azimuth. RF amplitudes from -0.1 to 0.1 are shown in order to make Ps converted phases more clear. (a,b) Radial and transverse RFs synthesized assuming the interface dips at 10˚. (c,d) Those at 20˚. (e,f) Those at 30˚.

back-azimuth should be used to detect interfaces dipping at larger than 20˚.

If an interface dips at larger than 50˚, some teleseismic waves with up-dip back-azimuth impinge nearly parallel to the interface. Consequently, it is difficult to detect the interface. The incident angle of a teleseismic P-wave with a ray parameter of 0.08 s/km (corresponding epicentral distance of 30˚) is always larger than 40˚ in the mantle if a horizontally layered structure (ak135) is assumed. Therefore, neither radial nor transverse RFs with up-dip back-azimuth should be used to detect interfaces dipping at larger than 50˚.

Because interfaces in the Slab Model are assumed to dip at 30˚-70˚ toward the west, only transverse RFs which come from the south-east or the north-east should be used for detecting them.

2.1.3 Calculating RFs for the Slab Model

We calculate RFs from teleseismic waveforms synthesized with the Slab Model and the synthetic event/station distributions. A code constructed by *Sekiguchi* [1992] and modified by *Hirahara et al.* [2007] is used for synthesizing waveforms with the Gaussian Beam Method [*Červený,* 1985]. To calculate RFs, we use the extended-time multitaper method.

2.2 Stacking RFs with a 1-d velocity model (ak135)

We migrate these synthetic transverse RFs to the depth domain with the ak135 velocity model, and project them on a section which consists of 0.02° in longitude by 2

km in depth cells and is parallel to latitude lines (Figure 4). When two or more RFs are projected on the same cell, the amplitudes are averaged. Ps phases converted at discontinuity interfaces dipping toward the west with upward decreasing velocity, produce positive peaks on transverse RFs with back-azimuths of 105˚-165˚ (Figures 3d, f), while those converted at discontinuity interfaces with upward increasing velocity produce negative peaks.

In Figure 4, peaks of RFs indicate 3 dipping interfaces. The top and the bottom of the slab are indicated by negative peaks (blue), and the oceanic Moho is indicated by positive peaks (red). The interface geometry estimated from the RF peaks is different from the assumed geometry indicated by solid lines in Figure 4. The cause of the difference is that the RFs are stacked with ak135 in spite of the fact that those RFs are synthesized with the Slab Model shown in Figure 2. Therefore, we now investigate how to take into account refraction of seismic rays at dipping interfaces to improve the geometric estimation.

2.3 Stacking receiver functions with the multistage FMM

We stack RFs taking account of refraction using 3-dimensional travel time fields calculated with the multistage FMM. We use a grid model which has widths of 3˚ in both latitude and longitude and a thickness of 301 km (from 1 km above sea level to 300 km below sea level), with a grid spacing of 0.02˚ in the horizontal directions and of 2 km in depth in order to calculate travel time fields.

First, we use the Slab Model as a velocity structure. Travel time fields of P-wave propagated upward from the synthetic teleseismic events and those of S-wave

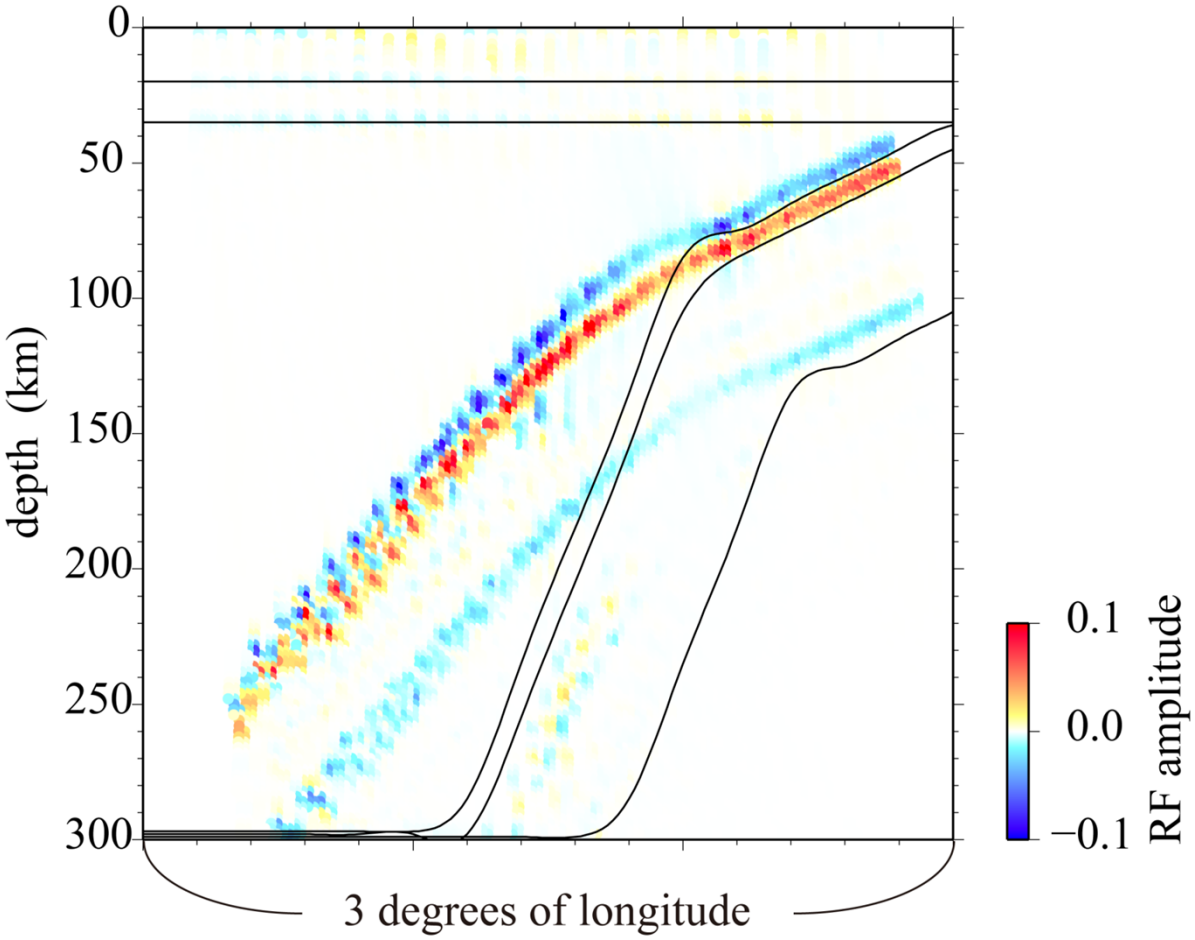

Figure 4 A vertical section which is constructed by stacking transverse RFs with a 1-dimensional velocity model (ak135). These transverse RFs are synthesized with the Gaussian Beam Method by assuming the Slab Model shown in Fig.1. The color bar shows the scale of RF amplitude. Positive (negative) peaks of these transverse RFs are produced by interfaces dipping toward the west with upward decreasing (increasing) velocities. Solid lines indicate the assumed interfaces of the Slab Model shown in Figure 2.

propagated downward from the synthetic stations are calculated with the multistage FMM (Figures 5a, b). With these travel time fields, for each pair of a teleseismic event and a station, the lag time of arrivals between the teleseismic P-wave and a Ps-wave converted at a node and scattered to the station are obtained by subtracting the P-wave arrival time at the station from the sum of the P-wave and S-wave travel times to the node. An example of a lag time field is also shown in Figure 5c. To follow Snell's law, we select nodes in which the P-wave slowness vector component that is parallel to the nearest interface is opposite in direction and equal in magnitude to the corresponding component of S-wave slowness vector (Figures 5d, e). With the selected nodes and their lag times, the amplitudes of each transverse RF are plotted in the model region. When two or more RFs are plotted in the same node, the amplitudes are averaged. A section of the stacked RFs is shown in Figure 6a. The assumed interfaces are correctly estimated.

In Figure 6b, we show a RF section which is constructed by assuming the ak135 velocity model and interface geometry of the Slab Model (shown in Figure 2). In this case, although the velocity values are the same as those of ak135, which is different from the Slab Model, the P-to-S conversion occurs at interfaces which are not horizontal but dipping at the same angle as the nearest interface in the Slab Model. The estimation of interface geometry is also successful and a small error contained in the RF section in Figure 6b is not a practical issue. *Nakajima et al.* [2001] and *Nakajima and Hasegawa* [2007] indicated that a low velocity anomaly of about 5% exists in the mantle wedge, in Japan. We migrate RFs synthesized with another velocity model which has 5% lower Vp and Vs in the mantle wedge than the Slab Model and the same velocities as the Slab Model in the other layers, and obtain a RF image (Figure 6c). The error of interface geometry estimated from this image is also negligibly small. These

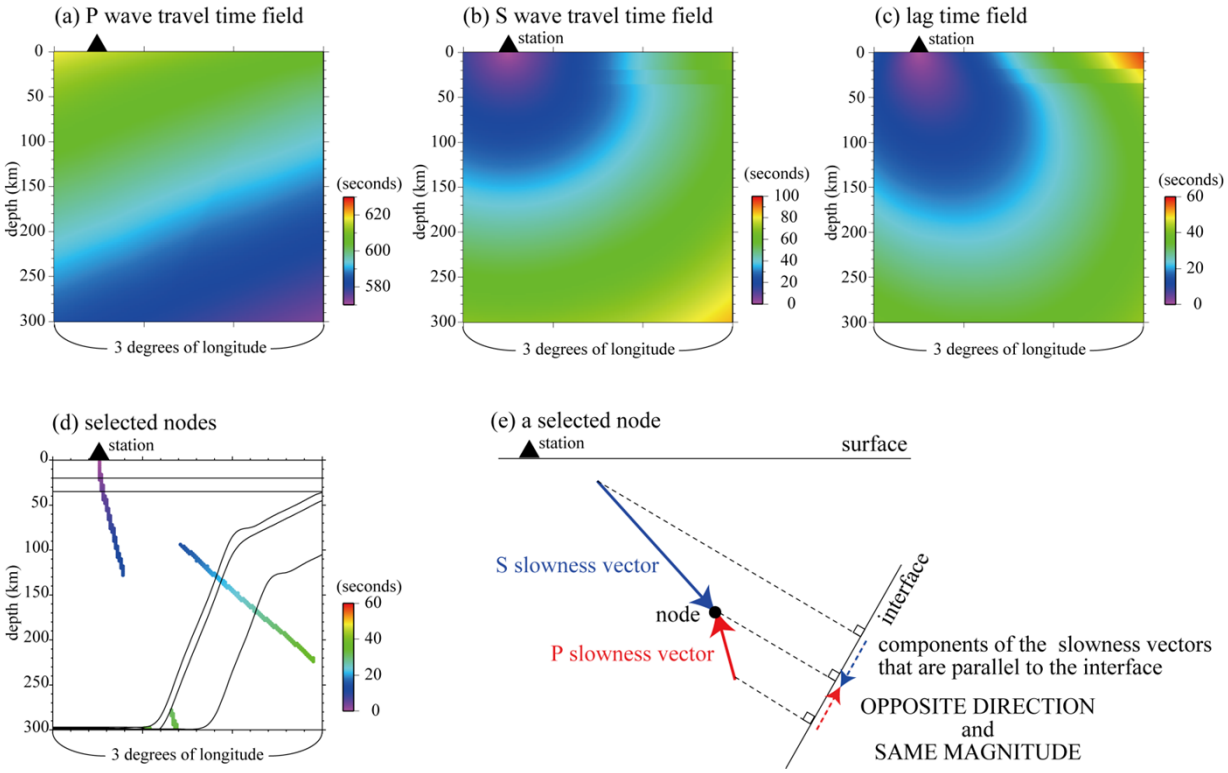

Figure 5 (a): Travel time field of a teleseismic P-wave generated by a synthetic hypocenter whose back-azimuth and distance from the modeled region are 135° and 60°, respectively. (b): Travel time field of an S-wave propagated from the station indicated by a triangle. (c): Lag time field of arrivals at the station between teleseismic P-wave and S-wave converted at each node. (a), (b) and (c) are vertical sections beneath the E-W array of the synthetic seismic stations. (d): Nodes selected as conversion points projected on a vertical plane parallel to latitude lines. (e): A schematic explanation for a selected node. A black circle indicates a node which is selected as a conversion point. Red and blue solid arrows indicate the P- and S-wave slowness vectors at the node, respectively. Red and blue dashed arrows indicate components parallel to the interface of the P- and S-wave slowness vectors, respectively.

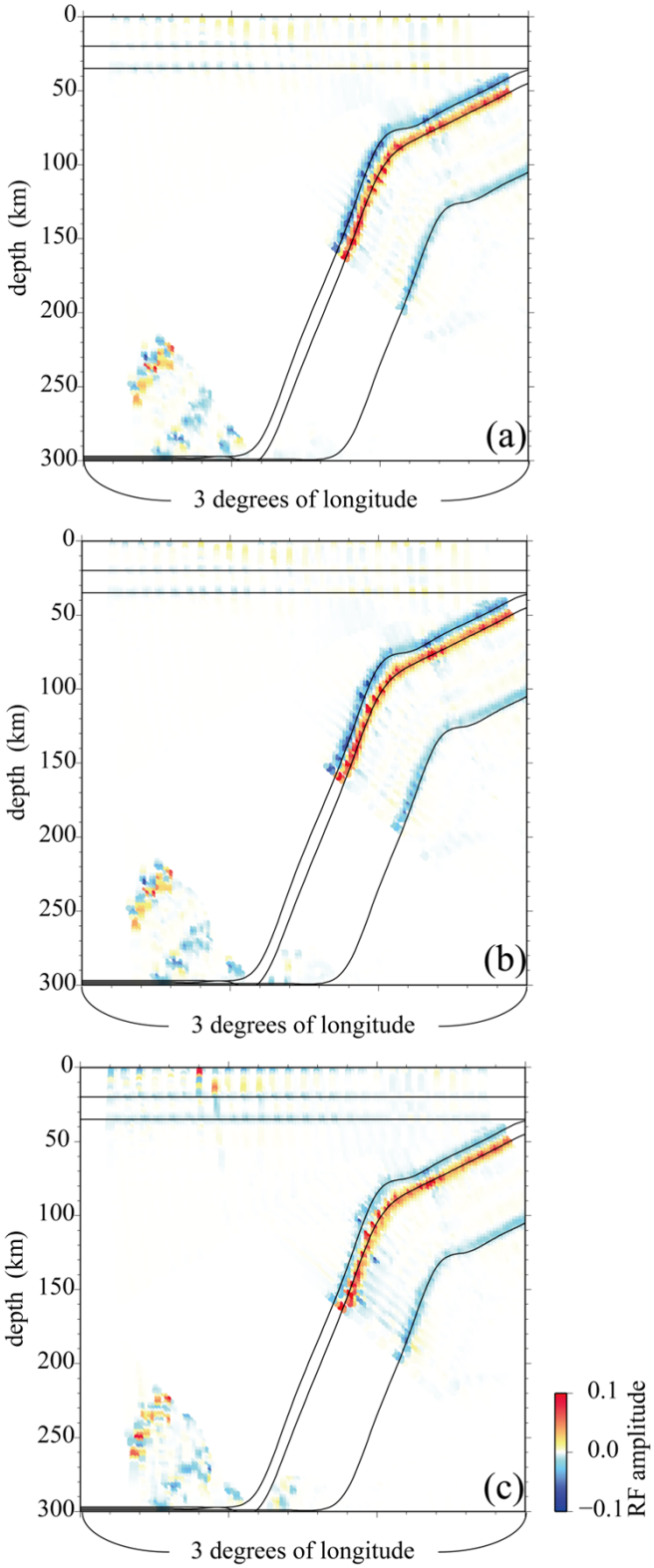

Figure 6 (a): RF section stacked with the multistage FMM by assuming the Slab Model. (b): RF section stacked with the multistage FMM by assuming ak135 and dipping interfaces of the Slab Model. (c): RF section with RFs synthesized with a velocity model whose mantle wedge has 5% lower seismic velocities than the Slab Model's, stacked with the multistage FMM by assuming ak135 and dipping interfaces of the Slab Model.

findings imply that estimation of dip angles of interfaces are critical for estimating their geometries, and RF images are not strongly affected by velocity anomaly expected to exist in subduction zones. In the following, therefore, we stack RFs with models which have arbitrary interfaces and the same velocities as ak135 at the nodes.

2.4 Estimation of interface geometry

When we take our approach to the estimation of subduction zone structure from observed data, we do not know the accurate interface geometry at the outset. Therefore, we develop a method to estimate the geometry iteratively by assuming approximate dip directions to restrict the back-azimuthal range of teleseismic events.

At the first iteration, we stack RFs by assuming only the ak135 model with no dipping interfaces and make the first estimation of the geometry. In each of the following iterations, we use the previously estimated geometry of dipping P-to-S conversion interfaces to calculate a new stack.

We apply this method to the RFs synthesized with the Slab Model and synthetic event/station distribution. In Figure 7, we show synthetic RF sections produced in each iteration. Figure 7a shows a RF section with RFs stacked assuming just the Conrad and the continental Moho. Figures 7b and 7c show RF sections with RFs stacked assuming the dipping interfaces estimated from Figures 7a and 7b (solid black lines in each section), respectively. RF peaks in Figures 7c correspond to the purple lines which indicate the interfaces of the Slab Model and the interface geometry is successfully estimated.

Kirchhoff migration of RFs [e.g. *Sheehan et al.*, 2000; *Boyd et al.*, 2007] can also

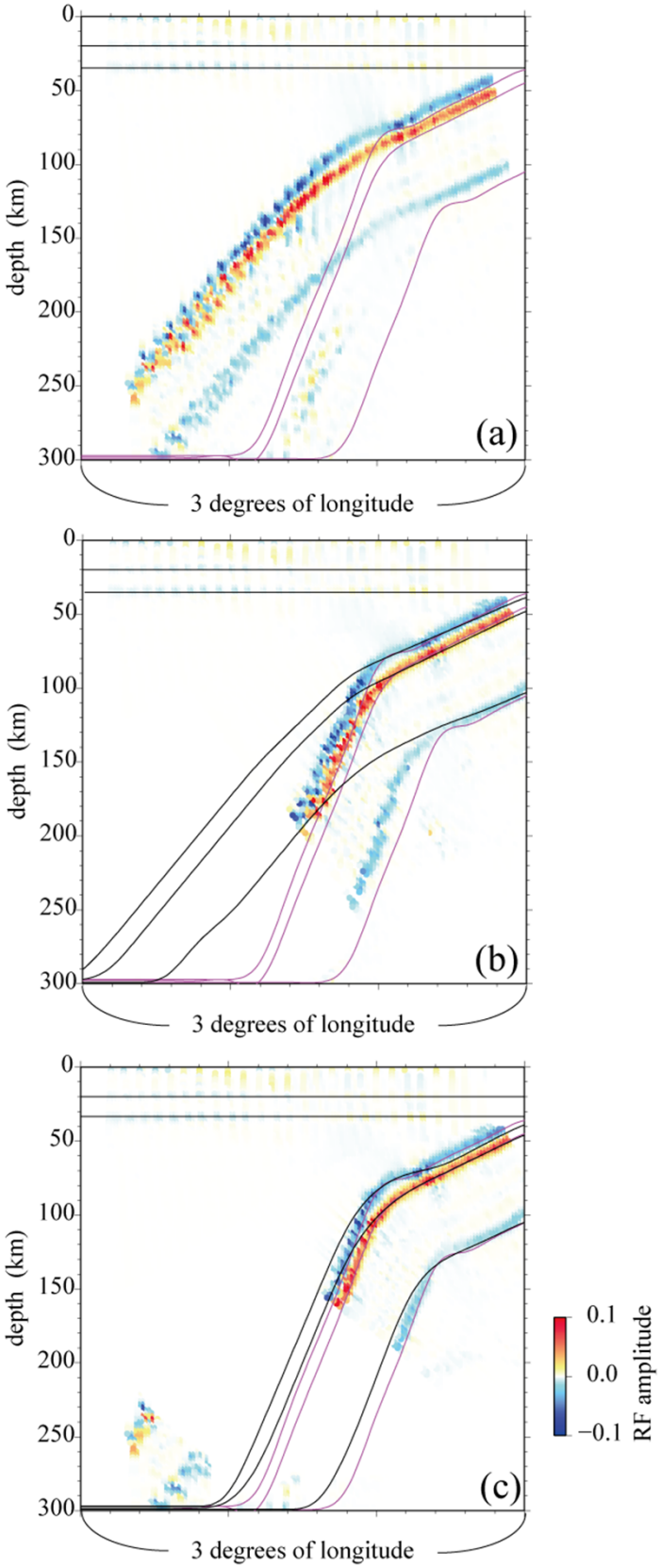

Figure 7 (a): RF section stacked with ak135. (b) and (c): RF sections stacked with ak135 and interfaces estimated from the section (a) and (b), respectively. Black lines indicate the interfaces assumed in order to stack RFs. Purple lines indicate interfaces of the Slab Model.

estimate geometries of dipping interfaces. In the method, S waves are assumed to be scattered to a station at all nodes, and RF amplitudes are assigned to the nodes based on the arrival time difference between the teleseismic P wave and the scattered S wave. In contrast, in our method we select nodes where teleseismic P waves are converted to S waves with satisfying Snell's law at dipping interfaces, and assign RF amplitudes on the selected nodes. Therefore, we can more adequately stack RF peaks which are derived from Ps converted phases.

Although the oceanic Moho is detected down to 250 km in depth in Figure 7(a), the oceanic Moho is detected down to 150 km in depth in Figure 7(c). We need seismic stations in the backarc region far from the trench to estimate the geometry of deep portion of the steeply dipping oceanic Moho.

3. Data and Estimation of Receiver Functions

We use 30,325 waveforms from teleseismic events whose epicentral distances are 30-90º, and magnitudes are greater than 5.5. Epicenters of these teleseismic events are shown in Figure 8. The waveform data were obtained from 78 stations of Hi-net established by the National Research Institute for Earth Science and Disaster Prevention (NIED) [*Obara et al.,* 2005], from 61 stations of the J-array established by the Japan Meteorological Agency (JMA), Kyushu University, Kagoshima University and Kyoto University [*Morita,* 1996], and from 13 stations of Sakurajima Volcano Research Center, Kyoto University (SVRC) (Figure 9). We use waveform data from Hi-net, J-array and SVRC, recorded from June 2001 to May 2010, from August 1996 to October 2009, and

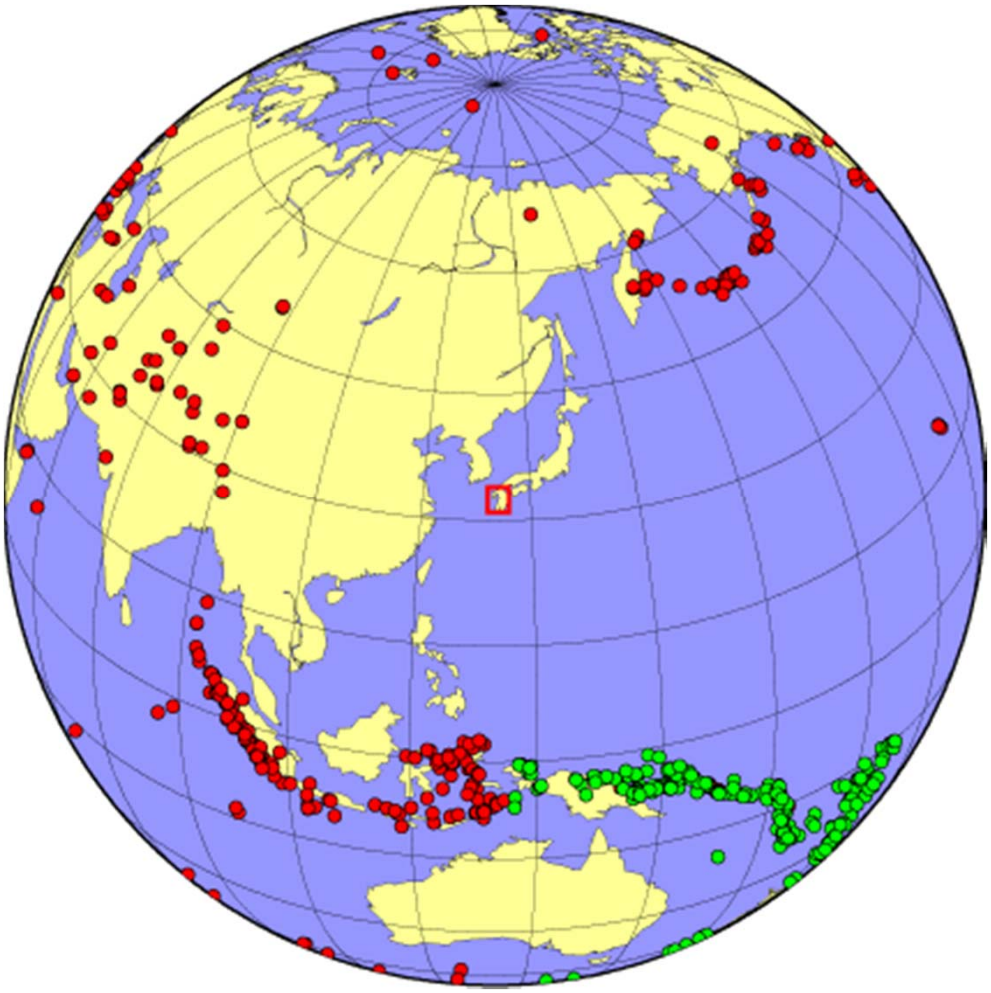

Figure 8 Epicenters of teleseismic events. Green circles indicate epicenters of teleseismic events used for both transverse and vectorial RF imaging. Red circles indicate epicenters of teleseismic events used for only vectorial RF imaging. Red rectangle indicates the area shown in the map in Figure 9.

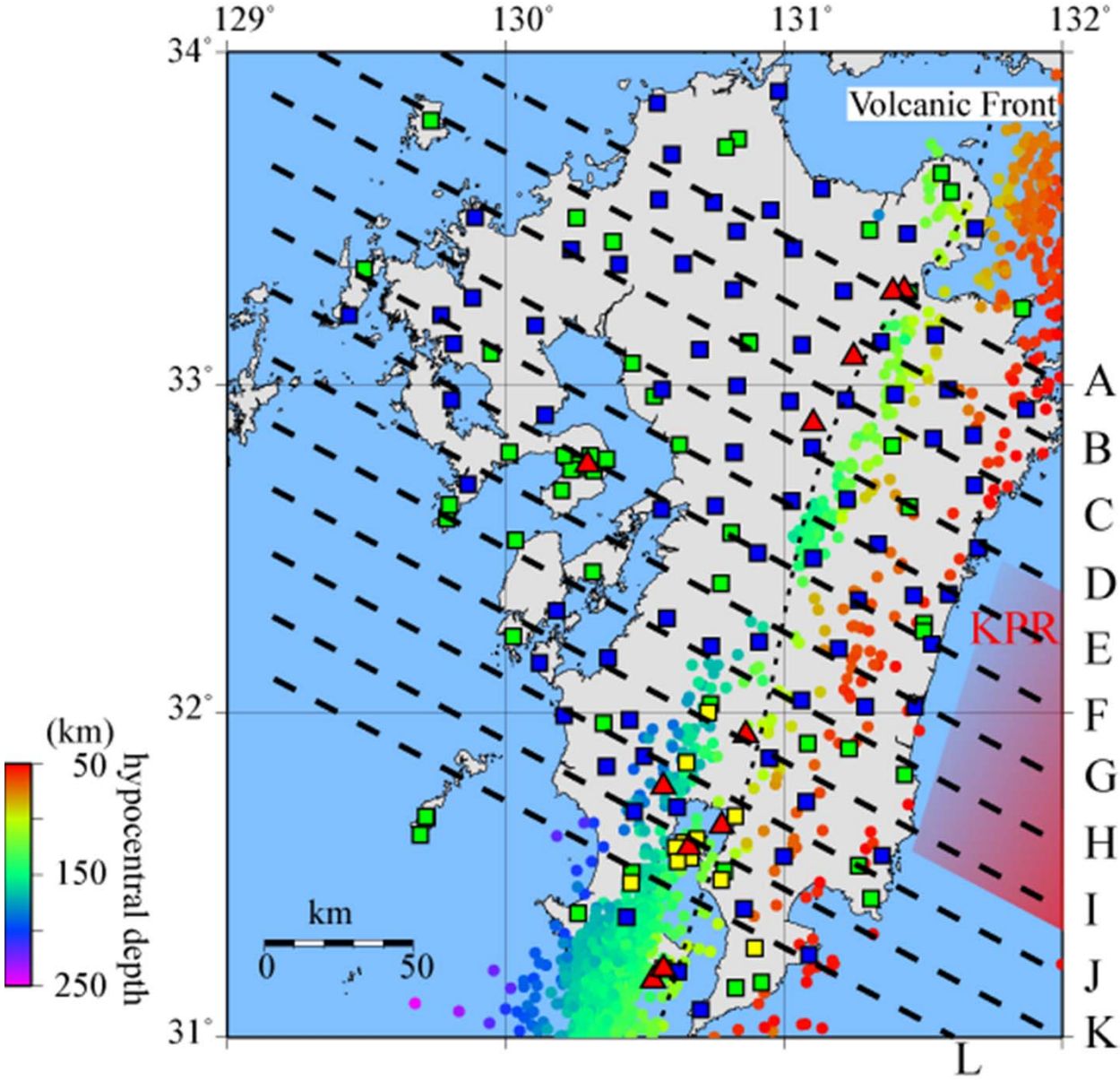

Figure 9　Map of Kyushu. Blue, green and yellow squares indicate stations of Hi-net, the J-array and Sakurajima Volcano Research Center (SVRC). The red triangles, the dotted line, the red shaded region and colored small circles indicate the same as those in Figure 1.

from January 2005 to December 2009 respectively.

A RF is calculated by deconvolving the vertical component of a waveform of a teleseismic P-wave from its horizontal components [*Langston,* 1979]. We calculate RFs with the extended-time multitaper method [*Helffrich,* 1996] which was improved by *Shibutani et al.,* [2008], with a 0.28 Hz low-pass Gaussian filter.

In order to estimate the geometry of steeply dipping discontinuities with RFs, refraction of the seismic rays at the dipping discontinuities should be taken into account. For this purpose, we apply the method explained in the previous section for stacking RFs.

4. Procedure for estimating the geometry of discontinuities

As mentioned in section 2.4, we first stack RFs with a 1-d velocity model (ak135). We determine from the distribution of intermediate-depth earthquakes that the dip azimuth of PHS slab is 298° (N62°W), and stack transverse RFs whose backazimuths are 118-178°, in the region at latitudes 31-34° north, longitudes 129-132° east and depths from 1 km above sea level to 300 km below sea level. Teleseismic rays for these RFs are expected to impinge on the PHS slab which slopes to the left. Therefore, Ps phases converted at discontinuities which dip parallel to the PHS slab and have upward decreasing (increasing) velocities should make positive (negative) peaks on these transverse RFs.

In Figure 10, the transverse RF sections constructed with a 1-d model are shown. In the sections, dipping discontinuities which slopes to WNW are detected. However, the

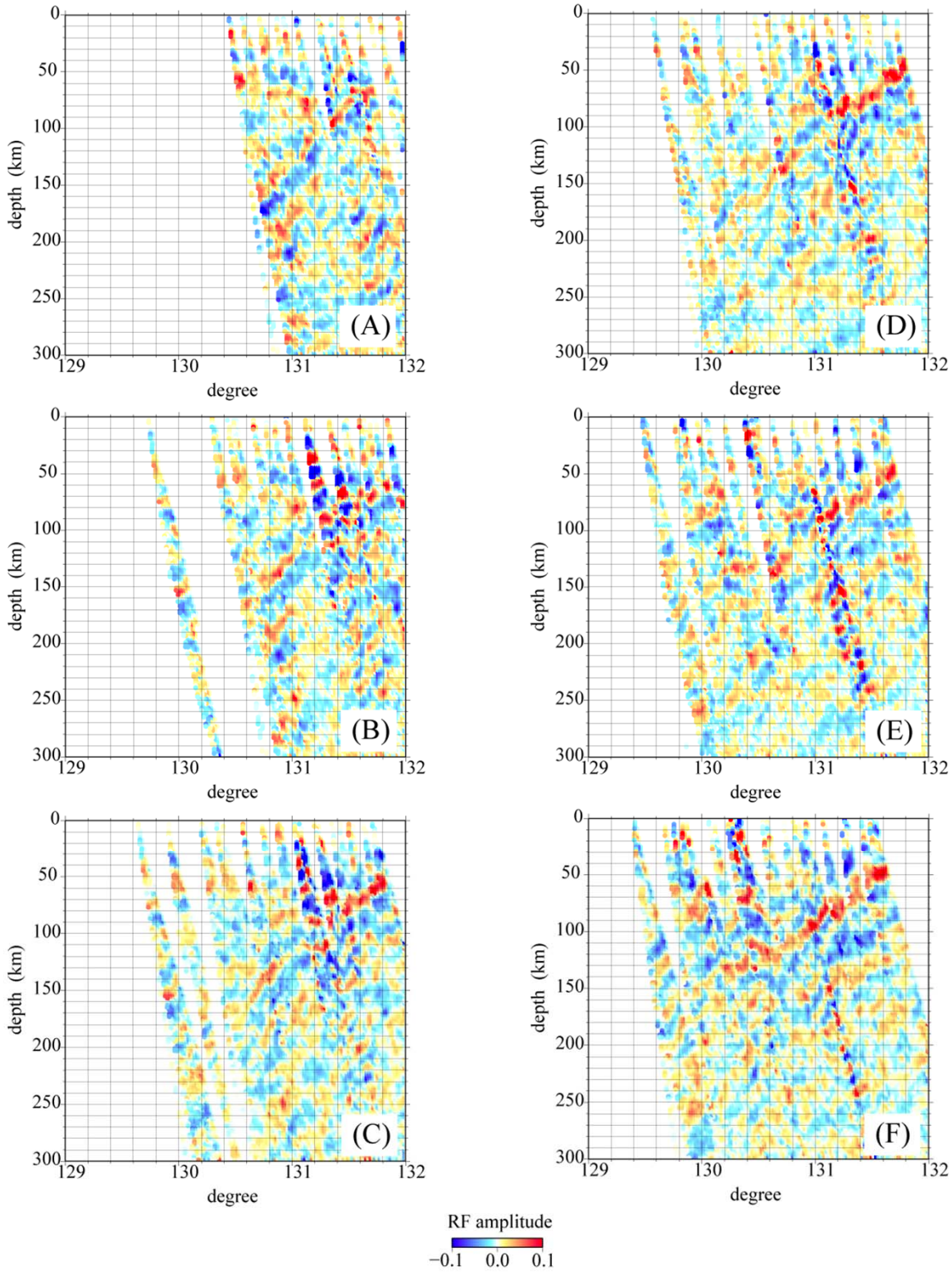

Figure 10　Transverse RF section along dashed lines in Figure 8 constructed with a 1-d model.

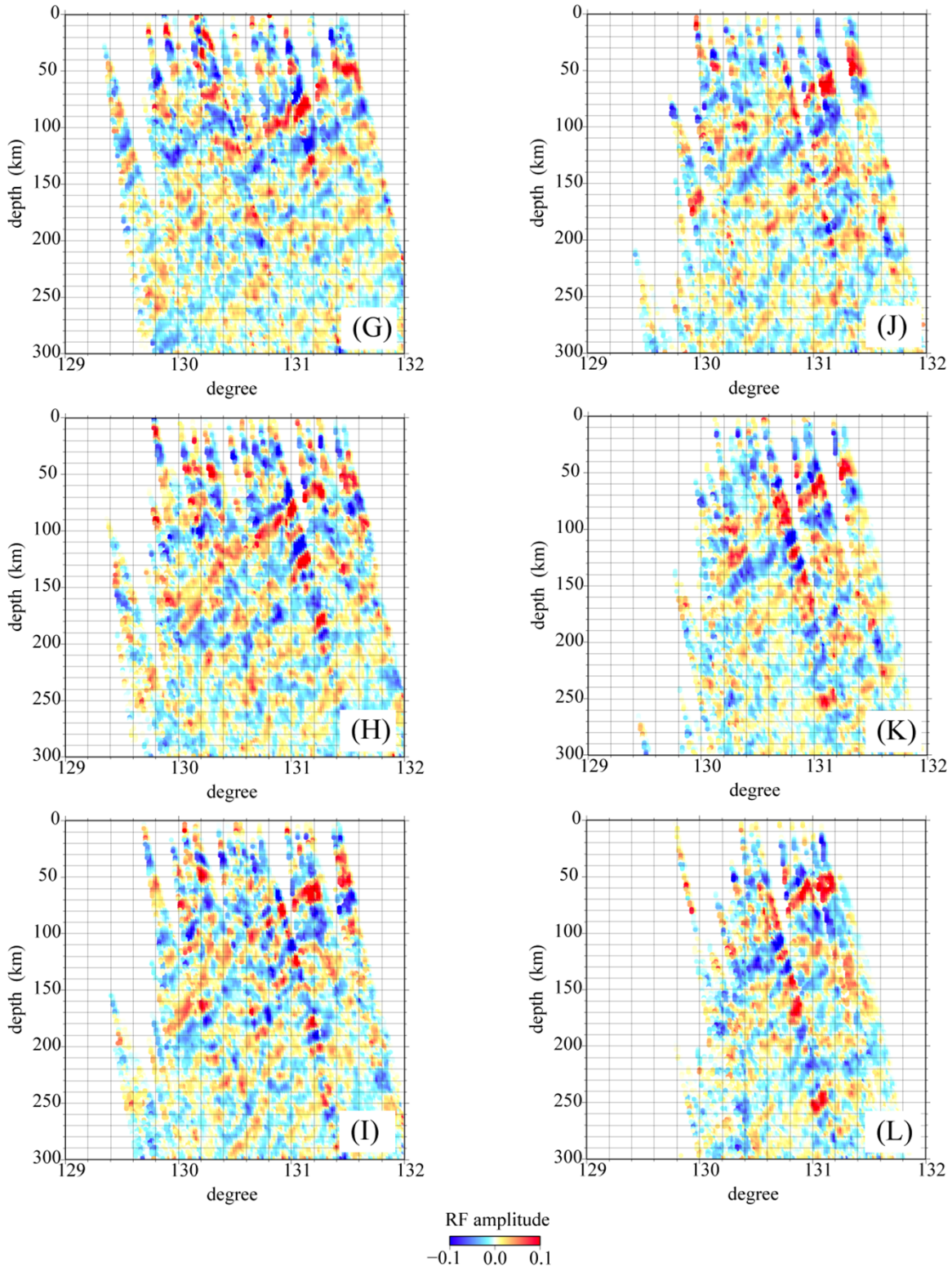

Figure 10 (Continued)

discontinuities are not subparallel to Wadati-Benioff zone (Figure 11), and it is expected that the detected geometry of the discontinuities are different from the real geometry because we assume teleseismic waves always refract at horizontal surfaces.

Then, we iteratively stack them with a model containing one additional dipping interface (the oceanic Moho) whose geometry is estimated in the former iteration. The discontinuity interpreted as the oceanic Moho is detected most clearly beneath the whole Kyushu region. Although we do not take the geometry of the upper boundary of the PHS slab, we mention the boundary later assuming that the upper boundary of the PHS slab is parallel to the oceanic Moho. We repeat this process until we obtain RF sections whose peaks coincide with the geometry of the assumed interfaces. After four iterations, such sections have been obtained (Figures 12 and 13), and we conclude that the interface geometry is correctly estimated.

Finally, we rotate radial and transverse component RFs into another horizontal component which is parallel to the horizontal component of the vibration direction of P-to-S converted wave estimated from the assumed dip angle and dip azimuth of the interface. Because the horizontal component of RF is rotated to horizontal component of vibration direction, we stack all RFs independent on their backazimuths to estimate the geometry of interfaces. This method which is called vectorial RF imaging introduced by *Kawakatsu and Yoshioka* [2011], enhances the RF peaks corresponding to both the dipping and horizontal discontinuities. We apply this method to the RFs whose backazimuths are 0-360º.

Backaziumths of the teleseismic events are not evenly distributed (Figure 8), and amplitudes of RF sections largely depends on the RFs from the direction where many teleseismic sources exist. However, amplitudes of RF section generated with evenly

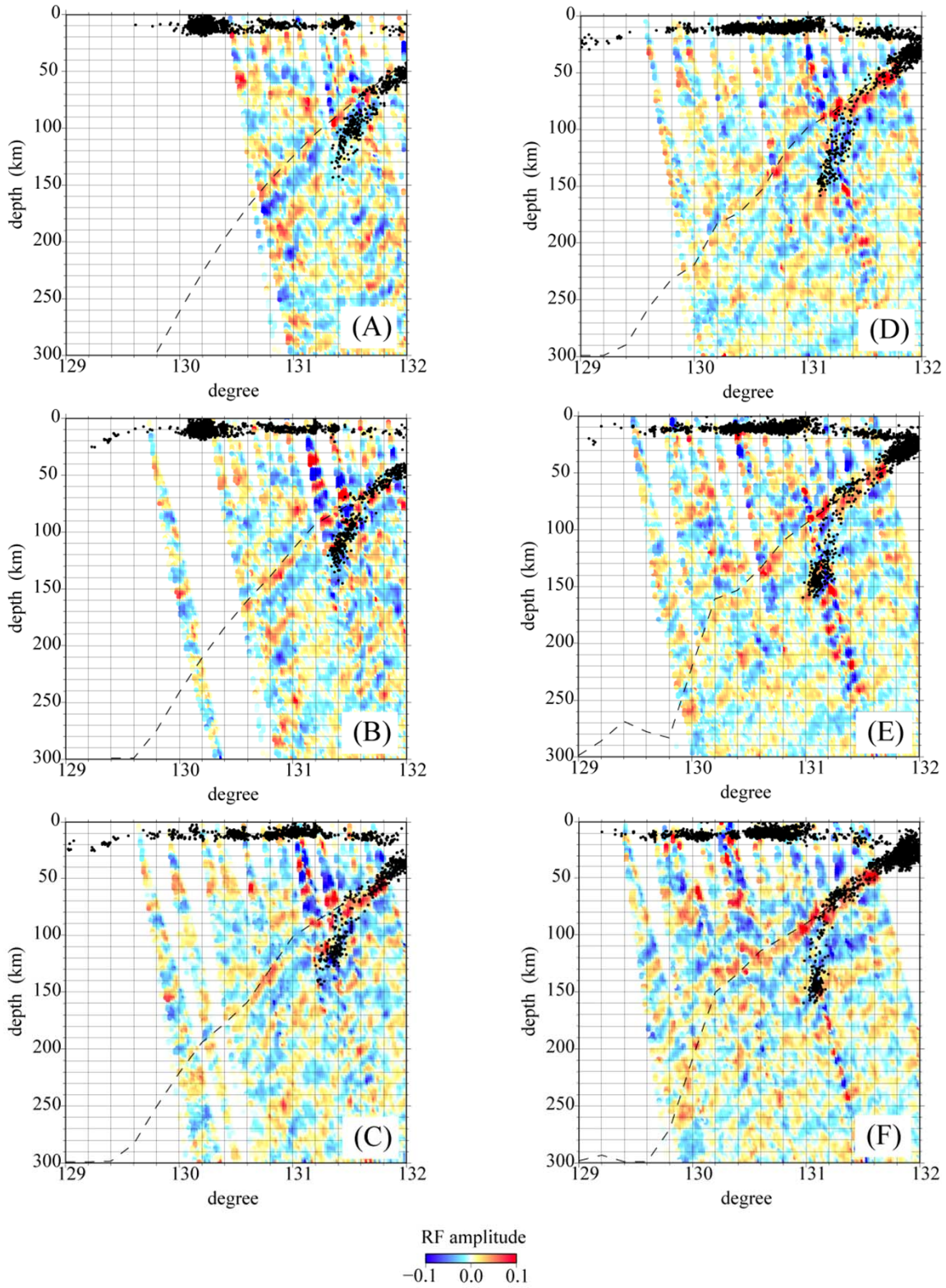

Figure 11 Transverse RF section along dashed lines in Figure 8 constructed with a 1-d model. Dots indicate hypocenter locations which exist in the region where RF amplitudes are averaged. The hypocenter locations are determined by JMA, and magnitudes and origin times of the earthquakes are greater than 1 and from Oct. 1997 tp Mar. 2007. The dashed lines indicate the estimated geometry of discontinuities from these sections.

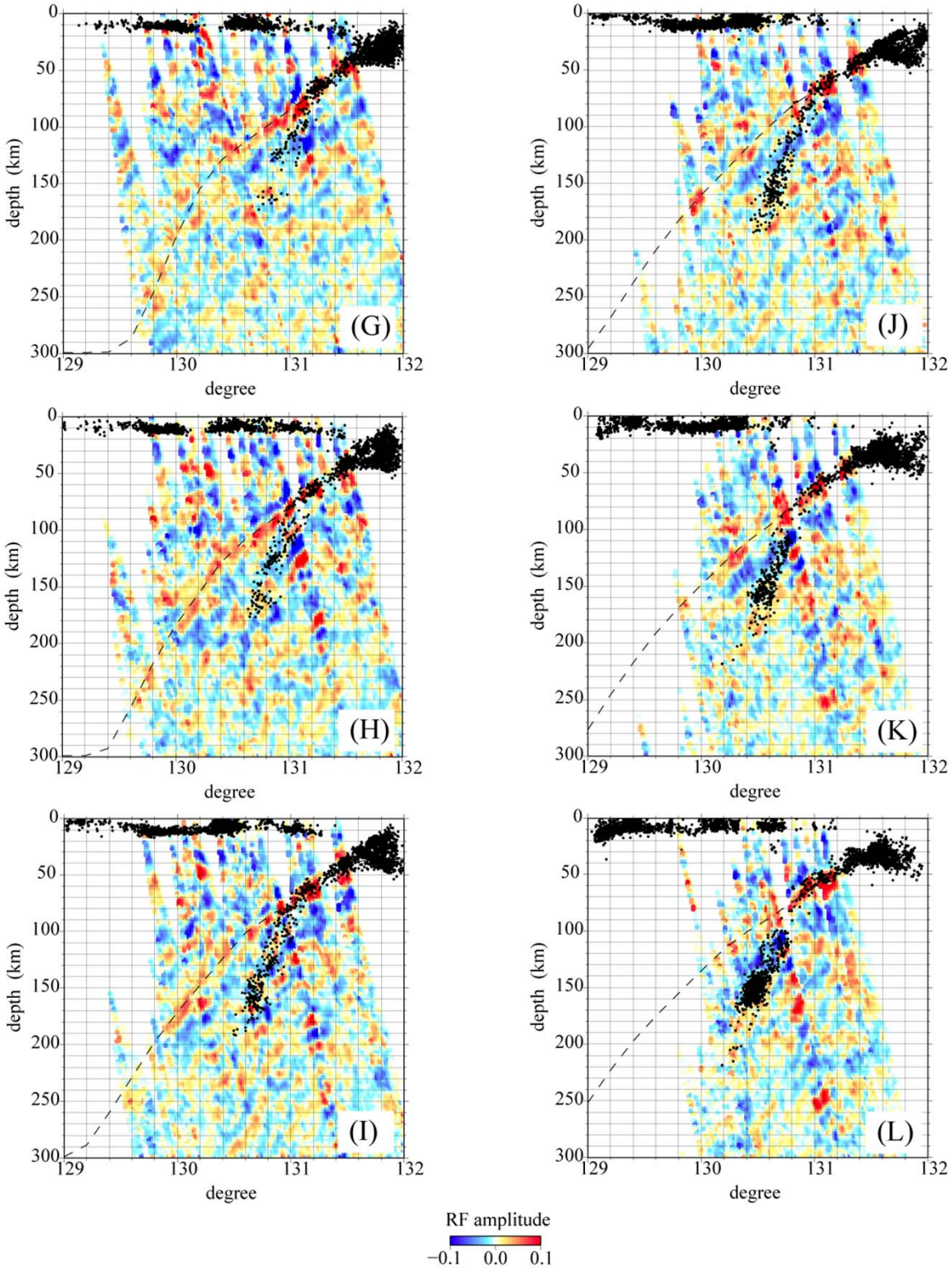

Figure 11 (Continued)

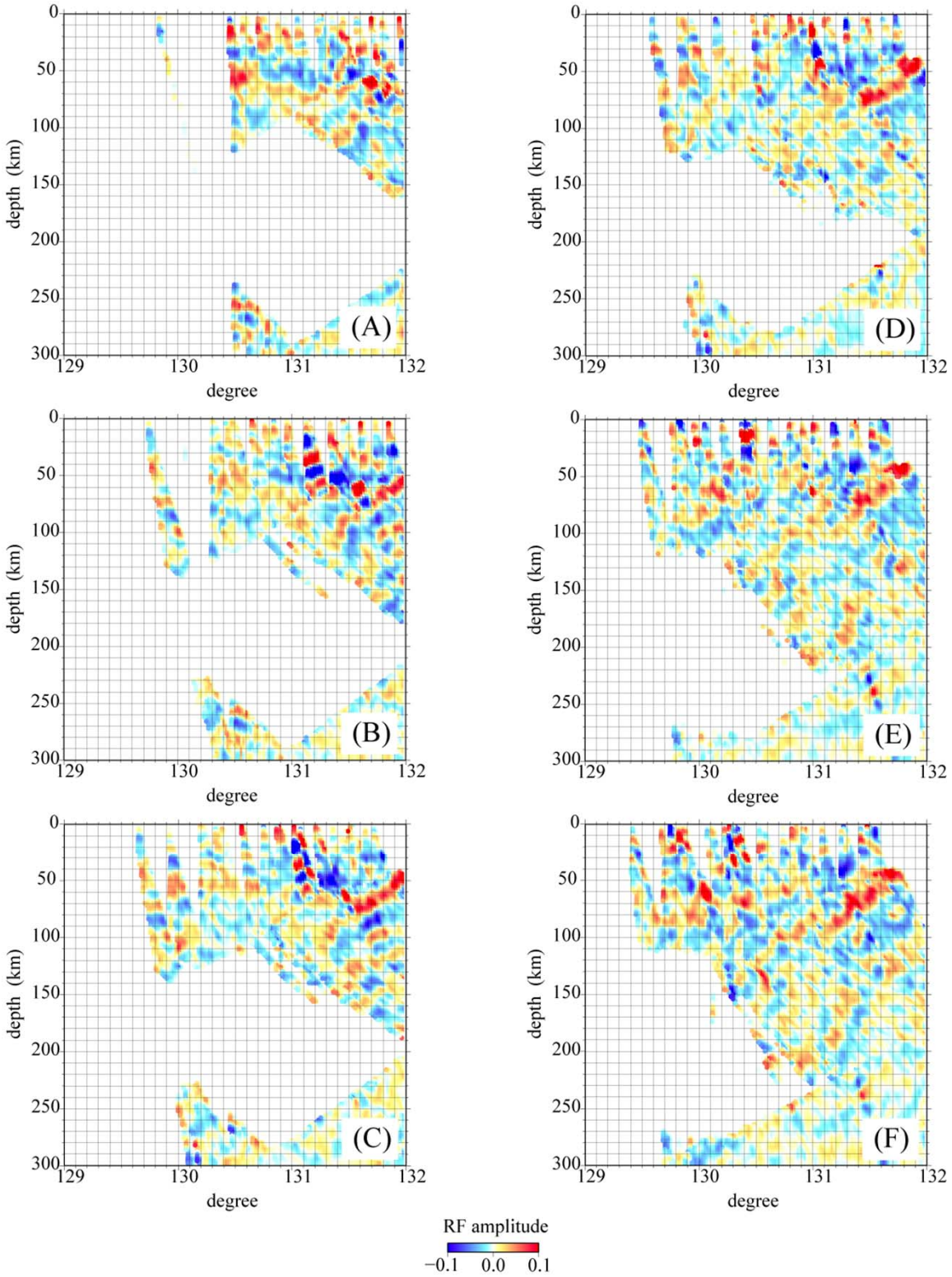

Figure 12 Transverse RF sections along dashed lines in Figure 8 obtained after the fourth iteration.

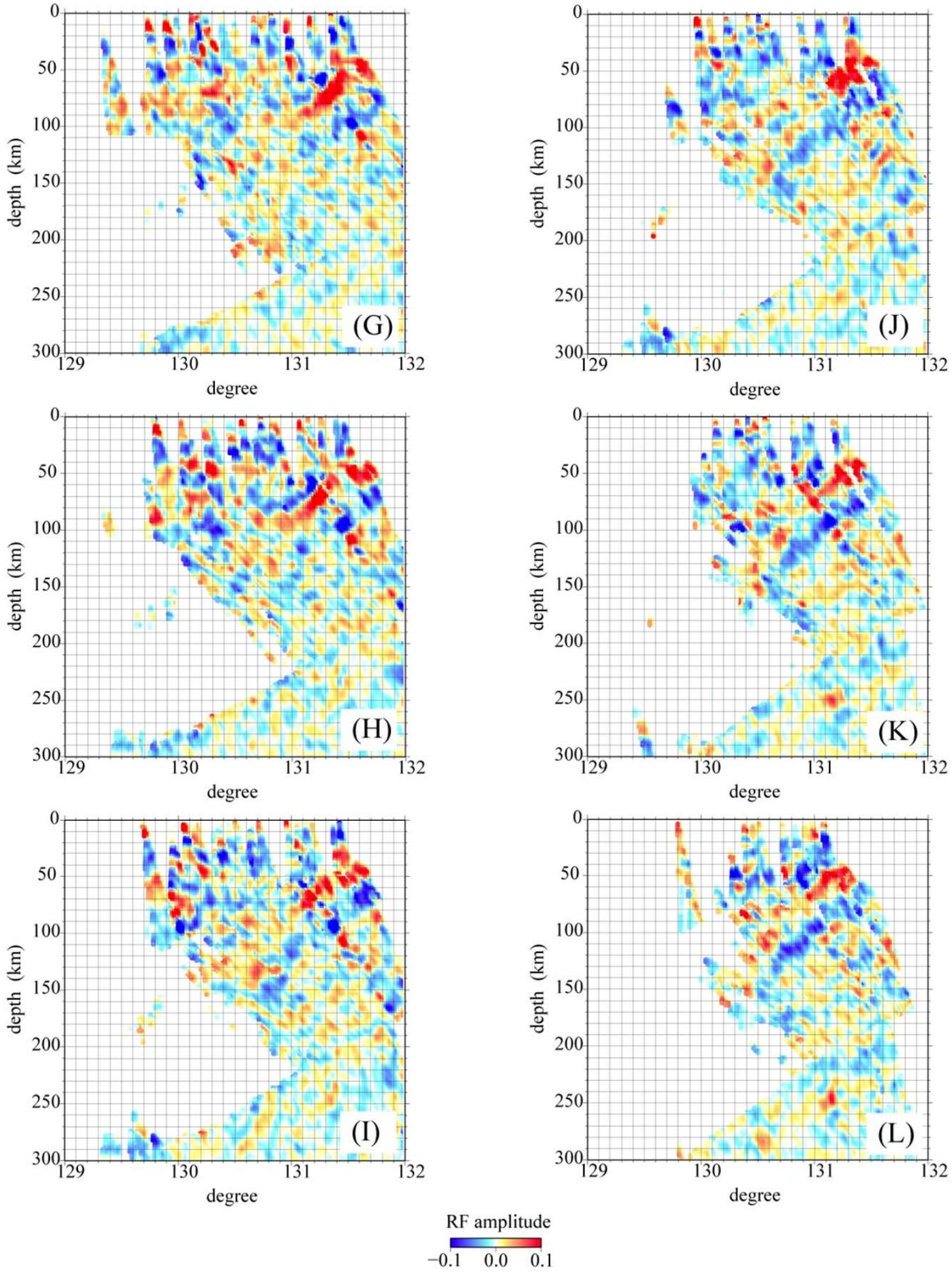

Figure 12 (Continued)

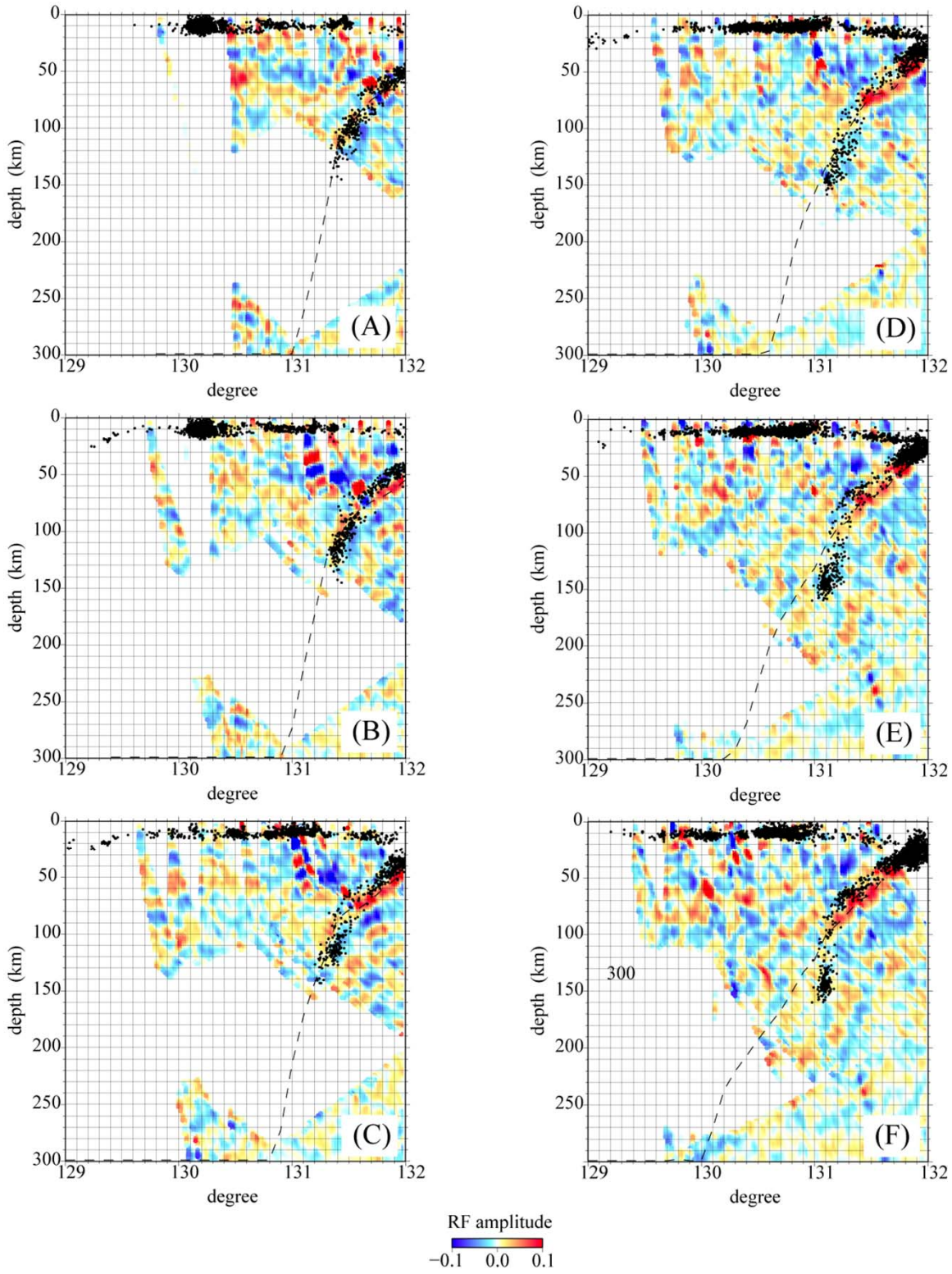

Figure 13 Transverse RF sections along dashed lines in Figure 8 obtained after the fourth iteration. Dots indicate the same as in Figure 9. The dashed lines indicate the assumed geometry of discontinuities.

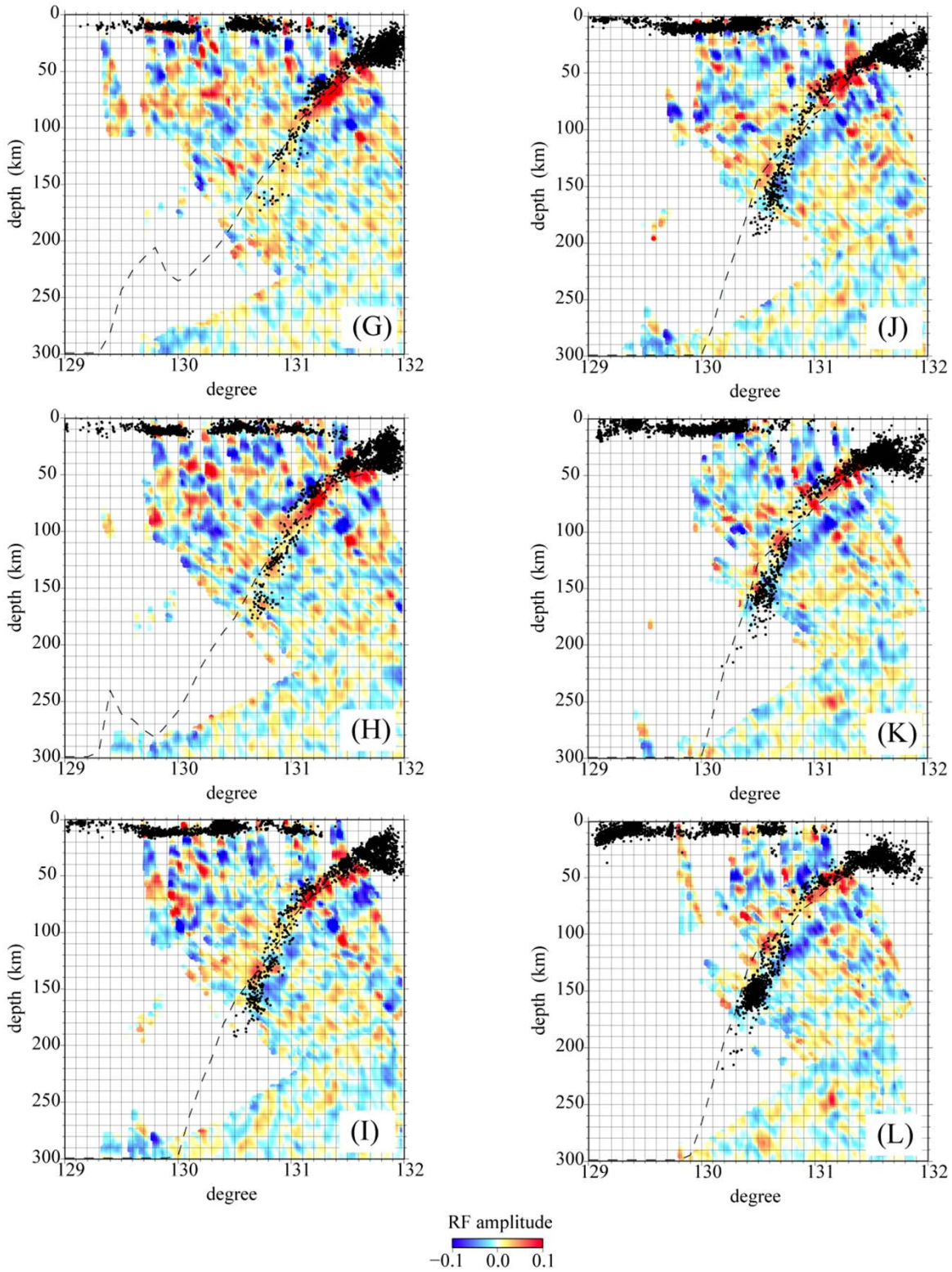

Figure 13 (Continued)

distributed teleseismic events more accurately indicates S-wave velocity contrasts at discontinuities if the medium has seismic anisotropy. Therefore, we stack RFs every 30º of backazimuth, and averaged the 12 sets of stacked RFs. The constructed RF sections are shown in Figures 14, 15 and 16.

5. Results

RF peaks beneath the area 40 km in width around each line shown in Figure 9 are projected on a section along the line. The RF section consists of 2 km by 2 km cells and each cell shows the amplitude of RFs that is projected on the cell. When two or more RFs are projected on the same cell, the amplitudes are averaged. Discontinuities that have upward (downward) decreasing seismic velocities are detected by positive (negative) peaks of RFs, and shown by warm (cool) colors. In Figures 11, 13 and 15, dots indicating hypocenters in the same region as RFs are projected are superimposed on each RF section.

In Figure 15, the positive peaks corresponding to the oceanic Moho is dipping at 30-50º. We have checked amplitudes of RF peaks made by shear waves which are converted at a discontinuity dipping at 30-50º with 10% of S-wave velocity contrast. We assume a model with a dipping low velocity layer shown in Table 1, and calculate RFs from the teleseismic waveforms synthesized with the assumed model. Dip angles of the low velocity layers are 30º, 40º, and 50º. Epicentral distances of the assumed sources are 40º, 60º, and 80º. Backazimuths of the assumed sources are 15º, 45º, 75° --- 315°, and 345°. We choose 26 models in which synthesized teleseismic rays impinge to the

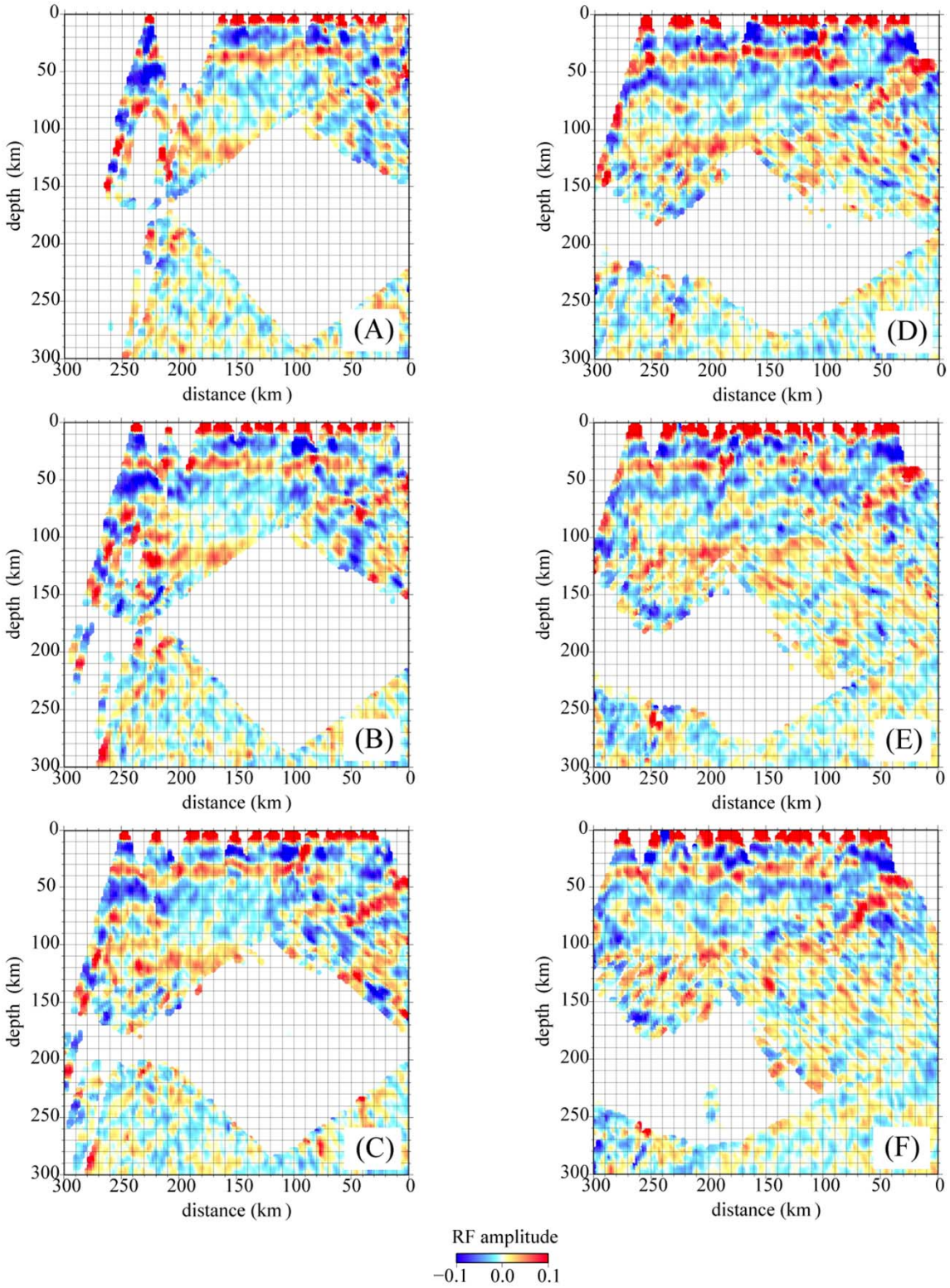

Figure 14 Vectorial RF imaging along dashed lines in Figure 8. Assumed geometry of interfaces for stacking RFs is the same as that in Figure 13.

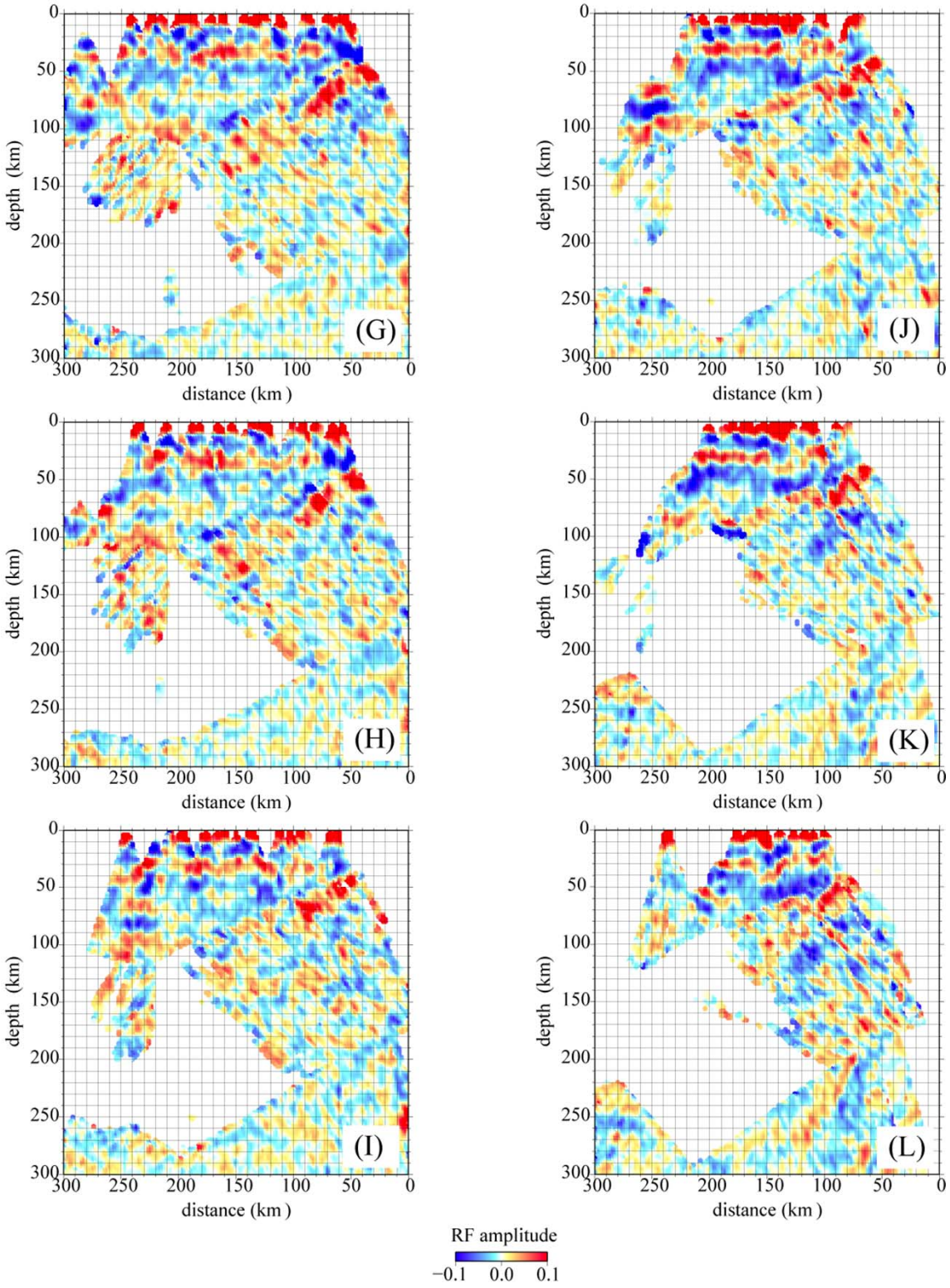

Figure 14 (Continued)

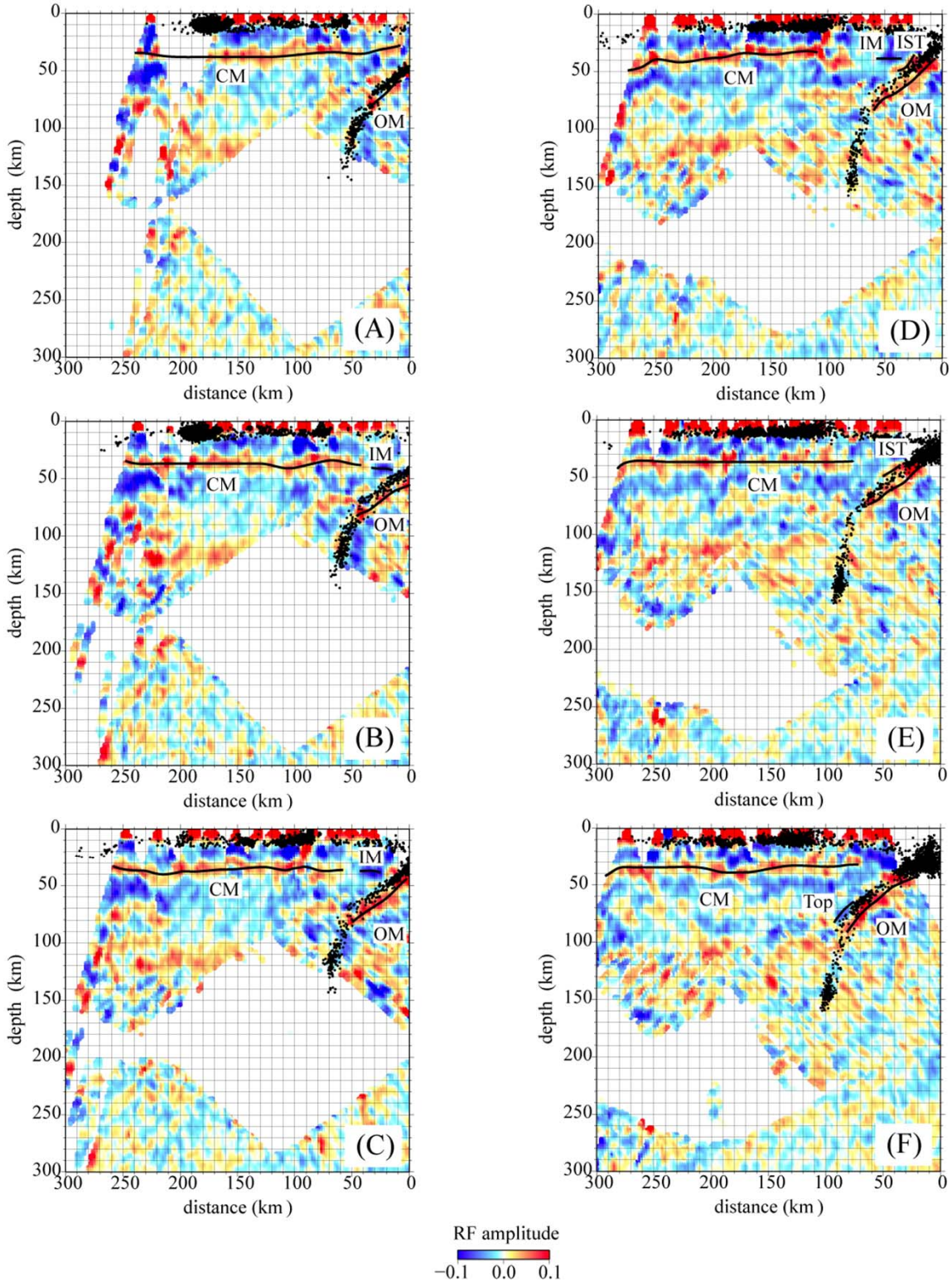

Figure 15 Vectorial RF imaging along dashed lines in Figure 8 obtained after the fourth iteration. Dots and dashed lines indicate the same as in Figure 9. Thick lines indicate detected discontinuities. CM: the continental Moho, OM: the oceanic Moho, IM: the continental Moho with reversed velocity contrast, IST: the upper boundary of the PHS with reversed velocity contrast, Top: the upper boundary of the PHS slab.

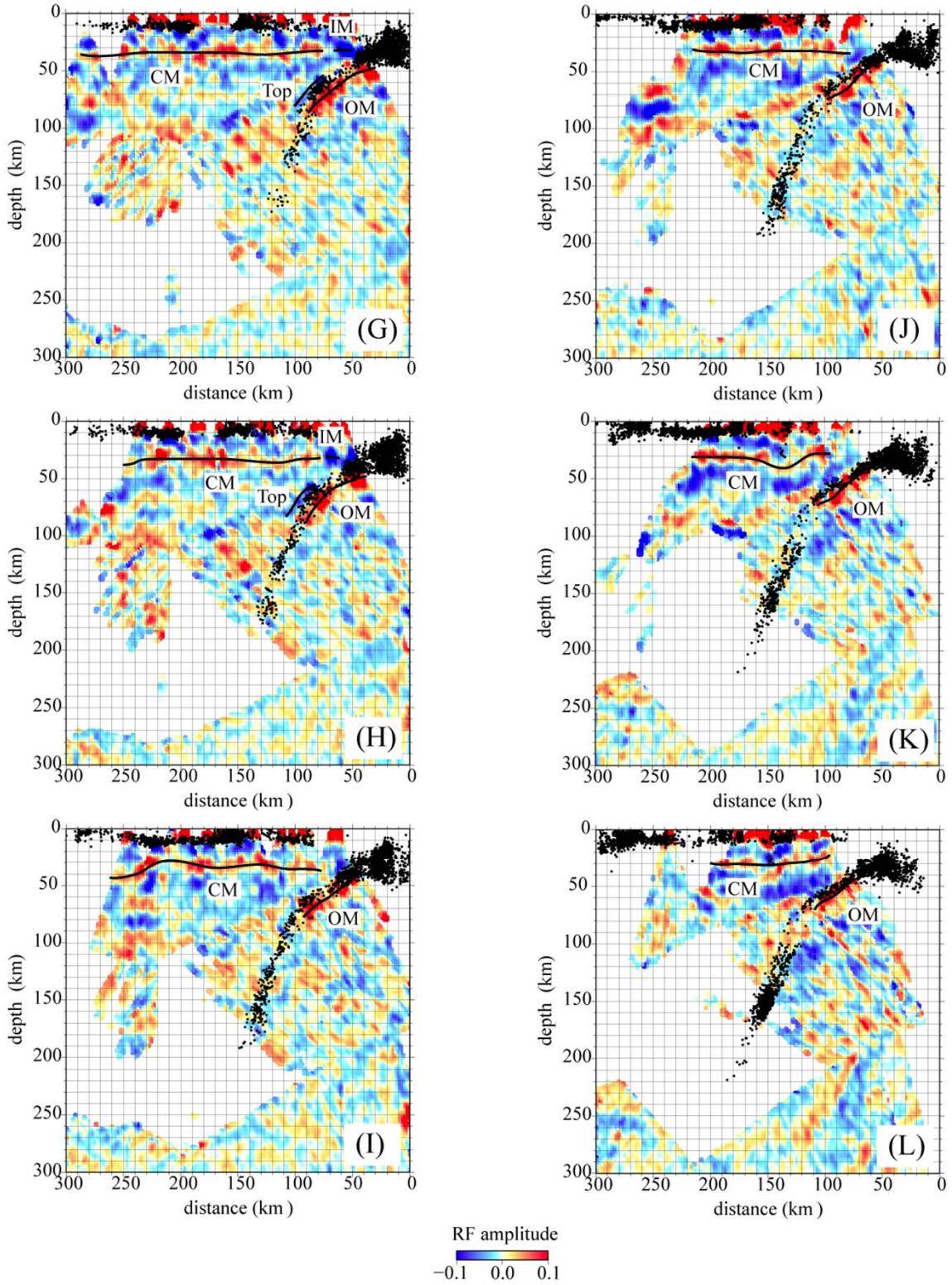

Figure 15 (Continued)

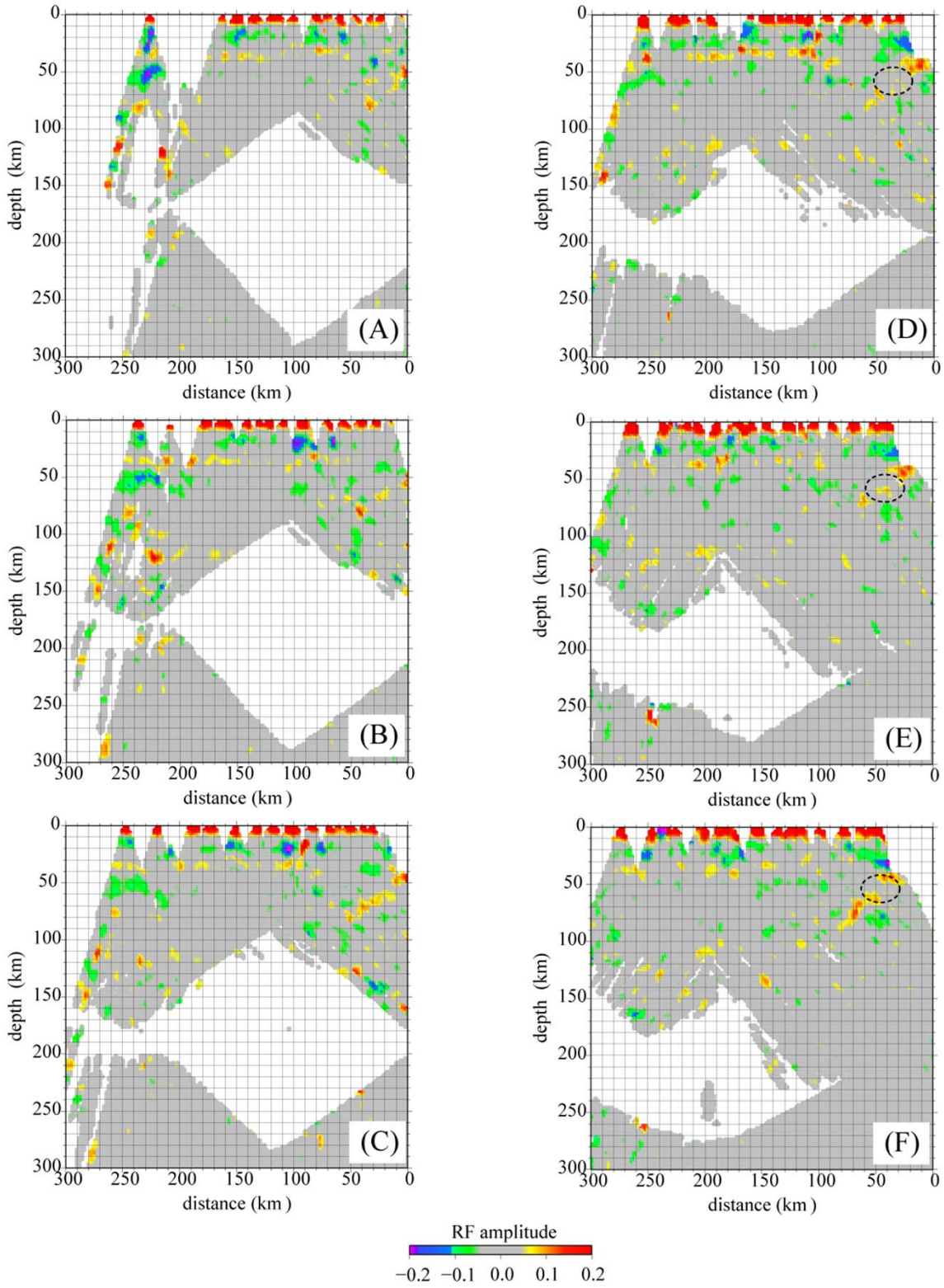

Figure 16 Same as Figure 14, but different color scale is used. Dashed ellipses indicate the small peaks corresponding to the oceanic Moho.

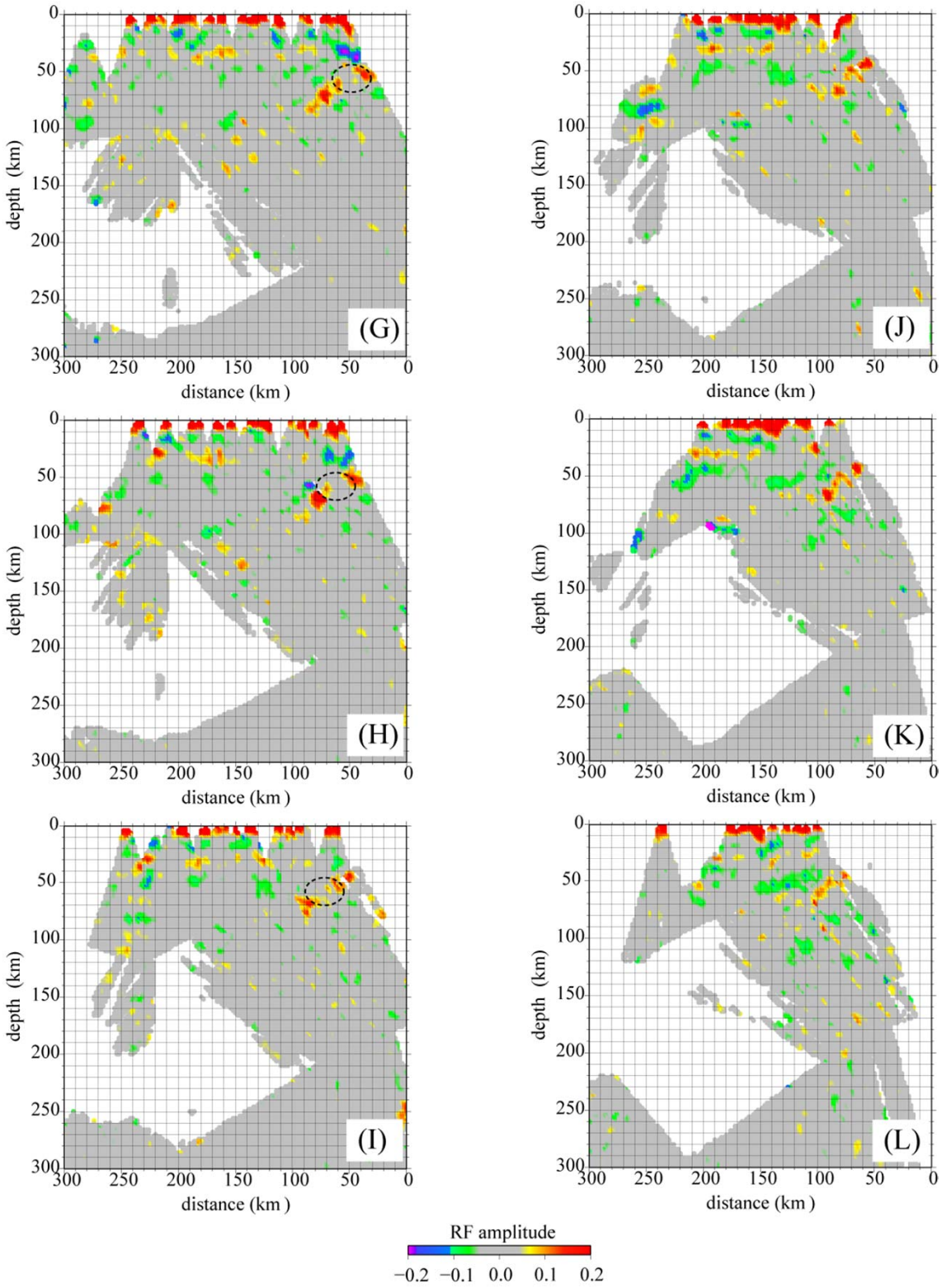

Figure 16 (Continued)

	thickness	Vs	Vp/Vs	density	strike	dip
upper crust	25 km	3.46 km/s	1.68	2.45 g/cm^3	0^o	0^o
lower crust	10 km	3.85 km/s	1.69	2.71 g/cm^3	0^o	0^o
mantle wedge	35 km	4.48 km/s	1.79	3.3 g/cm^3	208^o	?
oceanic crust	8 km	4.30 km/s	1.79	3.2 g/cm^3	208^o	?
mantle		4.77 km/s	1.79	3.4 g/cm^3		

Table 1　Velocity model.

assumed layer at 20-40°, and eliminated 10 of the 26 models whose backazimuths are 75° and 105° because we do not obtain observed teleseismic data from these backazimuths. The 16 selected combinations of dip angles of the low velocity layer, backazimuths and distances of sources are shown in Table 2. The calculated RFs are rotated into the expected vibration directions of shear waves converted at the dipping interface. From the synthesized RFs, we regard the amplitudes of RF peaks corresponding to the lower boundary of the oceanic crust which have 10% lower S-wave velocity than surrounding mantle as 0.054±0.011. To enhance discontinuities which dip at 30-50º and have more than 10% of S-wave velocity contrast, cells with absolute amplitudes less than 0.043 are represented by a shade of grey, and those with absolute amplitudes larger than 0.065 are represented by a pure color in Figure 16.

Positive RF peaks corresponding to the continental Moho appear at depths of 30-40 km (Figure 15). These depths are comparable to those observed in a previous study with the travel times of local earthquakes by *Oda and Ushio* [2007]. The polarity of RF peaks corresponding to the continental Moho is inverted beneath the east coast of Kyushu island beneath lines B, C, D, G and H. Beneath lines B, C, and D, amplitudes of the negative peaks are down to -0.1. Beneath lines G and H, amplitudes of the negative peaks are less than -0.1.

We obtain positive peaks corresponding to the oceanic Moho of the PHS slab (Figure 15). They extend down to 80 km in depth beneath lines A-E, down to 90 km in depth beneath F-I, and down to 70 km in depth beneath J-L. From sections on which dots indicating hypocenters are superimposed, it is understood that there are hypocenters of intermediate-depth earthquakes shallower than the oceanic Moho.

We obtain negative peaks corresponding to the upper boundary of the PHS slab

dip angle	BAZ	DIST	RF amplitude
30	45	60	0.069
30	45	80	0.058
30	165	40	0.063
30	165	60	0.047
30	165	80	0.039
30	195	60	0.072
30	195	80	0.060
40	165	40	0.059
40	165	60	0.051
40	165	80	0.048
40	195	80	0.066
50	135	60	0.036
50	135	80	0.031
50	165	40	0.059
50	165	60	0.051
50	165	80	0.057
		Average	0.054±0.011

Table 2 Amplitude of phase converted at dipping discontinuities on RF

(Figure 15). They exist at depths of 70-80 km beneath line F, at depths of 60-80 km beneath line G and H, respectively. Beneath lines F, G and H, intermediate-depth seismicity at depths of 60-80 km is higher than the surrounding region, and this high seismicity region almost coincides with the region where the upper boundary is detected.

6. Discussion

6.1 Water transportation

6.1.1 Water in the oceanic crust

We have detected the oceanic Moho with downward increasing S-wave velocity, and revealed the portion where the oceanic crust has more than 10% of S-wave velocity contrast. According to *Hacker et al.* [2003a] (Figure 17), the subducting oceanic crust of the PHS slab would maintain an S-wave velocity reduction of at least 10% from the surrounding anhydrous mantle until the stable oceanic crustal rock facies changes from lawsonite + amphibole + eclogite (3.0 wt.% H_2O) to amphibole + eclogite (0.6 wt.% H_2O) or to zoisite + eclogite (0.3 wt.% H_2O). Therefore, the oceanic crust whose lower boundary is indicated by warm colors in Figure 16 would have more than 3.0 wt.% of water content. Many intermediate-depth earthquakes occur above the oceanic Moho. *Hacker et al.* [2003b] and *Yamasaki and Seno* [2003] indicated that dehydration embrittlement is responsible for the occurrence of intermediate-depth earthquakes, and the occurrence of dehydration reactions in the low velocity oceanic crust would be

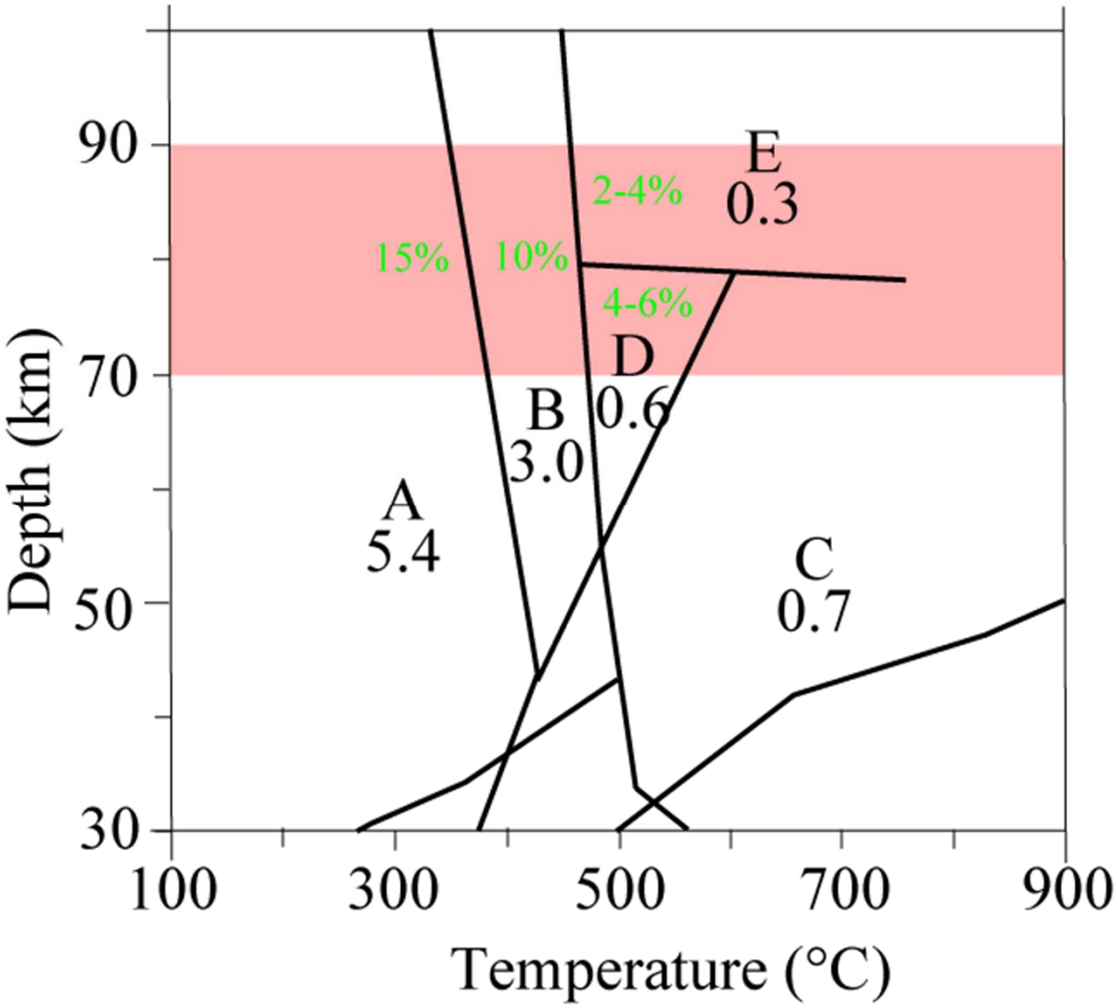

Figure 17 Phase diagram for MORB [*Hacker et al.,* 2003a]. Pressure is converted to the corresponding depth by *Yoshioka et al.* [2008]. A: jadeite+lawsonite+blueschist, B: lawsonite+amphibole+eclogite, C: zoisite+amphibole+eclogite, D: amphibole+eclogite, E: zoisite+eclogite. Black numbers indicate the H_2O content (wt.%). Green numbers indicate decrease ratio of S-wave velocity of the metamorphosed MORB from the unmetamorphsed harzburgite estimated based on *Hacker et al.* [2003a].

implied.

Hirose et al. [2008] estimated the crustal and uppermost mantle structure beneath southwest Japan, with double-difference tomography. They detected a low velocity zone corresponding to the hydrated oceanic crust down to 60 km in depth beneath Kyushu. *Okamoto et al.* [2008] detected intermediate-depth earthquakes whose observed waveforms have later phases implying that they occurred in the low velocity oceanic crust, and focal depth of the deepest event they detected is 60 km. However, we have revealed that the low velocity oceanic crust exists and would bring water down to 70-90 km in depth.

The positive peaks corresponding to the oceanic Moho have small amplitudes at depths of 50-60 km in Figure 16 (D-I). The oceanic crust above the oceanic Moho corresponding to these small peaks might have higher S-wave velocity. In Figure 15 (F-H), intermediate-depth seismicity above the small peaks is lower than above the surrounding oceanic Moho, and might indicate that this part of the oceanic crust has lower water content. However, we cannot expect that the oceanic crust is eclogitized at a depth of about 60 km, because deeper portion of the oceanic crust is expected to have over 3.0 wt.% of water content from RF sections. The oceanic crust of the PHS slab might consist of heterogeneous material or their water content might be heterogeneous, and this heterogeneity might be related to the subduction of the Kyushu-Palau ridge.

6.1.2 Water in the forearc mantle

The seismic velocity structure of the uppermost mantle beneath Kyushu has been estimated with seismic tomography [*Honda and Nakanishi,* 2003; *Wang and Zhao,* 2006, *Xia et al.,* 2008, *Tahara et al.,* 2008]. In these studies, a low V_S and high V_P/V_S region

was detected in the forearc mantle of Kyushu and regarded as a region that is serpentinized by fluid dehydrated from the PHS slab. Our results also indicate that the forearc mantle has extremely low S-wave velocities. In some of our RF sections, the continental Moho beneath the east coast of Kyushu is represented by negative RF peaks (Figure 15 B-H). This occurrence of negative RF peaks implies that the mantle has lower velocity than the continental crust. This unusual occurrence of "inverted Moho" has been also detected beneath Cascadia and northern Chile, and regarded as representing the existence of highly serpentinized mantle [*Bostock et al.*, 2002; *Sodoudi et al.*, 2011]. In Figure 15 (B-D), negative peaks whose amplitudes are between -0.11 and -0.05 corresponding to the continental Moho are detected at distances of 20-30 km, 30-40 km, and 40-50 km, respectively. These negative peaks imply that S-wave velocity of the mantle wedge below is 10-15% lower than that of the lower crust. When S-wave velocity of the continental lower crust is regarded as 3.85 km/s based on the ak135 model [*Kennett et al.*, 1995], the S-wave velocity of the mantle is estimated to be 3.2-3.5 km/s. In Figure 15 (E, F), amplitudes of such negative peaks are larger than -0.05, and S-wave velocity of the forearc mantle is estimated to be higher than 3.5 km/s, less than 10% lower than that of the lower crust. In Figures 15 (G, H), amplitudes of such negative peaks are smaller than -0.17 and between -0.17 and -0.10, respectively, and S-wave velocity of the forearc mantle is estimated to be lower than 2.8 km/s and 2.8-3.2 km/s, respectively. *Saiga et al.* [2010] examined the crustal structure beneath Kyushu with the double-difference tomography, and S-wave velocity beneath the east coast of Kyushu at 30 km in depth was estimated to be 3.6-3.8 km/s. Therefore, velocities of the forearc mantle may be lower than those estimated values.

Ando et al. [2002] analyzed the data of seismic experiments executed in the eastern

part of Kyushu in 1994 and 1996, and revealed that seismic waves reflected at the continental Moho were not detected. We can also expect that the forearc mantle has low seismic velocity from their results. We show a RF section along the survey line of the seismic experiments in Figure 18. In the section, although consecutive positive peaks corresponding to the continental Moho exist at distances of 0-60 km from the north end, clear peaks corresponding to the continental Moho do not appear beneath the other region.

In Figure 15 (D, E), positive peaks corresponding to the upper boundary of the slab are obtained. This fact implies that the forearc mantle has lower S-wave velocity than that of the oceanic crust, and is also an evidence that S-wave velocity of the forearc is extremely low.

In Figure 19, we show relationships between S-wave velocity of peridotite and volume percent lizardite and between S-wave velocity of peridotite and volume percent antigorite measured by *Christensen* [2004]. Because chrysotile has velocities similar to lizardite [*Christensen,* 2004], we assume that effect of volume percent chrysotile on S-wave velocity of peridotite is the same as that of volume percent lizardite. In Figure 19, S-wave velocities of lizardite-chrysotile serpentinites and antigorite serpentinites are 2.3 km/s and 3.6 km/s, respectively. Therefore, lizardite-chrysotile serpentinites would exist beneath the inverted Moho beneath lines B-H, rather than antigorite serpentinites. If lizardite-chrysotile serpentinites are the sole cause to reduce S-wave velocity of the forearc mantle, the degrees of serpentinization are estimated to be 50-60%, less than 50%, greater than 80%, and 60-80% beneath lines (B, C, D), lines (E, F), line (G), and line (H), respectively. However, while stable temperature of lizardite-chrysotile serpentinites is lower than 300ºC [*Christensen*, 2004], the forearc mantle may not have

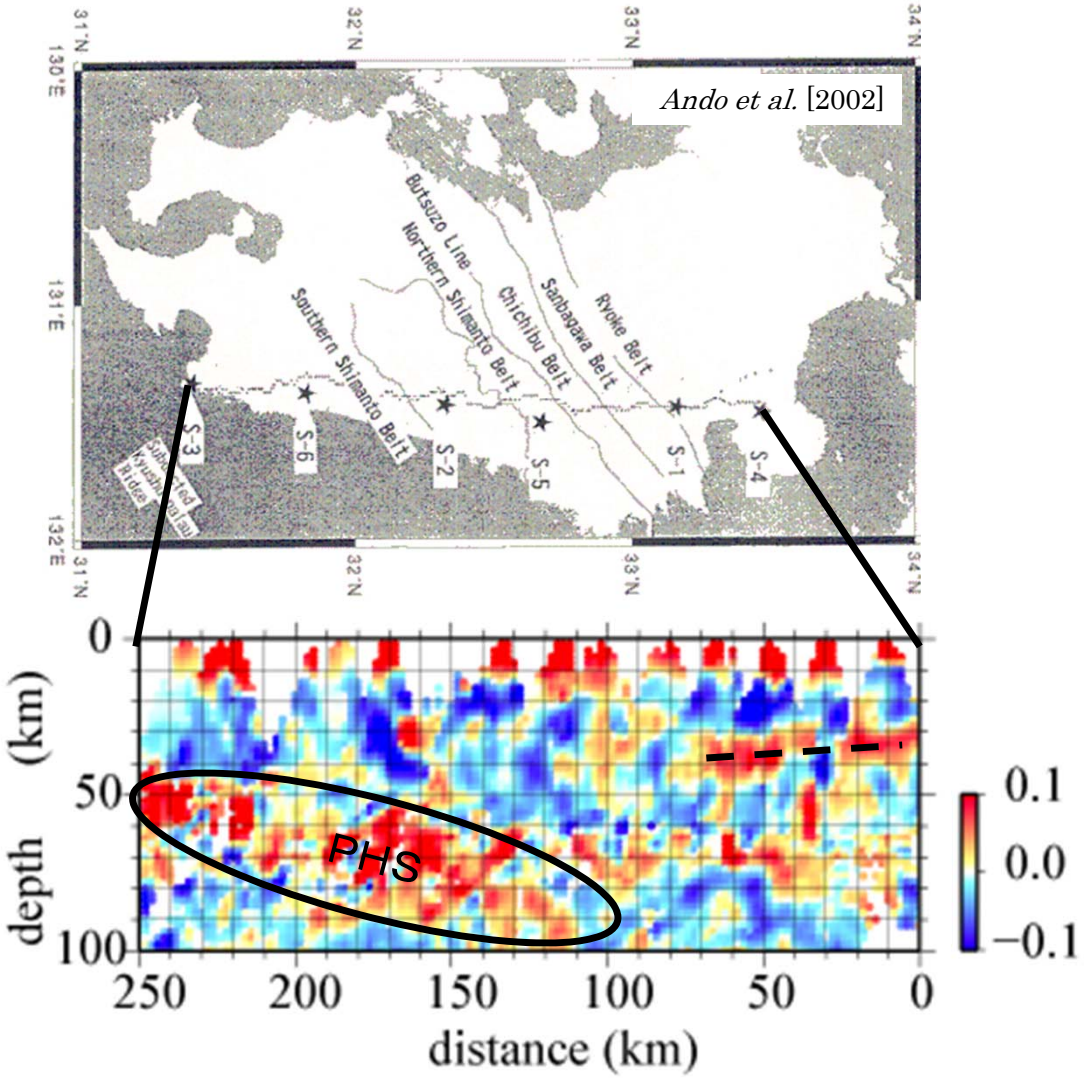

Figure 18 Vectorial RF image beneath the survey line of the seismic experiment by *Research Group for explosion seismology* [1999a, b]. Dashed line indicates the positive peaks which are interpreted to corresponds to the continental Moho. Ellipse indicates the positive peaks which are interpreted to correspond to the oceanic Moho of the PHS slab.

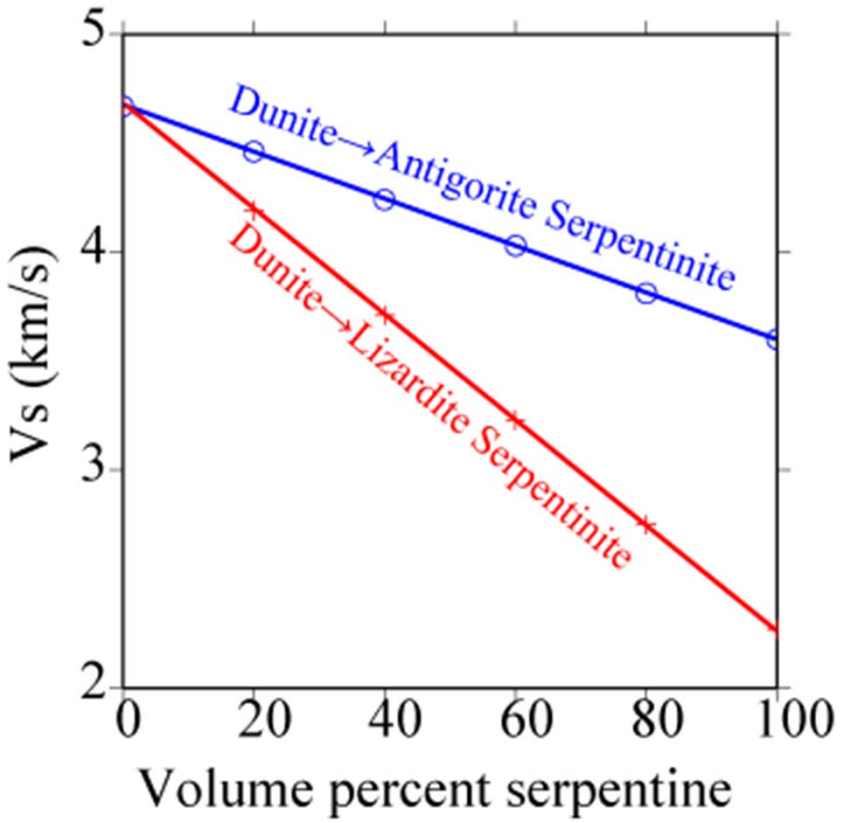

Figure 19 S-wave velocity of peridotite versus volume percent antigorite (blue) and lizardite (red) [*Christensen,* 2004].

such a low temperature according to the results of temperature calculations by *Yoshioka et al.* [2008]. *Christensen* [1989] measured seismic velocity of lherzolite with 3.9% of porosity at a confining pressure of 150 MPa. They revealed that increase in pore pressure from atmospheric to 130 MPa decreases S-wave velocity of the medium from 4.15 km/s to 3.18 km/s. High pore pressure can significantly reduce seismic velocities of rocks and may be one of the causes to reduce S-wave velocity of the forearc mantle.

A serpentinite layer on the top of the slab is believed to cause an aseismic slip and control the downdip limit of the seismogenic zone at a plate boundary [*Hyndman and Peacock*, 2003]. *Tahara et al.* [2008] revealed with double-difference tomography that aseismic and coseismic slip zones beneath the east coast of Kyushu detected by *Yagi and Kikuchi* [2003] coincide with portions having high and low Poisson's ratios, respectively. We do not detect discontinuities beneath Hyuga-nada which is a part of the study area of *Yagi and Kikuchi* [2003] because of absence of seismic data. However, the forearc mantle beneath lines (G, H) which is expected to have extremely low S-wave velocity (less than 3.2 km/s), coincides with the weakest interplate coupling area in the study area of *Yagi and Kikuchi* [2003]. Therefore, the existence of highly serpentinized material and/or free water in the forearc may characterize the fault-slips.

6.1.3 Water at the bottom of the mantle wedge

Free water derived from dehydration reaction of the oceanic crust would flow into the mantle wedge and hydrate it [e.g. *Hyndman and Peacock*, 2003]. Then, seismic velocity of the hydrated mantle would be reduced. In many of the RF sections, RF peaks corresponding to the upper boundary of the PHS slab are not detected clearly, and it is expected that the mantle above the boundary is serpentinized by free water from the

oceanic crust and has about the same S-wave velocity as the oceanic crust below it.

However, negative peaks which would be corresponding to the upper boundary of the PHS slab clearly appear in RF sections (F, G, H) at depths of 60-80 km in Figure 15. The portion below the discontinuity is estimated to have a little less than 10% lower S-wave velocity than the portion above it, and the discontinuity exists down to the depth where the oceanic crust has been eclogitized. This fact would imply that the mantle wedge above the discontinuity has little or no water content. We suggest here two of the possible causes for the little water content.

One of the possible causes is that temperature of the mantle wedge is higher than the stable temperature of serpentinite. Rock facies of the hydrated oceanic crust, jadeite + lawsonite + blueschist or lawsonite + amphibole + eclogite, are stable up to 420°C or 480°C, respectively, and serpentinized peridotite is stable up to 620°C [*Hacker et al.*, 2003a]. Therefore, a temperature transition from 420-480°C to 620°C would exist around the discontinuity, and serpentinized mantle and/or the anhydrous oceanic crust may exist between the anhydrous mantle and the hydrous oceanic crust. We estimate the thickness and temperature gradient with forward modeling of RFs. The sections of RFs calculated with a 0.92 Hz Gaussian low pass filter are shown in Figure 20. In Figure 20, we also plot arrival time differences between direct P and Ps converted phases on the conversion points. From Figure 20(b), it is understood that time width of negative peaks is about 1.0 s. Next, we calculate RFs from waveforms synthesized with GRT assuming velocity models (shown in Table 3) which have various thickness of the transition zone. In table 4, we show the relationship between width of RF peak and the transition zone thickness. Width of the negative peaks corresponding to the transition zone is 1.0 s when the thickness is assumed to be 3 km. Therefore, the temperature gradient about

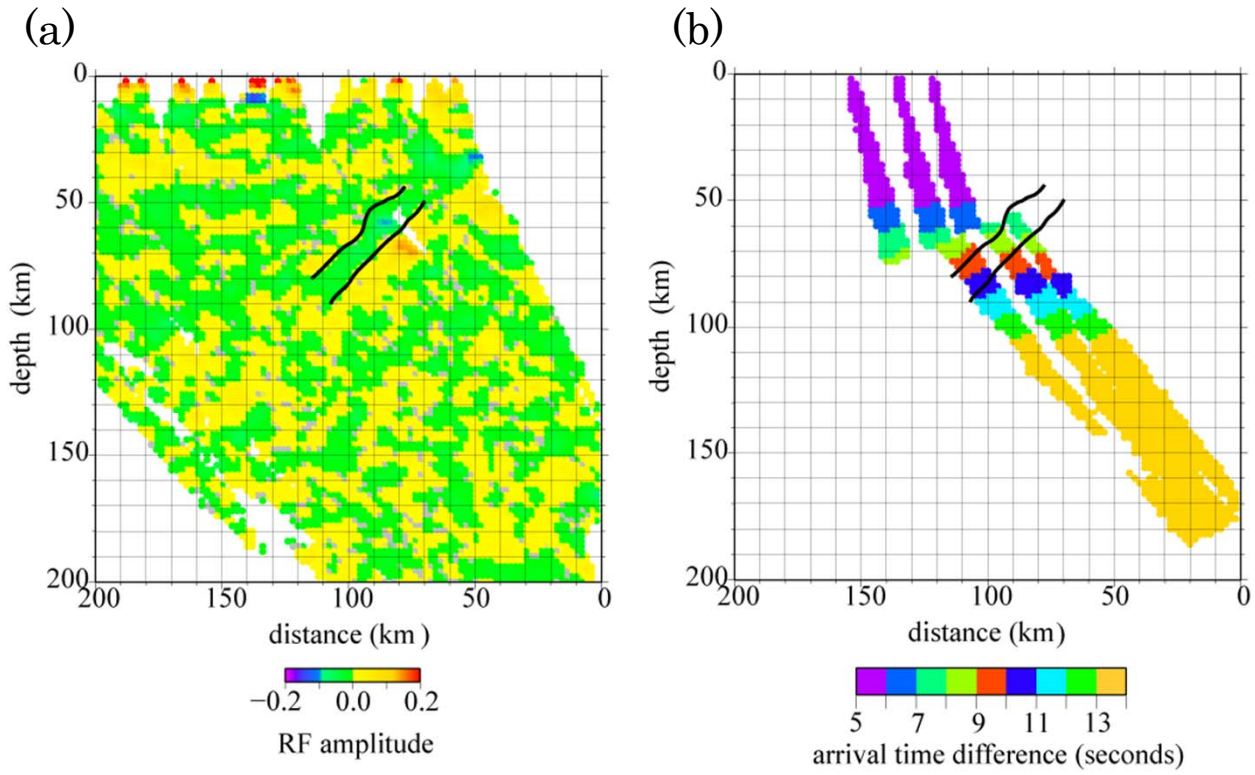

Figure 20　Two RF sections beneath line H in Figure 8. Black lines indicate width of the negative peaks corresponding to the upper boundary of the PHS slab. (a) Vectorial RF image. (b) Arrival time difference between direct P and Ps converted phases at stations ASKH, HYOH and UWEH.

	thickness	Vp	Vs	density
layer1	35 km	5.81 km/s	3.46 km/s	2.45 g/cm^3
layer2	(65 - 4h) km	8.40 km/s	4.77 km/s	3.40 g/cm^3
layer3	h km	8.93 km/s	4.70 km/s	3.15 g/cm^3
layer4	h km	8.74 km/s	4.60 km/s	3.15 g/cm^3
layer5	h km	8.55 km/s	4.50 km/s	3.15 g/cm^3
layer6	h km	8.36 km/s	4.40 km/s	3.15 g/cm^3
layer7	10 km	7.70 km/s	4.30 km/s	3.20 g/cm^3
layer8		8.40 km/s	4.77 km/s	3.40 g/cm^3

Table 3　Model for confirming the relationship between transition zone thickness and width of RF peaks corresponding to the transition zone. Layer 3-6 represent the transition zone, and we can set thickness of the transition zone by determining h arbitrarily.

h	negative peak width	thickness of transition zone
0 km	0.85 s	0 km
0.25 km	0.90 s	1 km
0.5 km	0.95 s	2 km
0.75 km	1.00 s	3 km
1.00 km	1.05 s	4 km
1.25 km	1.15 s	5 km
1.5 km	1.25 s	6 km
1.75 km	1.40 s	7 km
2.00 km	1.55 s	8 km

Table 4 Relationship between h shown in Table 2 and width of the negative peak of RF which is generated assuming the model shown in Table 2.

40-50ºC/km is expected to exist around the boundary. We can also expect such a large temperature gradient from the results of temperature calculations by *Yoshioka et al.* [2008].

However, *Abers* [2005] indicated another possible cause for existence of the sharp discontinuity at the upper boundary of a slab. They estimated the reduction of seismic velocity of the oceanic crust from the surrounding mantle in seven circum-Pacific subuduction zones, and revealed the velocity reduction at depths of 100-150 km is correlated to the dip angle of the slab. From the results, they expected that, in steeply dipping slabs, fluid dehydrated from the oceanic crust may travel up-dip through permeability fabric oriented parallel to the slab surface. If little fluid flows vertically to the mantle wedge, it will not become serpentinized and a sharp velocity contrast would exist at the upper boundary of the slab, regardless of temperature gradient. In our RF sections, the upper boundary of the slab corresponds to negative peaks beneath lines F, G and H, and impermeable boundary might exist there. Beneath the region, a remnant island arc, Kyushu-Palau ridge, is subducting (Figure 9), and such an impermeable boundary might related to the remnant island arc.

6.1.4 Water in a high seismicity portion of the oceanic crust

In Figure 15 (F, G, H), activity of intermediate-depth earthquakes is higher at depths of 60-70 km than the surrounding region. It is understood that these earthquakes indicated by dots in Figure 15 (F, G, H) occurred in the oceanic crust. RF peaks corresponding to the upper and lower boundaries of the oceanic crust are larger than the surrounding portion, and this fact implies that S-wave velocity of the high seismicity region is lower. Abundant free water may exist in the oceanic crust at depths of 60-70

km, and cause a decrease in S-wave velocity coincident with an increase in seismic activity. High heat flow from the mantle wedge to the PHS slab would cause a rapid temperature increase in the subducting oceanic crust, and a large amount of fluid is expected to be generated by dehydration reactions. Alternatively, fluid dehydrated from a deeper portion of the oceanic crust might flow up-dip in the slab and concentrate there.

6.2 Implications for volcanism

In our study area, the oceanic crust would bring down to 90 km in depth at a maximum beneath the sections F, G and H. Around these portions, the Kyushu-Palau ridge would be subducting. According to *Hacker et al.* [2003a], the colder oceanic crust would dehydrate deeper. The Kyushu-Palau ridge may be colder than the surrounding portion of the oceanic crust and bring water at deeper portion. In fact, the heat flow values in the Hyuga-nada region, where Kyushu-Palau ridge is subducting, are estimated to be low (<45mW/m^2) by *Ashi et al.* [1999]. However, the depth where the oceanic crust has been dehydrated does not largely vary along strike direction of the slab. On the volcanic front of Kyushu, there is about 110 km gap of volcanic activity between Aso and Kirishima volcanoes (Figure 1). Therefore, we interpret that this gap is not caused by the oceanic crust dehydrated at shallow portions beneath the gap region or the not-hydrated oceanic crust from the beginning of the subduction. For example, *Aoki and Kagiyama* [2006] revealed with GPS analysis that the crust of the central Kyushu region is subjected to compressional stress, and indicated that the compressional stress causes absence of volcanism in the central Kyushu region.

From our results, it is understood that the oceanic crust of the PHS slab would bring water below the forearc region or just below the volcanic front. However, we do not reveal whether or not fluid is conveyed deeper after it is evolved because many of our RF sections have large noise at about 100-150 km in depth. Serpentinite layer at the bottom of the mantle wedge is interpreted to convey water deeper than the depth at which the oceanic crust has been eclogitized, and fluid dehydrated from the serpentinized layer is thought to cause arc volcanism in NE Japan [*Nakajima et al.*, 2001; *Kawakatsu and Watada*, 2007]. Therefore, it is important to verify the presence of the serpentinized layer and the depth where fluid is released from it for understanding the process of volcanic activity in Kyushu.

7. Conclusions

We have developed a method to stack RFs by considering the refraction of seismic rays at dipping interfaces. Although the geometry of interfaces dipping at 30-70˚ cannot be correctly imaged without considering refraction in P-to-S conversion at dipping interfaces, such a geometry can be correctly estimated when we use this method.

Beneath Kyushu, the subuducting oceanic crust of the PHS slab contains more than 3.0 wt.% of water and brings water down to 70-90 km in depth. This hydrated portion of the oceanic crust would have a low S-wave velocity (more than 10% lower than the slab mantle), and cause a velocity contrast at the oceanic Moho. While the oceanic crust is subducting, dehydration reactions would gradually occur within it with increasing pressure and temperature, and cause the seismic activity in the oceanic crust. Almost all

fluid in the oceanic crust would have been lost at depths of 70-90 km, which is coincident with the disappearance of velocity contrast at the lower (and upper) boundaries of the oceanic crust. The depth where the oceanic crust has been dehydrated does not largely vary along the strike direction of the slab, and the gap of volcanic activity on the volcanic front between Aso and Kirishima would not be caused by the fact that the oceanic crust beneath the gap has been dehydrated at shallower portion than beneath the other region or is not hydrated from the beginning of the subduction.

Dehydrated fluid from the oceanic crust would flow to the mantle wedge. Beneath the forearc region, such fluids would hydrate the mantle material and cause the reduction of seismic velocity. Beneath lines B, C, D, G and H, S-wave velocity estimated from amplitudes of the negative peaks corresponding to the continental Moho is especially low (2.8-3.5 km/s), and the cause of such a low S-wave velocity may be the existence of serpentinite and/or free fluid with high pore pressure.

Beneath lines F, G and H, a sharp discontinuity with upward increasing seismic velocity exists at the upper boundary of the PHS slab. S-wave velocity of the mantle wedge above the boundary would not be low, and would have little or no water content. Unless a permeability barrier exists at the upper boundary of the slab, fluid dehydrated from the oceanic crust would flow vertically. In this case, a large temperature gradient (40-50ºC/km) that is subperpendicular to the slab may exist around the boundary, and serpentinite above the boundary may become unstable.

Abundant free fluid may exist in the oceanic crust at depths of 60-70 km beneath lines F, G and H, and cause a decrease in velocity in the high seismicity portion.

III. Crustal structure beneath Aso caldera, Japan

1. Introduction

Aso Volcano rises in the Kyushu district, southwest Japan, where the Philippine Sea plate is subducting beneath the Eurasian Plate (Figure 1). Aso is one of the most active volcanoes in Japan and has a caldera with dimensions of 18 km by 25 km, one of the largest in the world (Figure 21). Aso experienced four huge pyroclastic eruptions (266 ka, 141 ka, 123 ka, 89 ka) [*Matsumoto et al.*, 1991]. The last one (Aso-4 eruption) ejected over 600 km^3 of deposits and formed the present caldera [*Committee for Catalog of Quaternary Volcanoes in Japan*, 1999].

The seismic velocity structure shallower than 10 km beneath Aso Caldera has been estimated with seismic tomography by *Sudo and Kong* [2001] who detected a low velocity zone which is roughly spherical in shape centered at a depth of about 6 km below the central cones of the volcano (Figure 21). P- and S-wave velocities of its center were estimated lower than 4.5 km/s and 2.5 km/s, respectively. They interpreted the low seismic velocity sphere to be a magma chamber. The radius of this chamber is 2 or 3 km, its volume is about 100 km^3, and no other magma chamber in the crust shallower than 10 km was found. *Sudo et al.* [2006] detected a deflation source at the vicinity of the spherical chamber based on leveling survey data, and mentioned that only a few percent melt content is needed to explain the obtained low velocity of the sphere. The dense rock equivalent volume of the pre-eruptive magma of Aso-4 was estimated to be more than 200 km^3 [*Kaneko et al.*, 2007]. The spherical magma chamber detected by *Sudo and Kong* [2001] alone cannot eject as much material as was

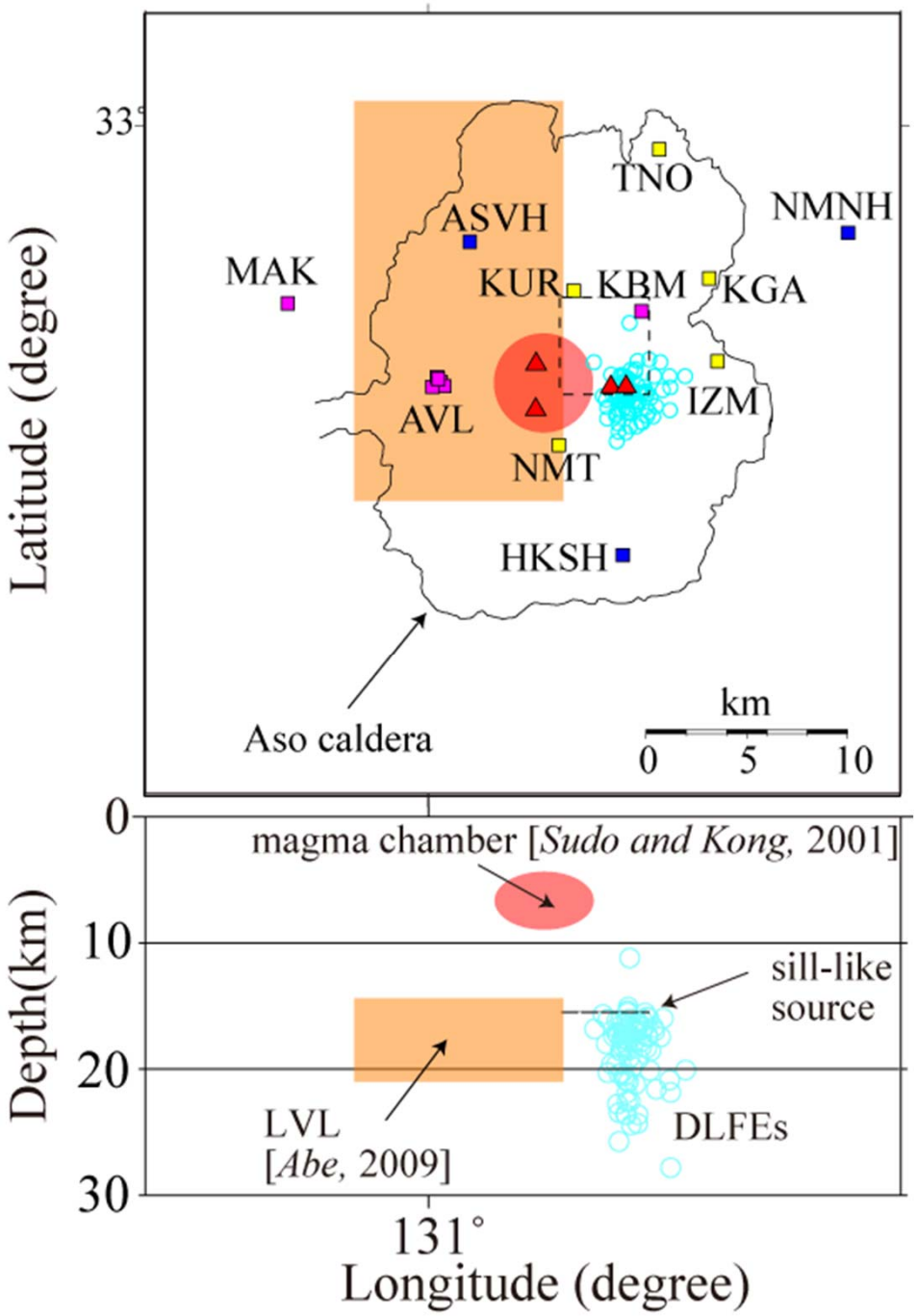

Figure 21 Upper, map of Aso caldera. Solid line indicates the rim of Aso caldera. Triangles indicate the summits of the central cones. Red circle indicates the spherical magma chamber detected by *Sudo and Kong* [2001]. Dashed box indicates the sill-like dilatation source detected by *Geographical Survey Institute* [2004]. Small light blue circles indicate the hypocenters of deep low frequency events (DLFEs, origin time: September 1999-March 2007) determined by JMA. Orange box indicates LVL detected by *Abe* [2009]. Blue and purple squares indicate the locations of seismic stations of Hi-net and AVL. Yellow squares indicate the locations of temporal seismic stations. Lower, east-west vertical section where all the subsurface features in the map of Aso caldera are projected. Red ellipsoid, dashed line, yellow box and light blue circles are corresponding to magma chamber, sill-like deformation source, LVL and hypocenters of DLFEs, respectively.

deposited in the Aso-4 eruption, even if all the magma in the chamber erupted.

Existence of fluid in the deep portion of the crust beneath Aso caldera has been expected geophysically and geochemically. *Geographical Survey Institute* [2004] reported that a sill-like dilatation source is located at a depth of 15.5 km (Figure 21) and its 70 cm opening in vertical direction caused crustal deformation in the middle of 2003 from GPS measurements. Later, *Ohkura and Oikawa* [2008] observed that the sill-like deformation source has been compressing since 2004 with GPS data. Deep low frequency earthquakes (DLFEs) have also been observed beneath the sill-like deformation source (Figure 21), which is a possible signal of fluid movement in depth [*Ukawa and Ohtake*, 1987; *Nakamichi et al.*, 2003]. *Kaneko et al.* [2008] analyzed trace elements of volcanic rocks of Aso volcano, and indicated that magmas of its huge pyroclastic eruptions were derived from the molten gabbroic lower crust melted by high-temperature melt intruded into the crust from the mantle. Therefore, it is possible that the crust deeper than 10 km beneath Aso caldera reserve magmas which will eject at the next huge eruption, and it is important to examine the structure carefully for understanding the process of preparation for a catastrophic eruptions.

The crustal S-wave velocity structure beneath a part of Aso caldera has been estimated with genetic algorithm (GA) inversion of RFs by *Abe* [2009] who detected a low S-wave velocity layer (LVL) at depths of 15-21 km beneath the western part of the caldera. S-wave velocity of LVL was estimated to be 2.3 km/s. He concluded that LVL contains more than 2% of aqueous fluid or melt. However, he could not reveal the crustal structure beneath whole part of Aso caldera because of sparse distribution of seismic stations especially at the eastern part of the caldera.

In order to detect further evidence of the process of magma activity of Aso volcano,

including its large eruptions, we examine the crustal structure beneath Aso caldera with GA inversion of RFs using more abundant data from denser distributed seismic stations in Aso caldera than *Abe* [2009].

2. Data

We use waveform data of teleseismic events (epicentral distance: 30-90º, magunitude: over 5.5, origin time: 2001-2011). The waveform data was observed at parmanent stations of Aso Volcanological Laboratory, Kyoto University (AVL, KBM, MAK) and stations of Hi-net (ASVH, HKSH) [*Obara et al.*, 2005]. We also use waveform data of temporal stations in Aso caldera which we set in June and July 2009 (KUR, KGA, IZM, NMT, TNO). Epicentral distribution of the teleseismic events is shown in Figure 22, and distribution of all the stations is shown in Figure 21.

2-1. Stations of Aso Volcanological Laboratory

We use 6 permanent stations established by AVL. 4 stations of them (AVL) are equipped with well calibrated seismometers with a natural period of 1 s (Katsujima SD203B). Station KBM is equipped with well calibrated seismometers with a natural period of 0.8 s (Katsujima SD110). Station MAK is equipped with a broad-band seismometer (Guralp Systems CMG-40T).

2-2. Temporal stations in Aso caldera

We set 5 seismic stations in Aso caldera and started observations in June 2009

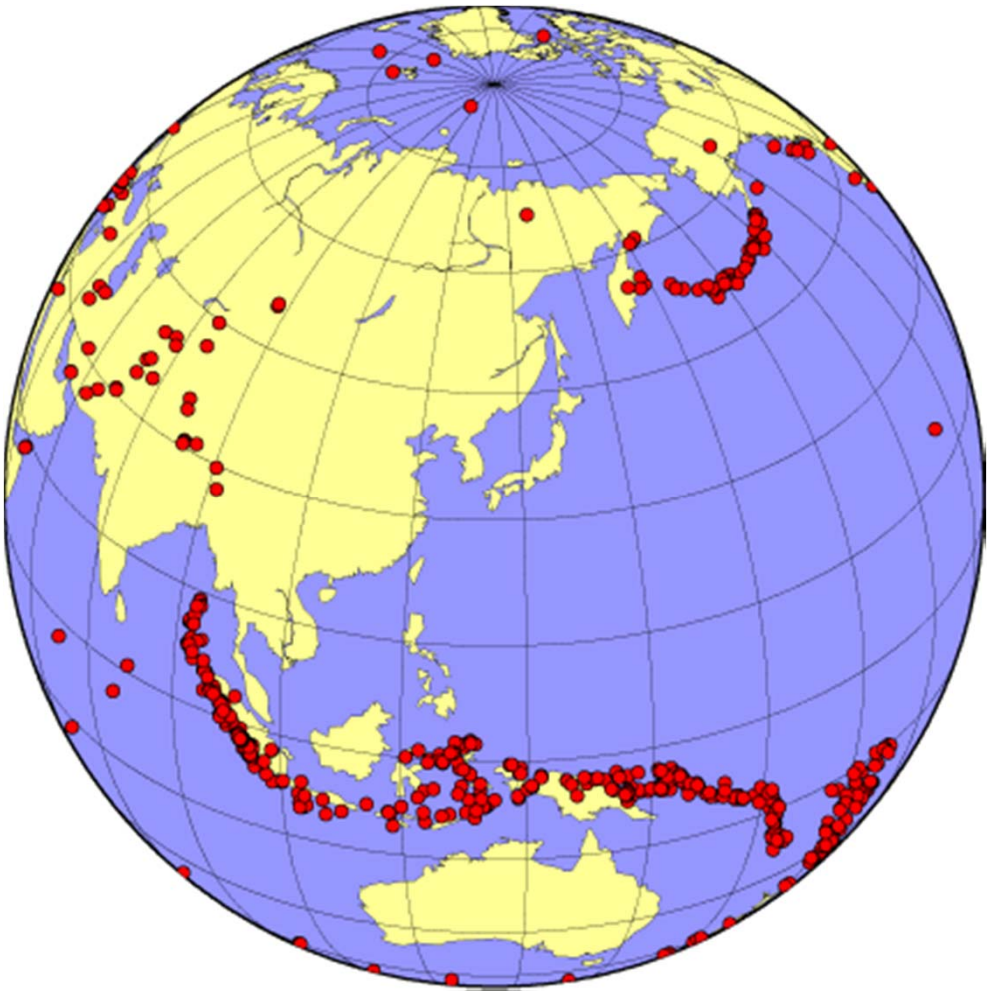

Figure 22 Epicenters of teleseismic events used in chapter III.

(NMT) and July 2009 (KUR, KGA, IZM, TNO). Their locations are shown in Figure 21. These stations are equipped with a three component short-period (1 s) seismometer (Sercel L-4C-3D). We use data loggers (Kinkei System EDR-X7000) to record waveforms. The seismic waveforms are digitized by 18-bit A/D converters with a sampling frequency of 250 Hz and stored in CF cards. The internal crystal clock in the logger is corrected by a GPS timing signal so that timing error is assured to be less than 1 ms. We have evaluated a damping factor and a natural period of each the seismometers using signal calibration methods [*Rodgers et al.*, 1995].

3. Analyses

3.1 Processing of data

RFs have been calculated from teleseismic waveforms with the extended-time multitaper method [*Helffrich*, 2006] modified by *Shibutani et al.* [2008].

In Figure 23(a), we show a RF section beneath line D in Figure 8 which crosses Aso caldera. Although positive RF peaks corresponding to the continental Moho exist at depths of 30-40 km at distances of 100-200 km in the section, two discontinuities are detected by positive peaks beneath Aso caldera. One exists at a depth of about 30 km, and the other exits at a depth of about 45 km. *Abe* [2009] revealed that positive peaks corresponding to the continental Moho appear at 35-40 km in depth beneath Aso caldera in the section without RFs calculated with waveform data observed stations inside the caldera (Figure 23(b)). They elucidated with forward modeling of RF that RFs which

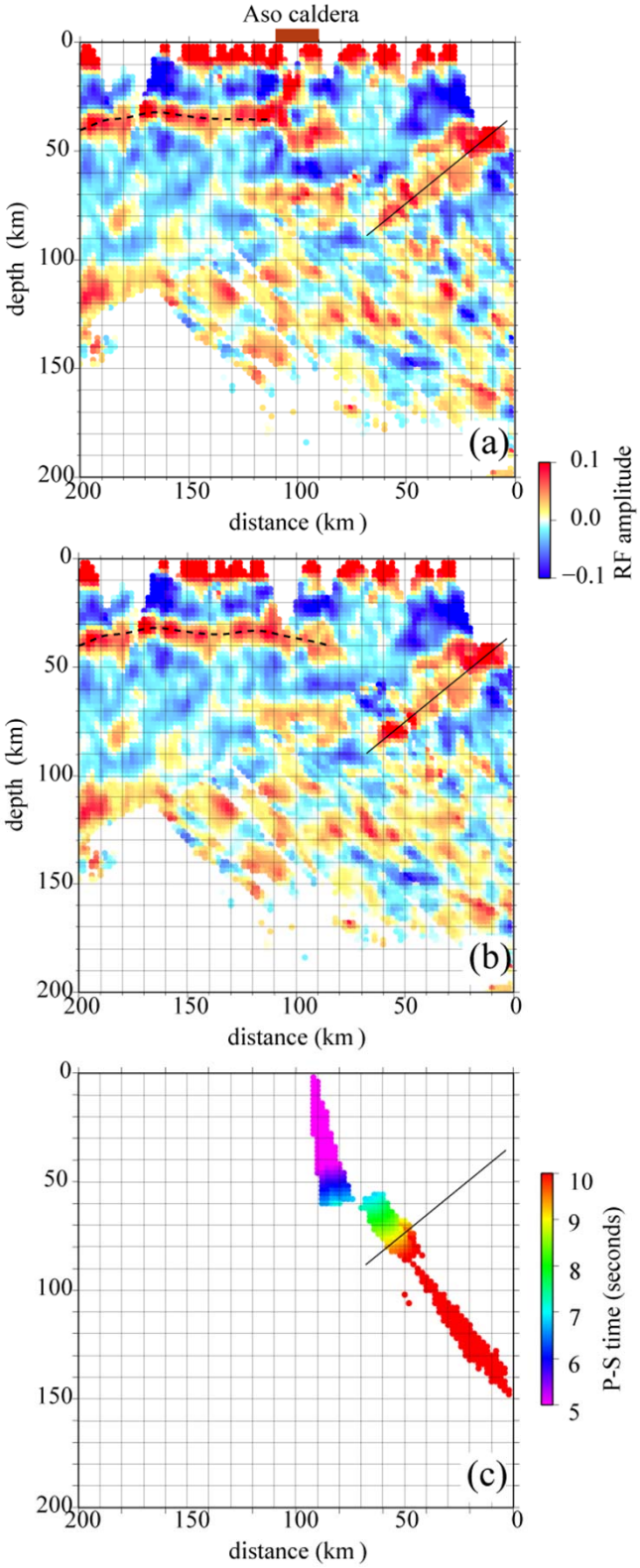

Figure 23 RF sections beneath line D in Figure 8. Solid black lines indicate the positive peaks corresponding to the oceanic Moho of the PHS slab. Dashed black lines indicate the positive peaks corresponding to the continental Moho. (a) Vectorial RF image. (b) Same as (a) but RFs observed at ASVH and HKSH which locate inside Aso caldera are eliminated. (c) Arrival time difference between direct P and Ps converted phases at station NMNH.

are converted to depth domain would have two positive peaks at about 30 km and 45 km in depth if low velocity (V_S=2.4 km/s) layer exists beneath station at depths between 14-19 km and the continental Moho exists at 37 km in depth. If such a low velocity layer exists only beneath Aso caldera, teleseismic waves observed outside the caldera, which pass through the continental Moho beneath Aso caldera and do not pass through the low velocity layer, produce depth domain RFs which have positive peaks at depths of 35-40 km beneath the caldera. Therefore, they concluded that a low velocity layer exists beneath Aso caldera. In this thesis, we also assume the existence of the low velocity layer and estimate S-wave velocity structure from the observed RFs with genetic algorithm inversion.

In Figure 23(c), we show the Ps conversion points of teleseismic waves impinging station NMNH which was estimated in chapter II. Colors of the points in Figure 23(c) indicate arrival time differences between direct P and Ps converted phases. From Figure 23(c), shear waves converted at the oceanic Moho would arrive at station NMNH about 9 seconds after the arrivals of direct P-waves, and the first 7 seconds portion of observed RFs would not be contaminated shear waves converted at boundaries of the PHS slab. In order to estimate crustal structure, therefore, we use the first 7 seconds portion of observed RFs, and assume that all peaks on the portion are caused by scattering or reverberation in the continental crust.

In Figure 21, there are 4 stations named AVL. These 4 stations are close to each other, and we treat all RFs estimated from data of the 4 stations as RFs estimated from data of a station named AVL.

RFs for each station are grouped in every 15º of backazimuth, and stacked. Stacked RFs have averaged back azimuth and ray parameter. For example, group of RFs whose

backazimuths are between 0º and 15º of station AVL is named AVL-000-015. We estimate subsurface structure using these RFs of groups in which more than 10 RFs are stacked. To check stability of a stacked RF, we calculate standard deviations of observed RFs for each group at 141 sampling points in 0-7 seconds, and average them. We do not use stacked RFs of groups whose averaged standard deviation is over 0.1 for structure estimation.

In this study, we estimate the subsurface structure only from radial RFs assuming that the crust consists of horizontally layered isotropic media. However, if subsurface structure beneath a station has dipping discontinuities or portions which consist of anisotropic media, they will affect radial RFs. Although it is difficult and requires careful handling of RFs to estimate effects by geometry of discontinuities and seismic anisotropy, we easily estimate how large the dipping and anisotropic structures beneath stations affect radial RFs here. We define the effect by $E(t) = \sqrt{RF_R(t)^2 + RF_T(t)^2} - \sqrt{RF_R(t)^2}$, where $RF_R(t), RF_T(t)$ indicate radial and transverse RF, respectively, and t indicates the sampling time points. We select and invert RFs whose $E(t)$ do not exceed 0.2.

We show all stacked RFs of groups in which more than 10 RFs are stacked in Figure 24. We indicate groups which have a stacked RF whose averaged standard deviation is over 0.1 with white circles, groups whose transverse RF has more than one sampling point on which $E(t)$ is over 0.2 with black circles and the other groups with red circles in Figure 25.

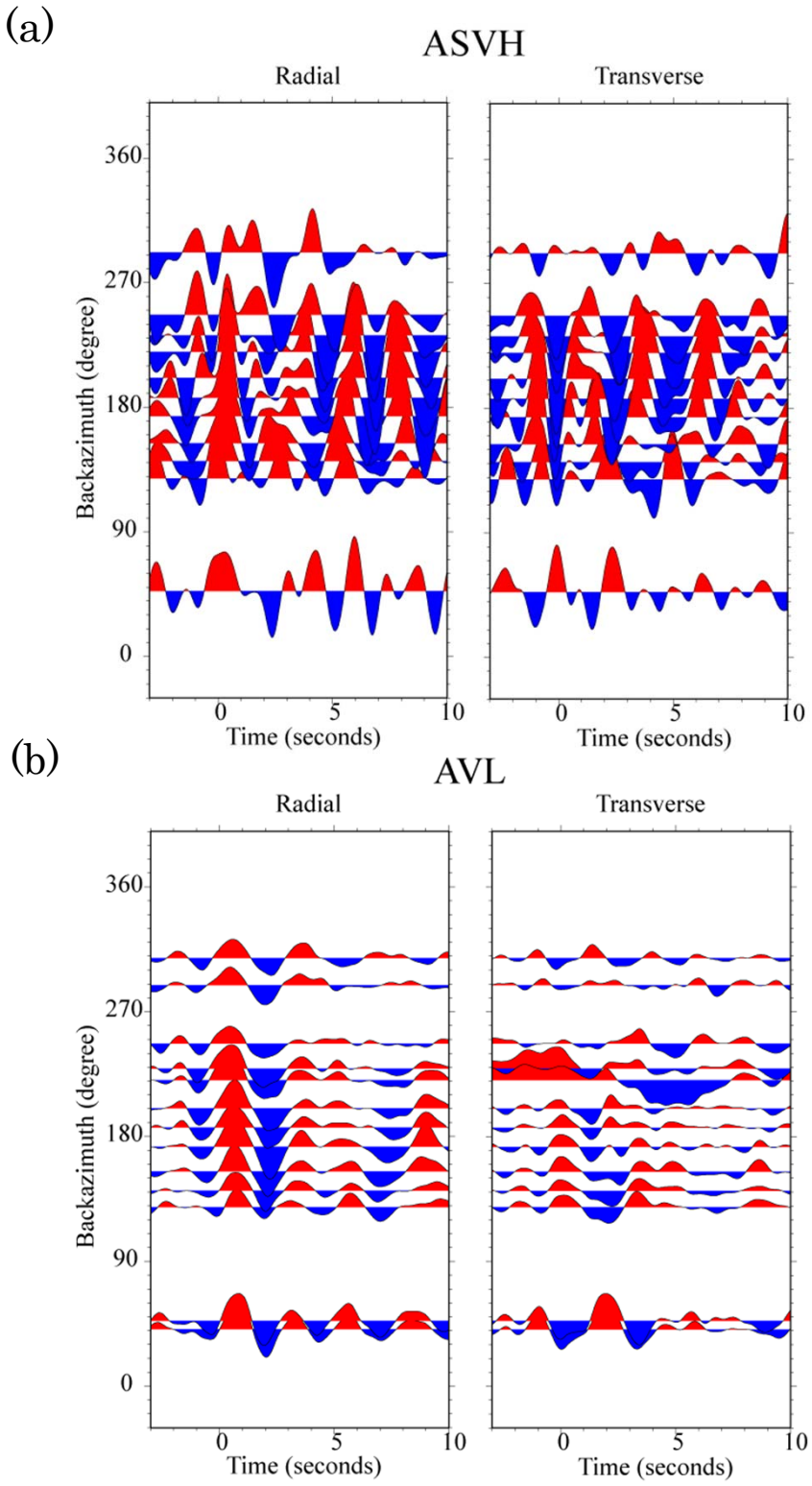

Figure 24 Radial and transverse RFs for groups of each station.

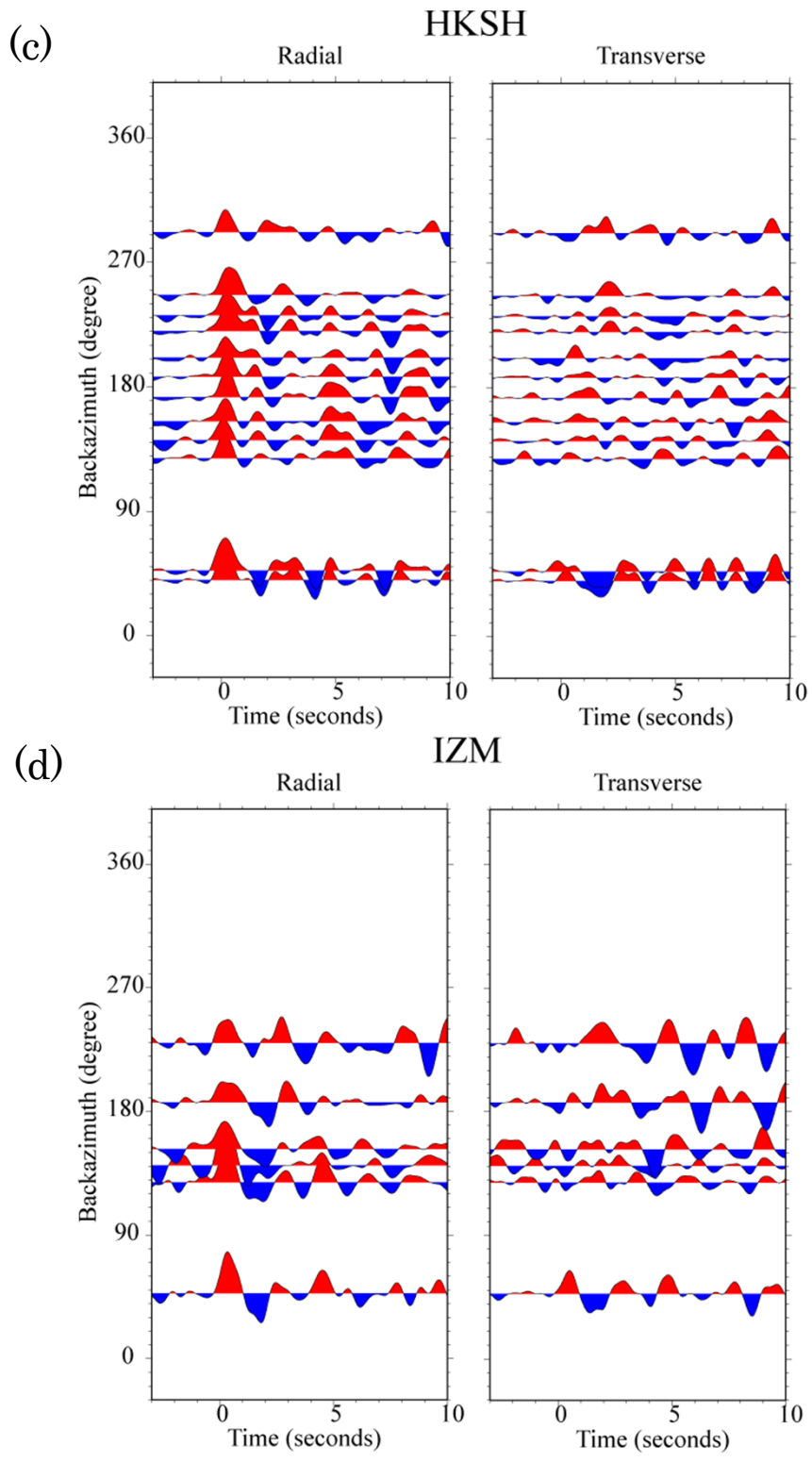

Figure 24 (Continued)

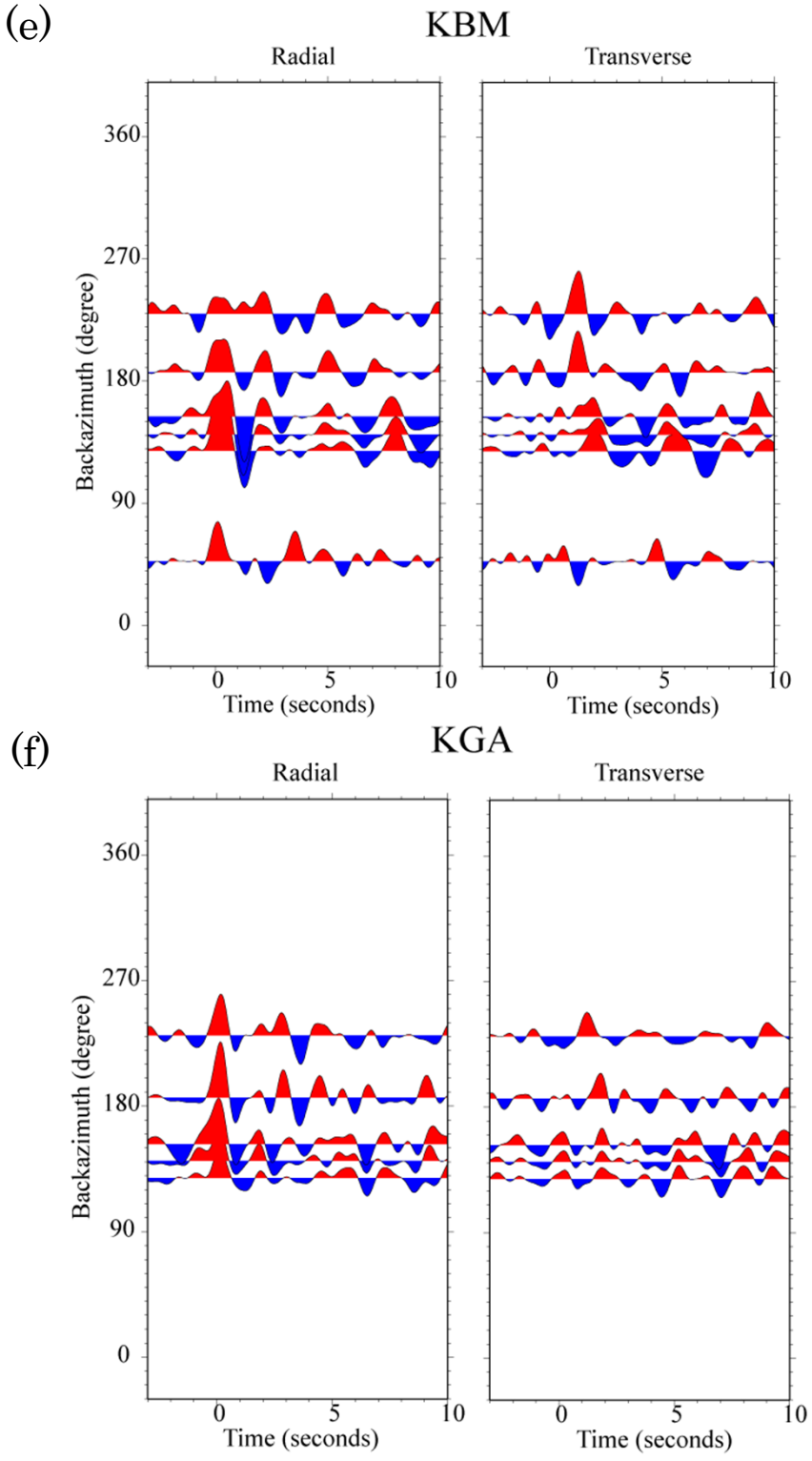

Figure 24 (Continued)

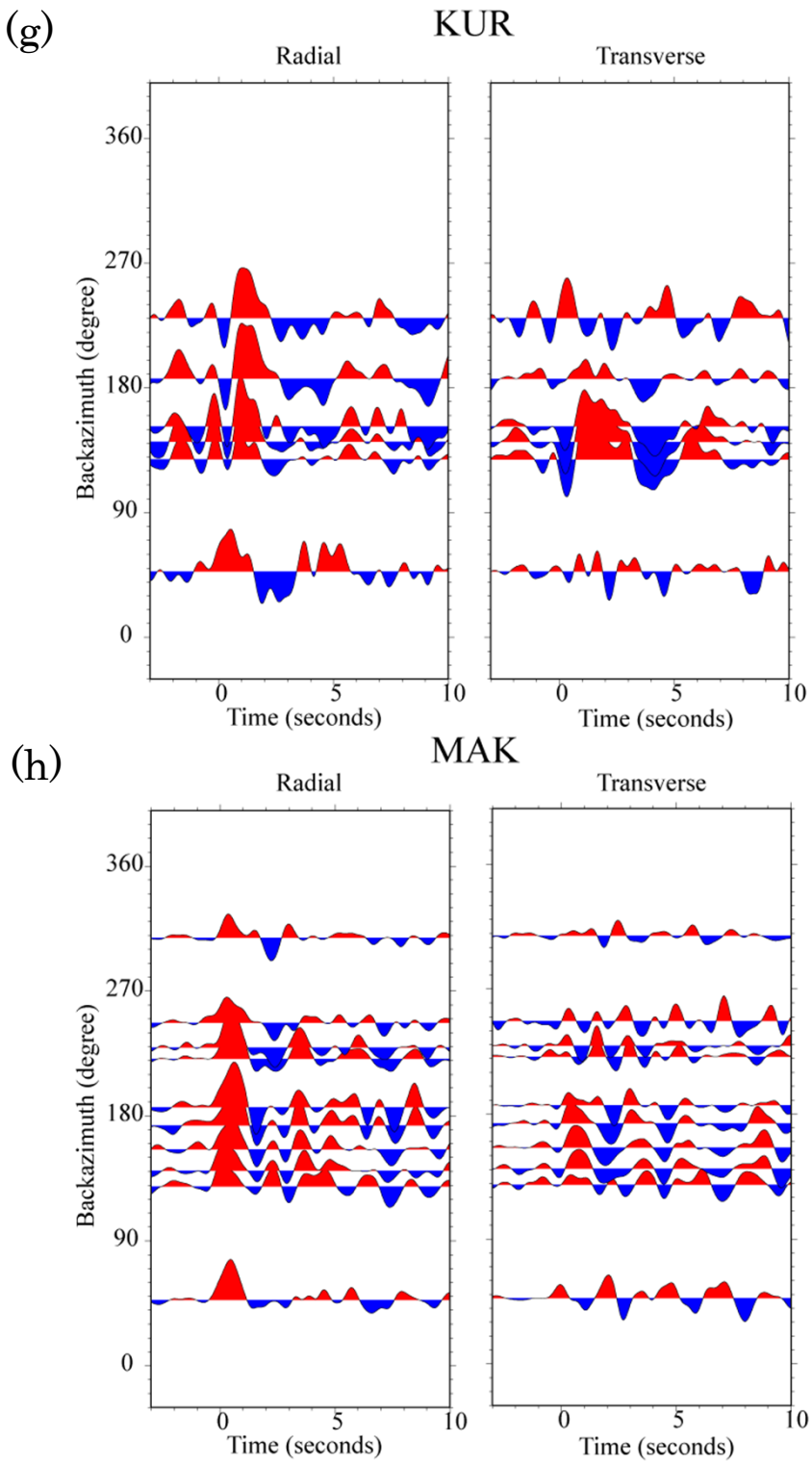

Figure 24 (Continued)

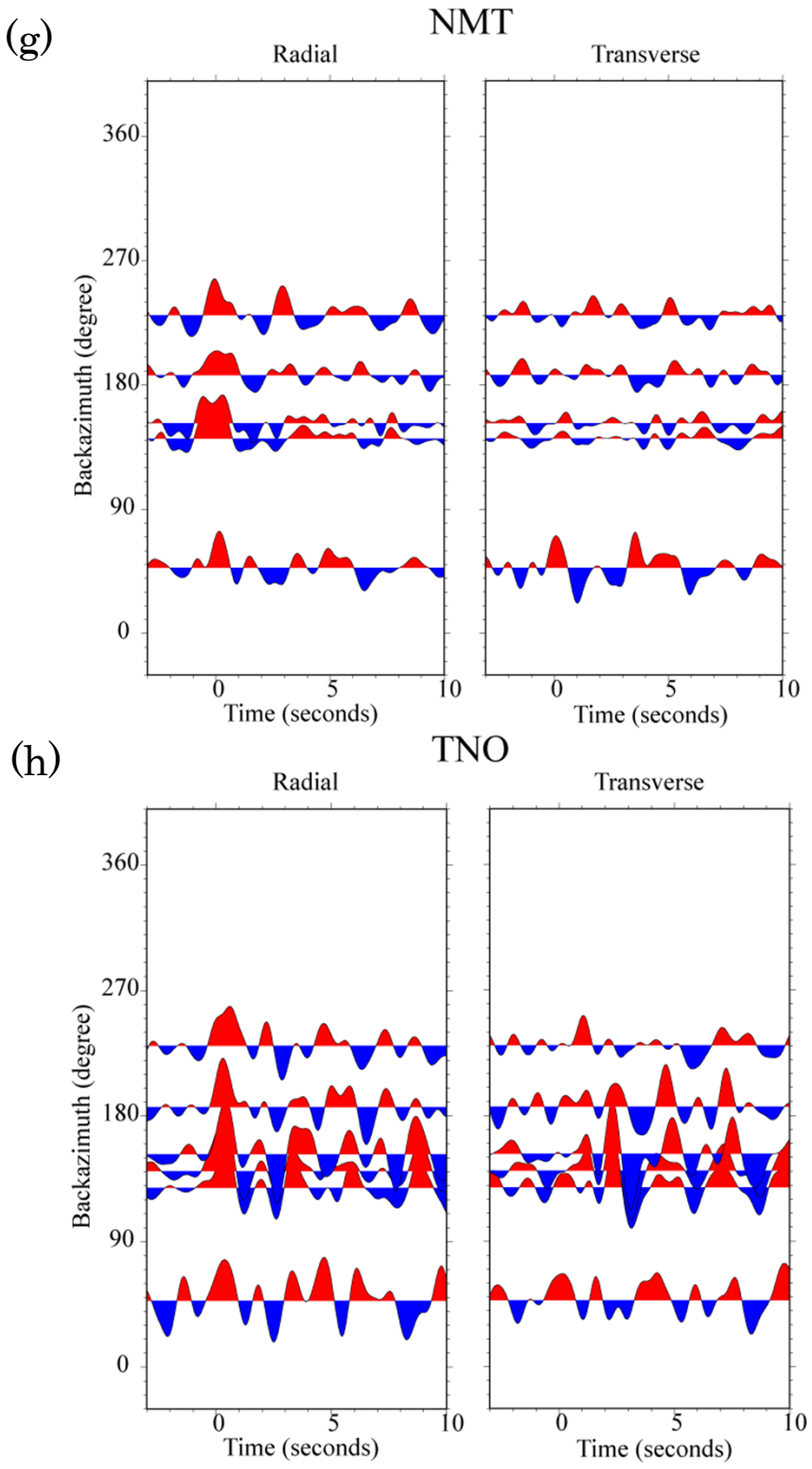

Figure 24 (Continued)

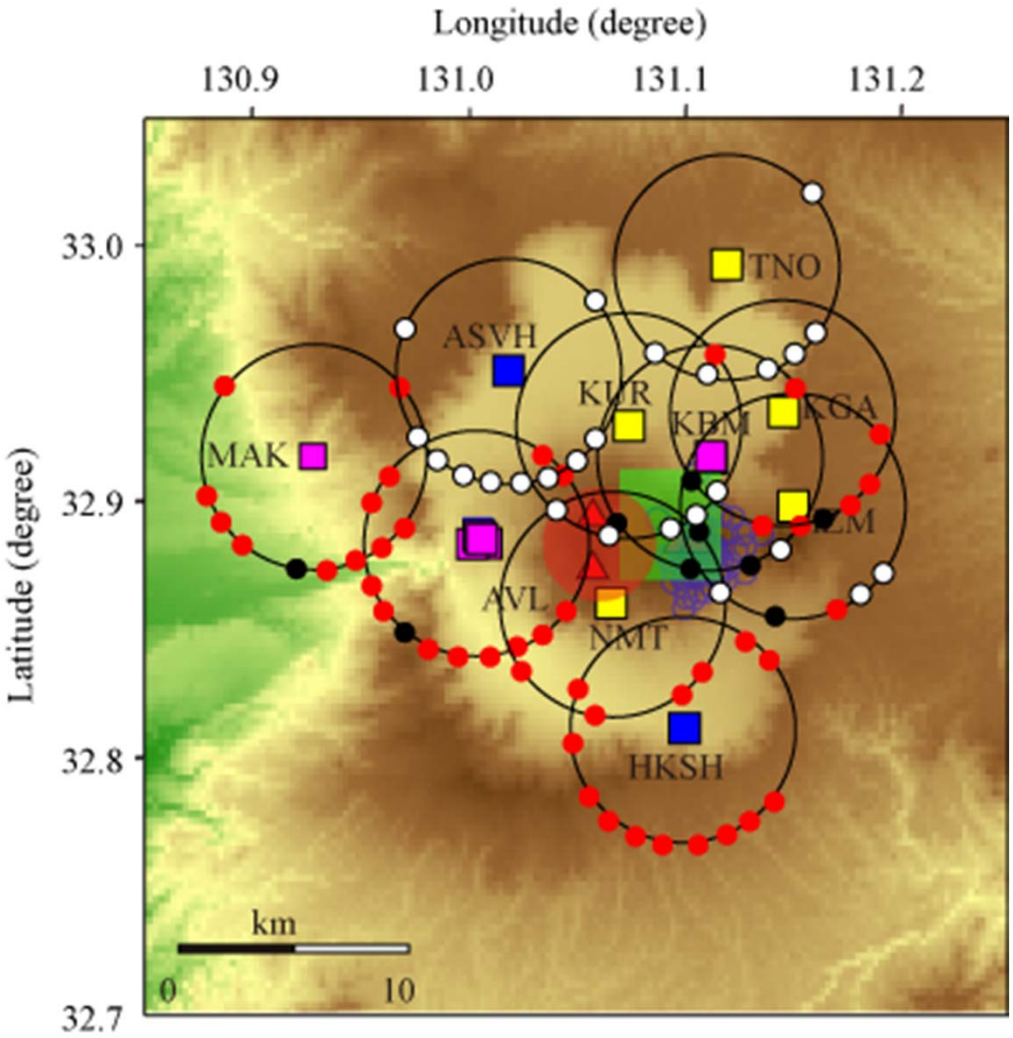

Figure 25　Groups in which more than 10 RFs are stacked. Blue, purple and yellow squares indicate the same as in Figure 21. Red triangles, large red circle, green square and blue small circles indicate summits of the central cones, magma chamber, sill-like deformation source and hypocenters of. We show the groups on a ring centered on each station with colored small circles. White small circles indicate groups in which averaged standard deviation of stacked RFs is over 0.1. Black circles indicate groups in which transverse RFs have a large amplitudes ($E(t) > 0.2$). Red circles indicate the other groups.

3.2 Inversion

We estimate subsurface structure beneath each station with genetic algorithm (GA) inversion of RFs [e.g. *Shibutani et al.,* 1996]. GA is one of the nonlinear global optimization methods that explore large model spaces [*Holland,* 1975; *Goldberg,* 1989]. We follow the inversion method of *Shibutani et al.* [1996]. We generate 200 generations, each of which has 1000 models. 3 component synthetic waveforms are calculated assuming each model with generalized ray theory [*Helmberger,* 1974], and a synthetic RF is estimated with the extended-time multitaper method [*Shibutani et al.,* 2008]. The misfit (objective function) is defined by the square sum of difference between the first 7s portion of a RF estimated from a model in a model space and that of an observed one. GA minimizes the misfit to optimize the models.

In Table 5, we show the model space. We set the model space by reference to the model space set by *Abe* [2009] which was based on the seismic refraction survey [*Research group for explosion seismology,* 1999a, b]. Some of the best fit RFs generated from the previous model space [*Abe,* 2009] have the first 1 s portion which does not fit the observed one. In this study, we add one surface layer and spread the ranges of S-wave velocities of the surface layers so that synthetic RFs have the first 1 s portion which is similar to the observed one. We set V_P/V_S by reference to the ak135 model [*Kennett et al.,* 1995], except for layers 1, 2, 3 and 5. Density(ρ) of each layer is determined by $\rho(\mathrm{g/cm^3}) = 2.35 + 0.036 \times (V_P(\mathrm{km/s}) - 3.0)^2$ [*Kurita,* 1973]. We assume S-wave velocity of near surface portion shallower than a few kilometers increases downward, and set 100.0 as the misfit values of the models which have the second or the third layer whose S-wave velocity is lower than that of the shallower

	thickness (km)			Vs (km/s)			Vp/Vs		
layer	Min.	Max.	n	Min.	Max.	n	Max.	Min.	n
1	0.5	2	2	0.5	3.6	5	1.6	2.3	3
2	0.5	2	2	0.5	3.6	5	1.6	2.3	3
3	1	4	2	2.3	3.8	4	1.6	2.3	3
4	1	16	4	3.1	3.8	3	1.68	1.68	0
5	0.5	8	4	0.8	3.9	5	1.6	2.3	3
6	1	16	4	3.2	3.9	3	1.68	1.68	0
7	1	16	4	3.5	4.2	3	1.69	1.69	0
8	half space			4.1	4.8	3	1.79	1.79	0

Table 5　Model space for GA inversion.

layers. In some of previous studies [*Nakamura et al.,* 2002; *Oda and Ushio,* 2007; *Abe*, 2009], the Moho beneath the Aso caldera was estimated to exist at depths between 30-40 km. Therefore, we assume the depth of the Moho (the upper surface of the deepest layer) is 30-40 km, and also set 100.0 as the misfit of the models which have the Moho shallower than 30 km or deeper than 40 km.

4. Results

RFs constructed from data at stations AVL, HKSH and MAK have wider backazimuthal coverage than those at stations IZM, KBM, KGA, KUR, and NMT. This is caused by the difference of the observation period, (AVL, HKSH, MAK: about 10 years; IZM, KBM, KGA, KUR, NMT: about 2-3 years). Therefore, if we continue observation, backazimuthal coverages of the above five stations will become wider. In Figure 25, RFs constructed from teleseismic waves which pass beneath the southern part of Aso caldera have low averaged standard deviation and low amplitude transverse component. In Figure 25, RFs constructed from teleseismic waves which pass beneath the eastern flank of the central cones have large amplitude transverse component.

We show the inversion results in Figure 26. Each RF has been inverted 3 times with a different set of initial models. We regard the best 5000 models in each inversion as acceptable models, and average them. The 3 averaged models for each group are shown in Figure 26. For the each averaged model, we calculated the misfit and the acceptable models which generate the smallest misfit are also shown in Figure 26. RFs synthesized from the 3 averaged models are shown on the observed RF together with RFs

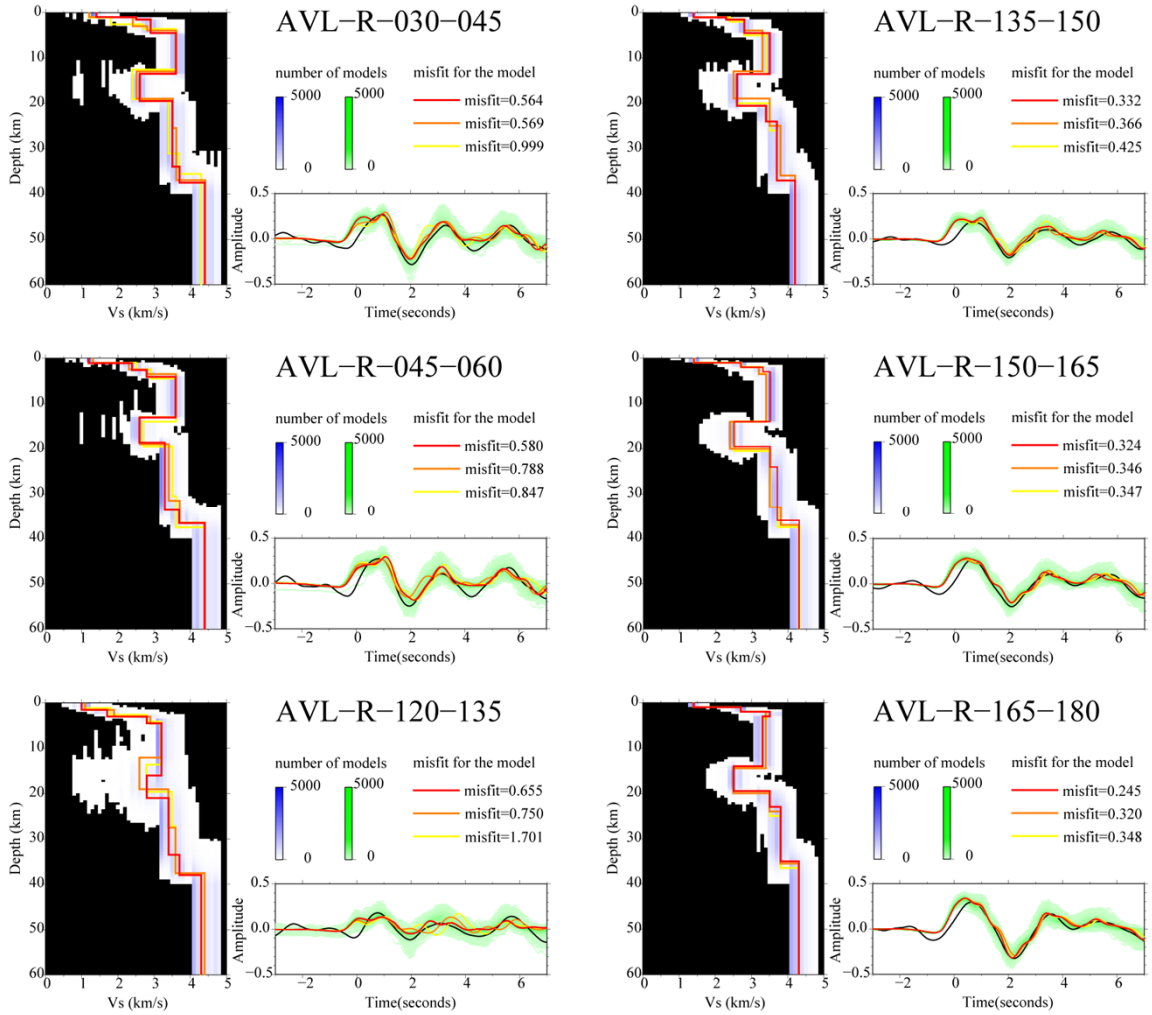

Figure 26 Results of inversion. Each set has two panels and the name of the group is indicated on the right top. The white and blue areas on the left panel indicate the best 5000 models generated from the best inversion. The green areas on the right below panel indicate RFs synthesized from the best 5000 models generated from the best inversion. Red, orange and yellow lines indicate the averaged models of the best 5000 models generated from three inversions on the left panel, and RFs synthesized from the averaged models on the right below panel. Misfit values for the best fit models generated from the three inversions are shown on the upper right.

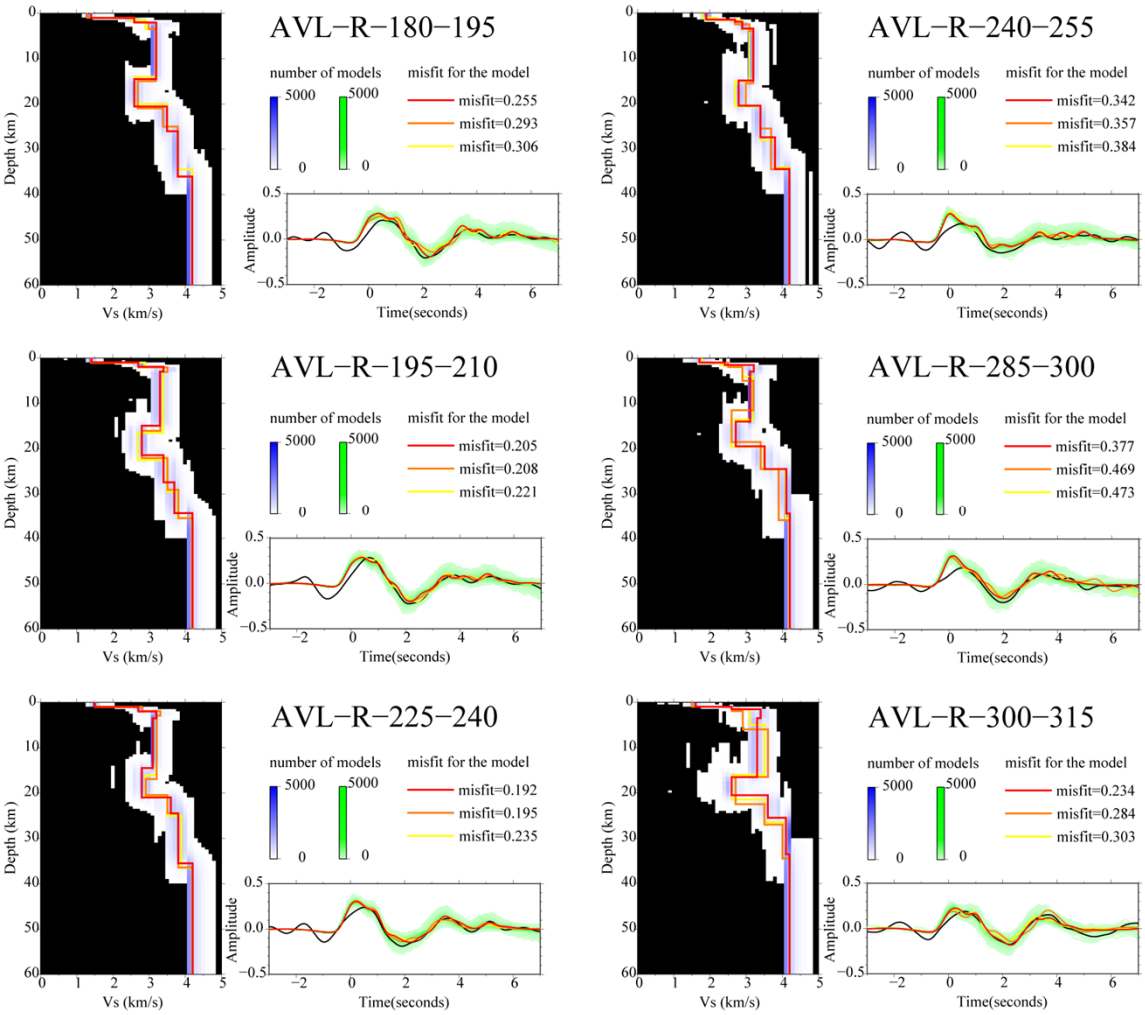

Figure 26 （Continued）

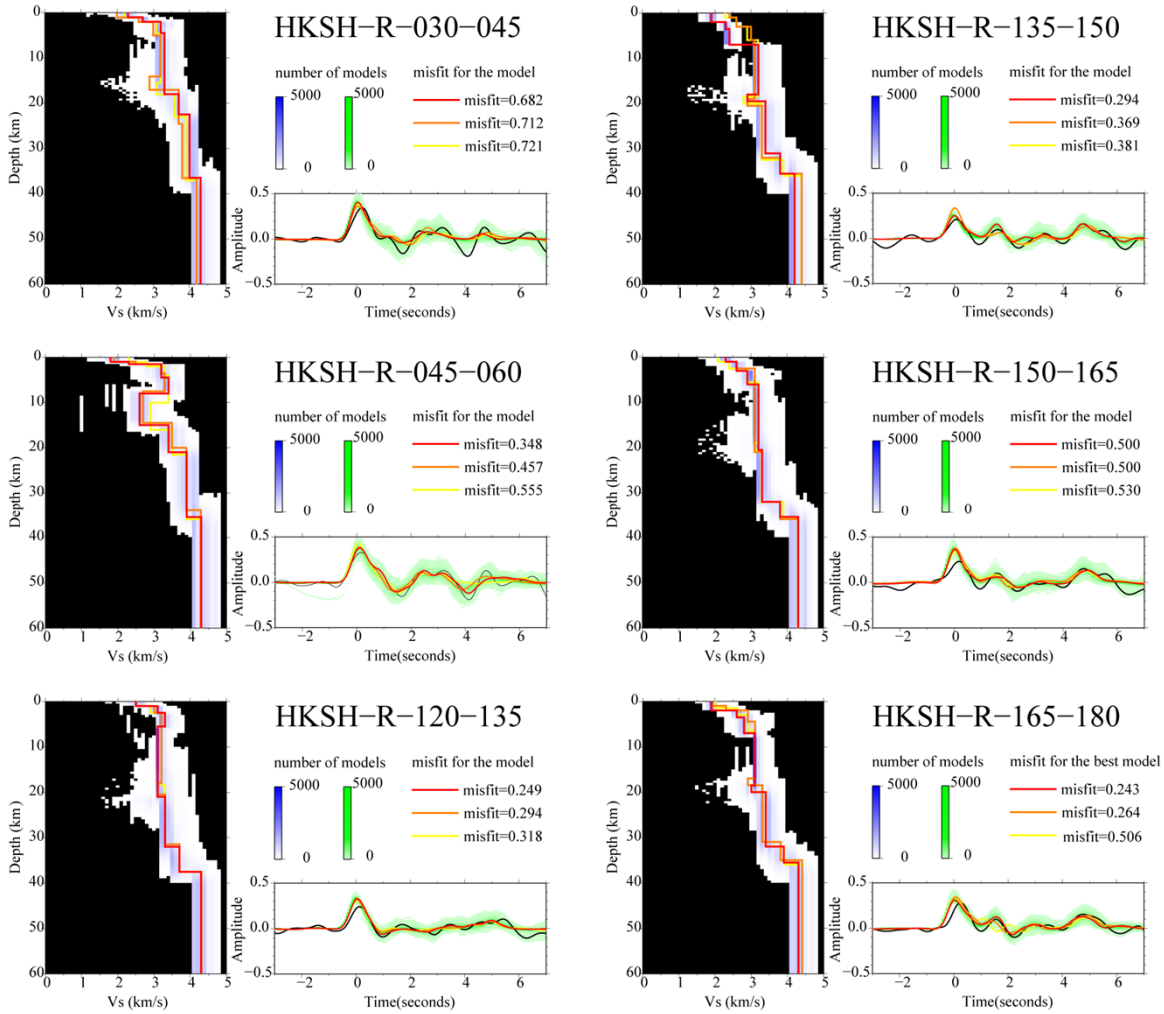

Figure 26 （Continued）

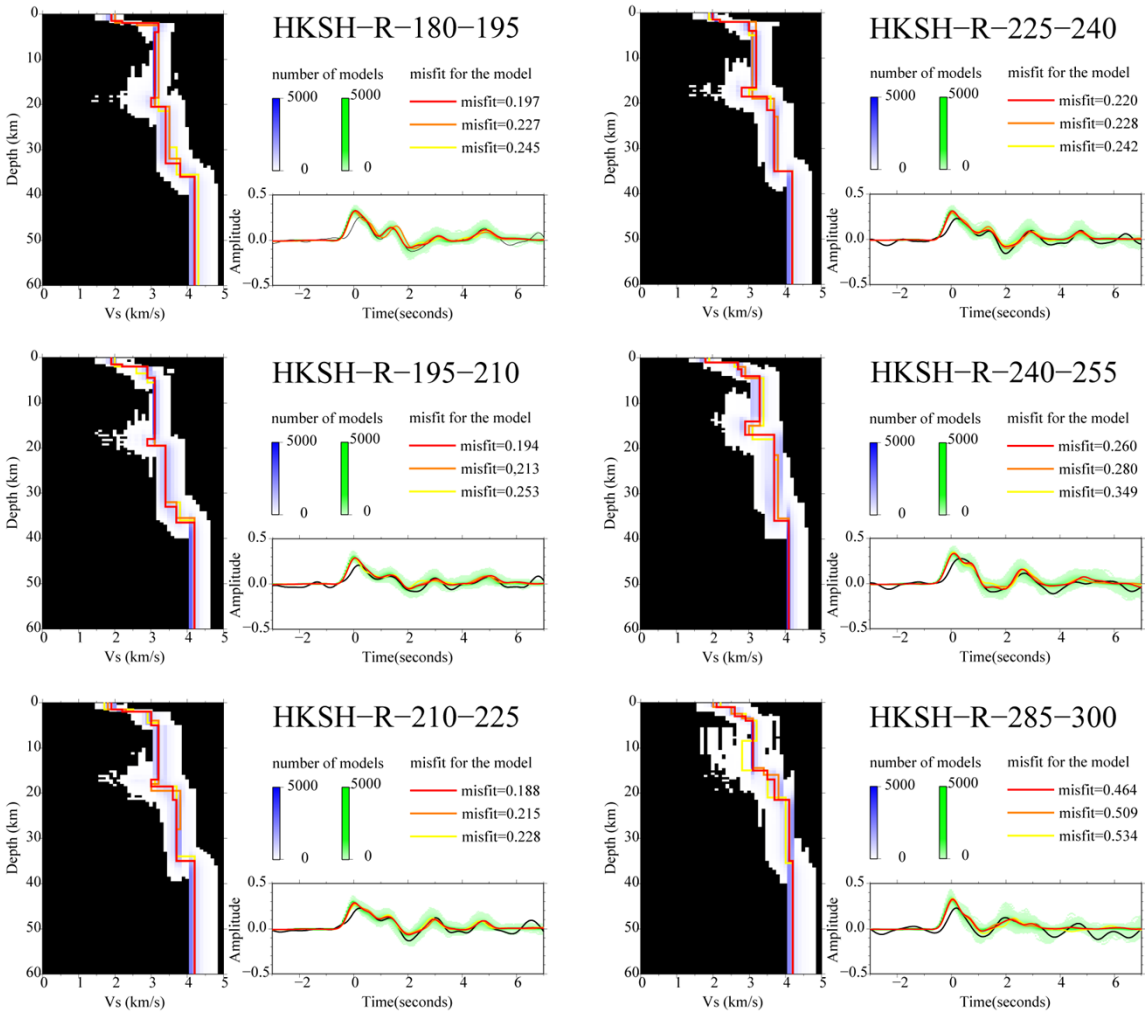

Figure 26 （Continued）

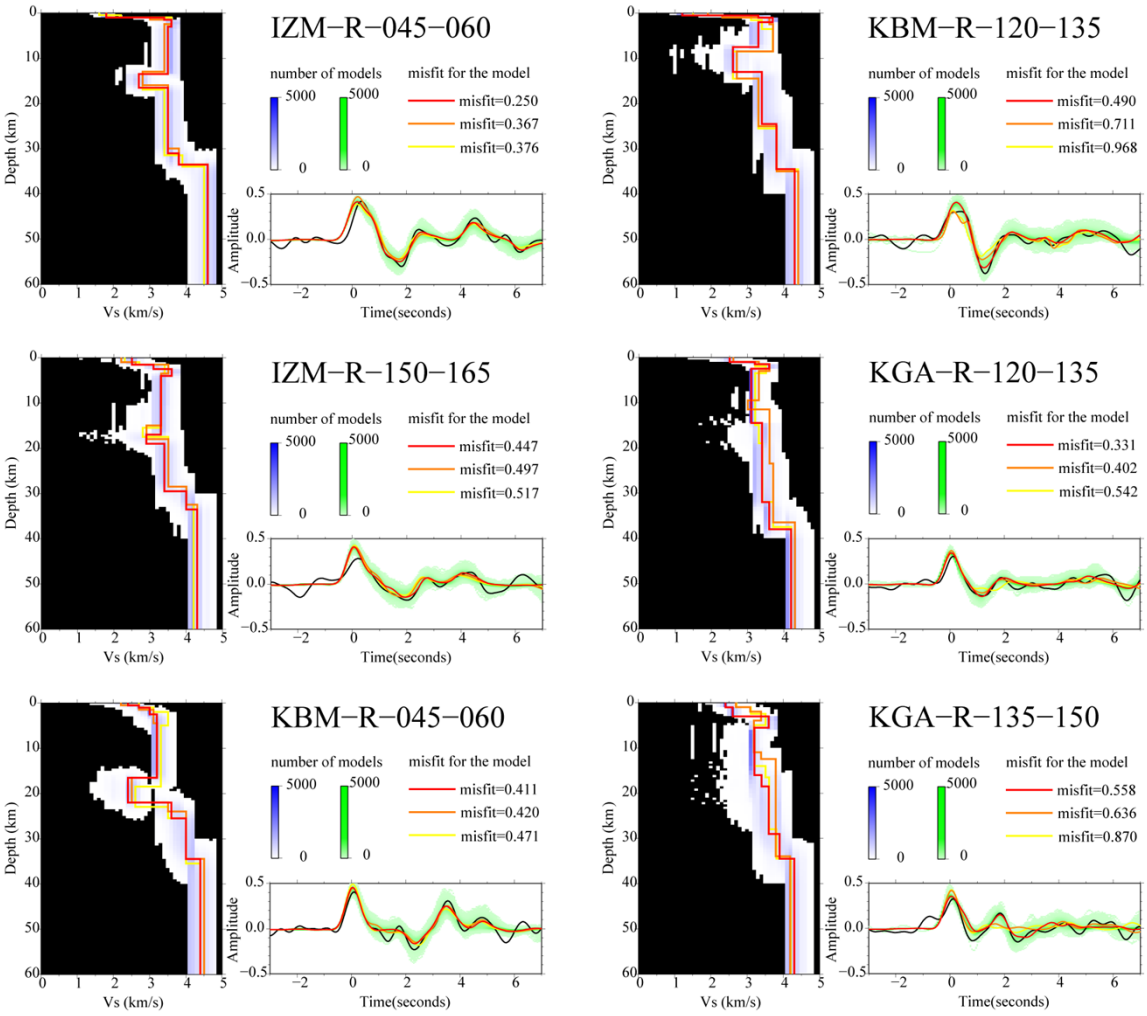

Figure 26 （Continued）

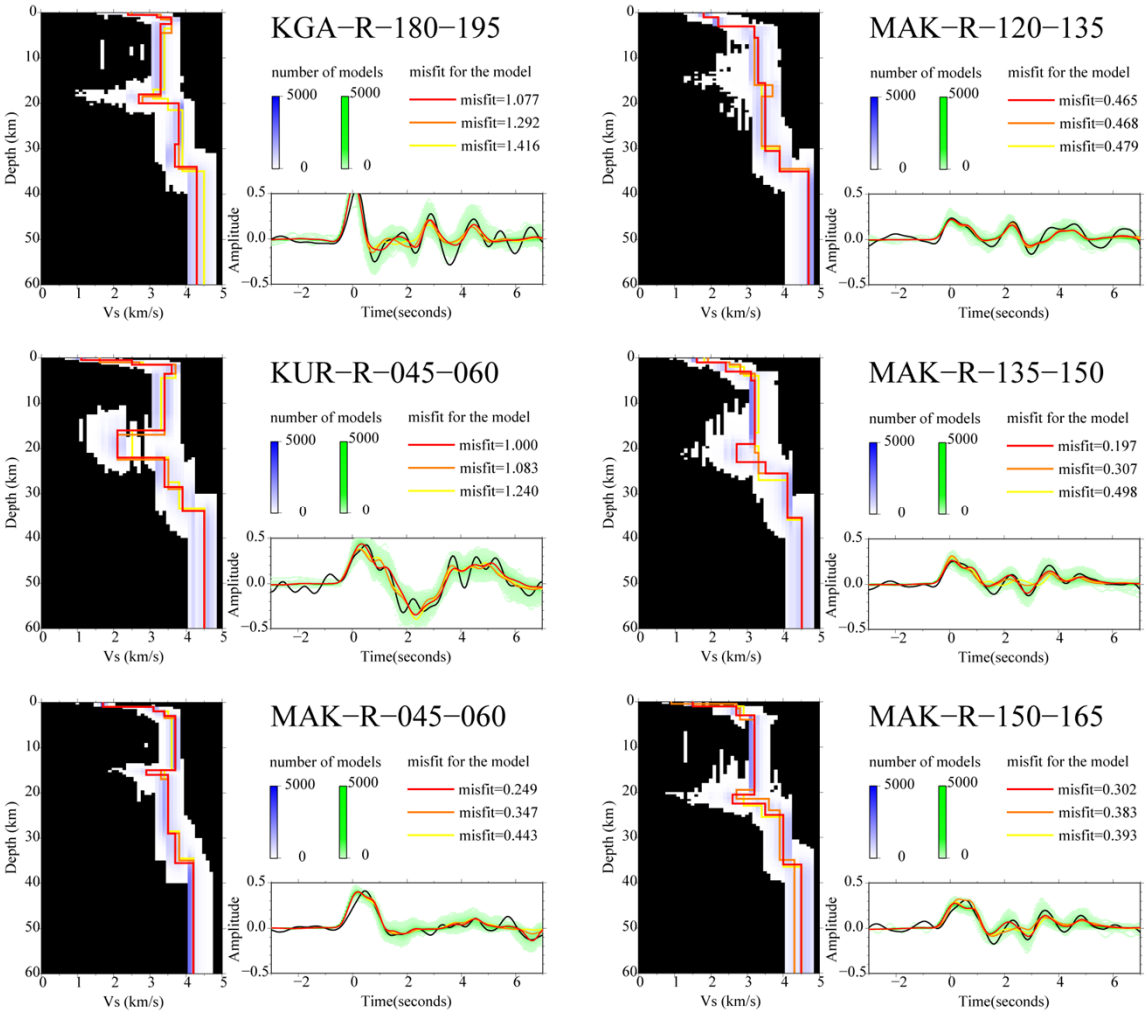

Figure 26 （Continued）

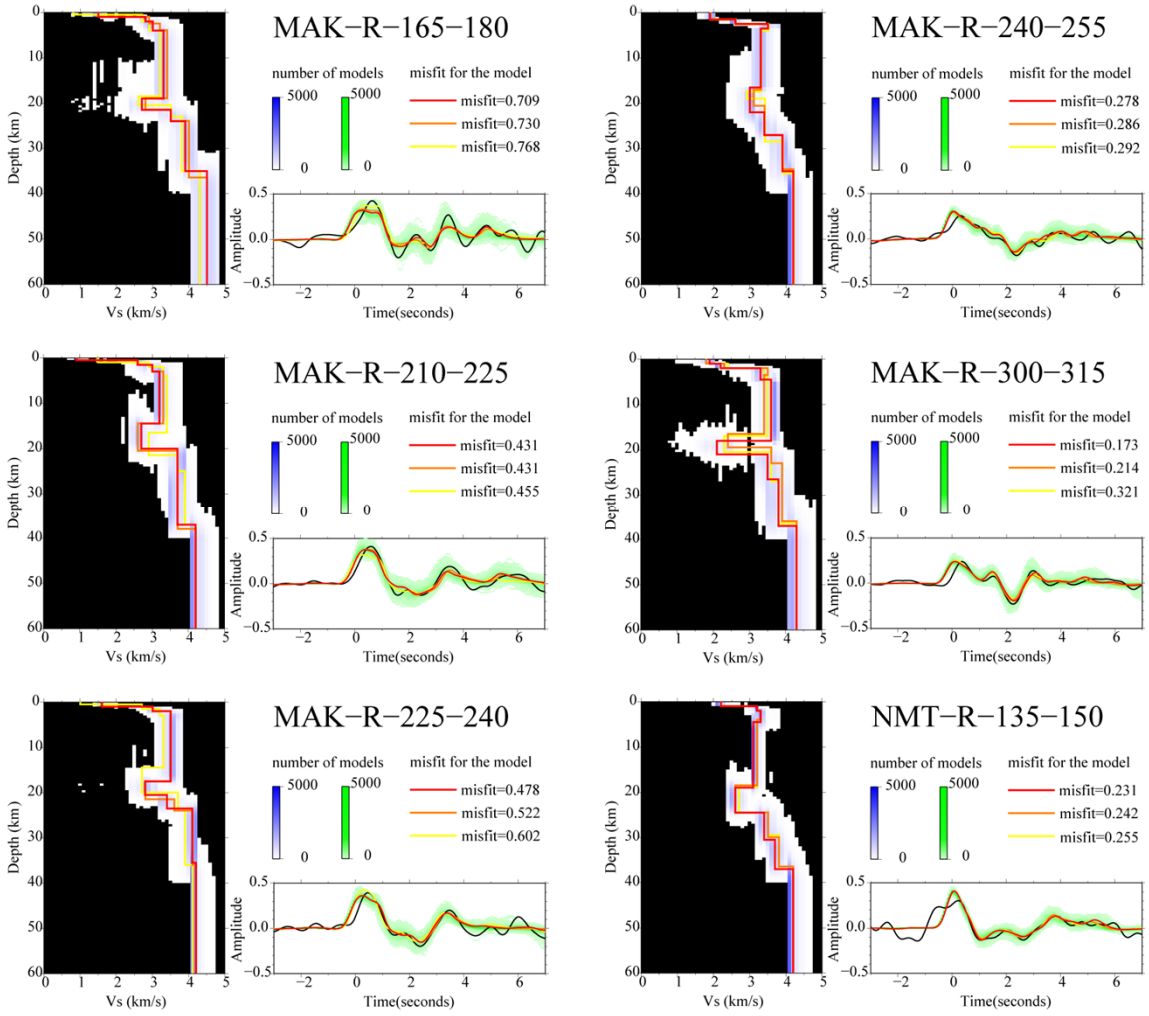

Figure 26 （Continued）

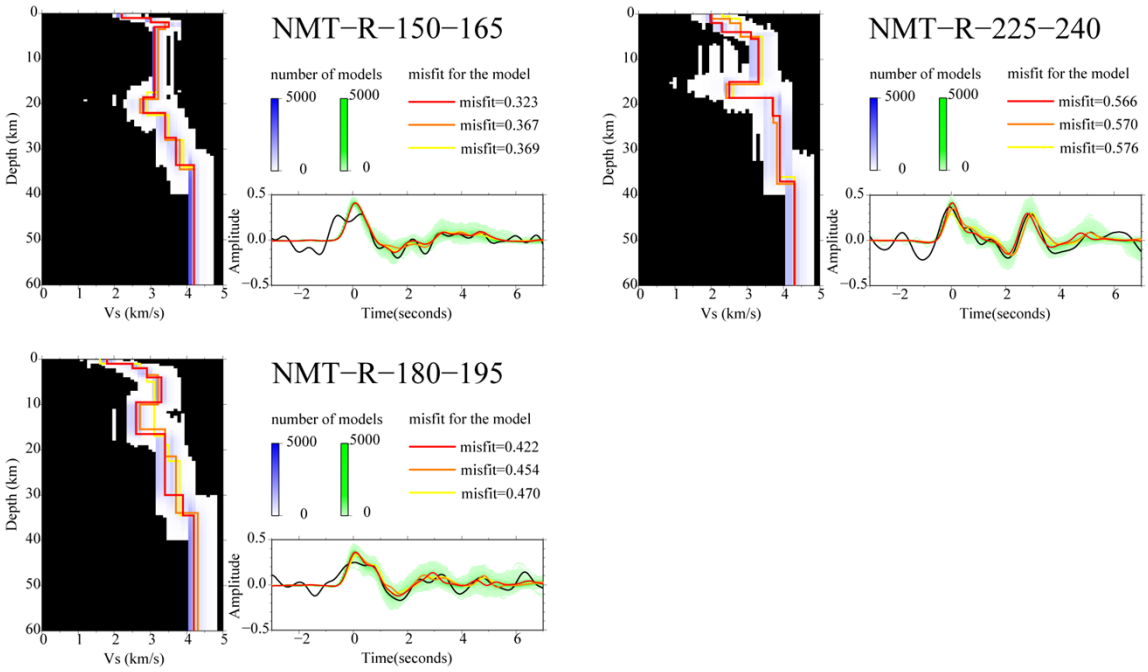

Figure 26 （Continued）

synthesized from the above mentioned acceptable models. We describe the averaged model which has lowest misfit value of the three as the best inversion model. In Figure 26, 3 averaged velocity models for each RF are about the same, and this fact implies that the velocity structure estimated in this study is little dependent on the initial models.

We define the detected the low velocity layer whose depth range is 10-24 km and whose S-wave velocity range is 2.0-2.6 km/s as LVL. The best inversion models for groups AVL-030-045, AVL-135-150, AVL-150-165, AVL-165-180, AVL-180-195, AVL-285-300, AVL-300-315, KBM-045-060, KUR-045-060, NMT-225-240 have LVL. Although the best inversion model for MAK-300-315 can be interpreted to have LVL, the low velocity layer included in the model would be separated from LVL beneath Aso caldera, and we do not interpret the low velocity layer as LVL. In this study, we have also detected LVL beneath wider area in Aso caldera than *Abe* [2009]. We estimate the characteristics of LVL with averaging parameters of the 10 models which have LVL. The averaged depths of the upper and lower boundaries of LVL are 15 km and 20 km, respectively, and the thickness of LVL is 5 km. Averaged S-wave velocities of the above and below layers are 3.35 km/s and 3.55 km/s, respectively, and averaged S-wave velocity of LVL is 2.5 km/s Therefore, S-wave velocity reduction of LVL from surrounding portion is 27%. Averaged V_P/V_S of LVL is estimated to be 2.0, and P-wave velocity reduction of LVL is 13%.

In Figure 27, the S-wave velocity structures detected from the best inversion models of all the groups are shown. We calculate Ps conversion points with iasp91. At each depth, detected S-wave velocity is plotted on the area where the distance from a conversion point is shorter than one fourth of the radius of the Fresnel zone defined as

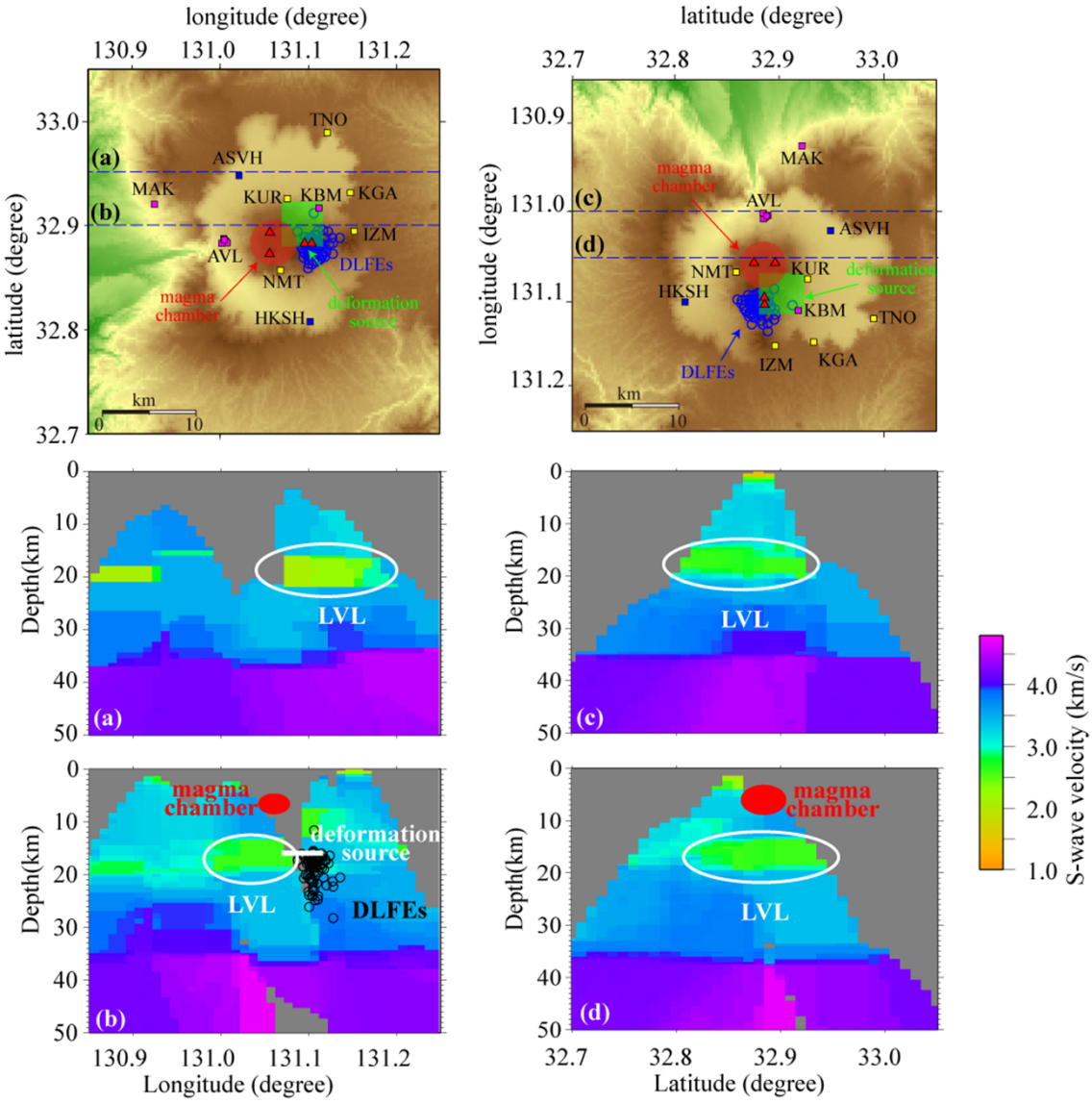

Figure 27 Maps of Aso caldera and vertical sections showing detected S-wave velocity structure. Each map is the same as that in Figure 21. The map on the right side is rotated clockwise 90º with respect to the map on the left side. Each section is along each dashed blue line on the map, and shows S-wave velocity structure by the color bar. S-wave velocity is not detected in grey areas. Red ellipsoids, small black circles and white lines indicate magma chamber, DLFEs and sill-like deformation source. LVL is encircled by white lines.

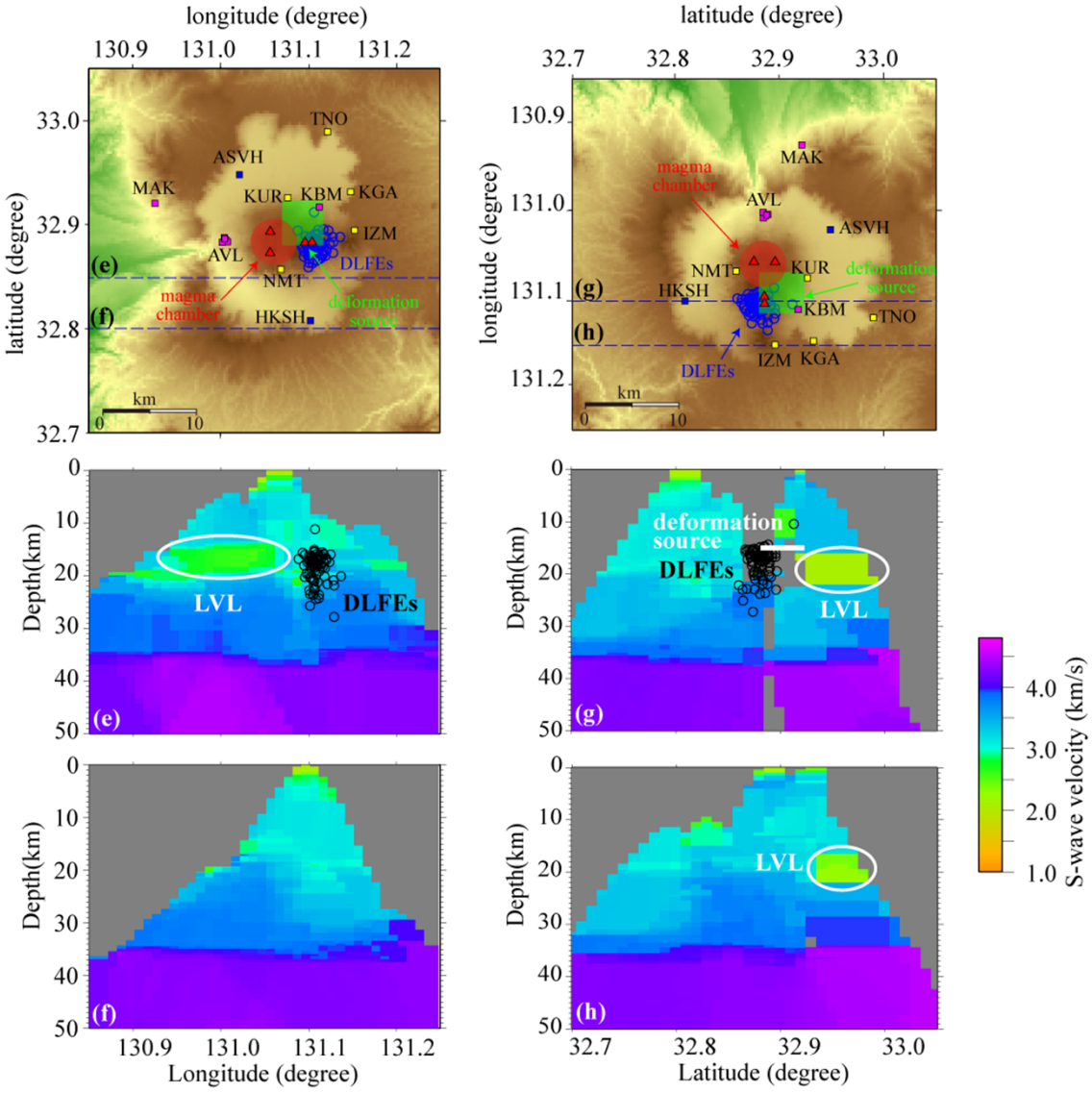

Figure 27 (Continued)

$r(d) = \sqrt{(d + \frac{V_P(d)}{1.12})^2 - d^2}$, where d indicates depth (km), *Vp(d)* indicates P-wave velocity of iasp91 at a depth of d km. 1.12 is double of corner frequency (Hz) of RFs. We use a grid for the velocity field spacing of 0.01° in the horizontal direction and 1 km in depth. When S-wave velocity of a node is defined by two or more models, S-wave velocities are averaged, using inverses of distances from the calculated conversion points as weights.

5. Discussion

Stacked RFs for stations ASVH and TNO whose averaged standard deviations are smaller than 0.1 have not been obtained. The two stations exist at the northern part of Aso caldera, and the crustal structure beneath the northern part might have a heterogeneous structure.

RFs constructed from teleseismic waves which pass beneath the eastern flank of the central cones have large amplitude of transverse component (Figure 25), and structure beneath the eastern flank should not be estimated assuming horizontally layered isotropic structure. The effects on these RFs are large at about 1 s. Shear waves converted at a depth of about 10 km would arrive at 1 s after the arrival of direct P-wave. Therefore, anomalous portion may exist at a depth of 10 km beneath the eastern flank of the central cones. We show radial and transverse RFs which are constructed from teleseismic P-waves passing beneath the eastern flank of the central cones in Figure 28. Transverse RFs whose teleseismic events occurred northeast (KBM-045-060, NMT-045-060) have large negative peaks at about 1 s. Transverse RFs whose

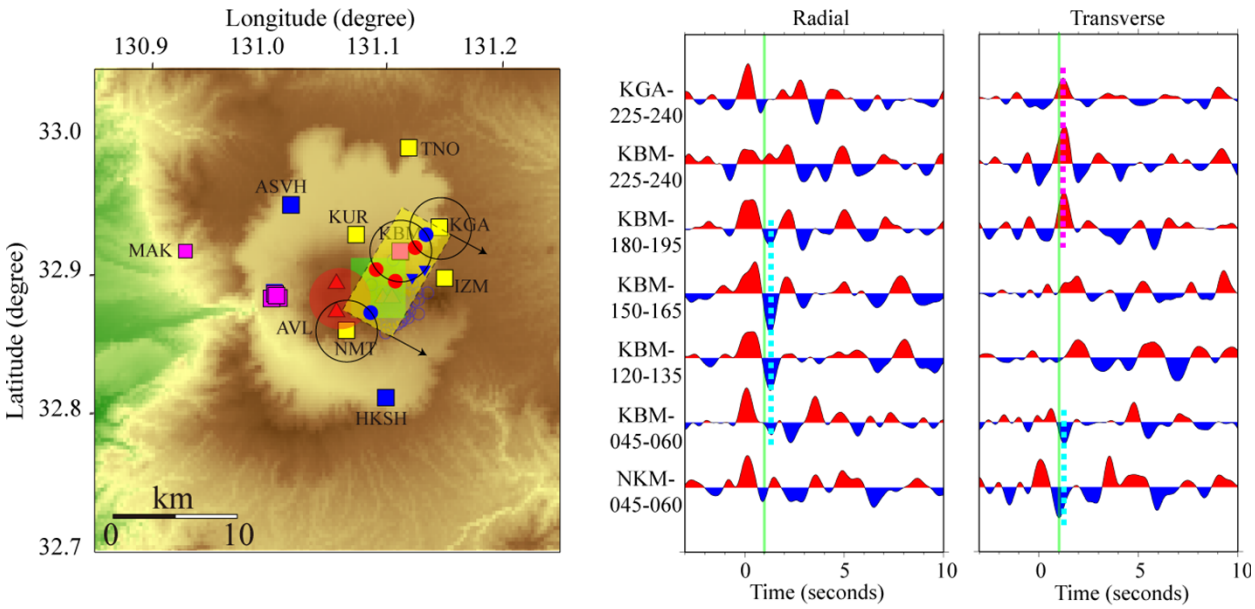

Figure 28 Left map: We show the groups on a ring centered on each station with colored small circles. Red small circles indicate groups whose transverse RFs have large positive amplitudes, blue small circles indicate groups whose transverse RFs have large negative amplitudes, and blue small triangles indicate groups whose radial RFs have large positive amplitudes at about 1 s. A dipping interface is expected to exist beneath the yellow square at a depth of about 10 km. The other symbols indicate the same as in Figure 25. Right panels: RFs which are constructed from teleseismic P-wave passing beneath the eastern flank of the central cones.

teleseismic events occurred southwest (KGA-225-240, KBM-225-240, KBM-180-195) have large negative peaks at about 1 s. Radial RFs whose teleseismic events occurred southeast (KBM-150-165, KBM-120-135) have large negative peaks at about 1 s. These peaks indicate the existence of an interface dipping toward southeast, below which lower S-wave velocity medium exists, beneath the eastern flank of the central cones (Figure 28). Beneath this portion, a sill-like deformation source [*Geographical Survey Institute*, 2004; *Ohkura and Oikawa*, 2008] and a swarm of low frequency earthquakes are located at depths of 15.5 km and 15-25 km, respectively (Figure 25), and existence of fluid and its movement are expected. Fluid from the sill-like deformation source and the swarm of low frequency earthquakes might be transported through a dipping layer to the surface.

Abe [2009] obtained LVL beneath the western part of Aso caldera with RF inversion, and also revealed that LVL does not exist beneath the southern part of the caldera. Results of our new analyses agree with the previous studies. Additionally we have revealed that LVL exists beneath the northeastern part of the caldera, and does not exist beneath the eastern part.

It is expected from the fact that LVL has very low S-wave velocity, 2.5 km/s, that fluid is contained in LVL. We estimate the fluid fraction of LVL from the averaged parameters of the 10 models containing LVL with a method suggested by *Takei* [2002]. Although P-wave velocity reduction of LVL is also estimated, amplitude of RF peak has little dependence on P-wave velocity contrast and it would be difficult to estimate P-wave velocity contrast accurately from RF inversion. Therefore, we do not use the obtained P-wave velocity reduction for estimating the fluid fraction of LVL. The fluid

fraction (φ) is estimated as $\varphi = \frac{1-(\frac{V_S}{V_S^0})^2}{\Lambda_N-(1-\frac{\rho_f}{\rho})(\frac{V_S}{V_S^0})^2}$, where Λ_N indicates the coefficient which represents the relationship between liquid volume fraction and shear modulus of the medium, ρ indicates density of the skeleton, ρ_f indicates density of the fluid, V_S^0 indicates shear wave velocity of the solid phase and V_S indicates the solid-liquid system, respectively. Physical property of the contained liquid is not determined only from seismic velocity structure, and we estimate fluid fraction in the case the fluid is molten rocks and in the case the fluid is water. We do not obtain P-wave velocity structure, and the aspect ratio of pores is not determined. If very small aspect ratio is assumed, little fluid is necessary to decrease seismic velocity of the medium largely. Therefore, we assume the maximum aspect ratio of pores and estimate maximum fluid content of LVL. According to *Takei* [2002], maximum dihedral angles of partially molten rocks and rock + aqueous fluid system are 40º and 100º, corresponding to 0.15 and 0.5 of the equivalent aspect ratios, respectively. We assume these values are the maximum aspect ratios. According to *Takei* [2002], Λ_N of media with 0.15 and 0.5 of the equivalent aspect ratio (α) are 3.75 and 2.08, respectively. $\rho_f/\rho = 0.92, 0.33$ are assumed for melt and water, respectively. $V_S = 2.5$ (km/s) and $V_S^0 = 3.45$ (km/s) are assumed based on our inversion results. Using these values, φ are calculated to be 0.15 for molten rocks and to be 0.3 for aqueous fluid. The area of LVL obtained in this study is about 200 km^2. Therefore, the volume of LVL and maximum amounts of aqueous fluid and melt contained in LVL are simply calculated to be 1000 km^3, 300 km^3 and 150 km^3, respectively. These values will not largely increase if the crustal structure beneath the northwestern part of the caldera is revealed. However, some small low velocity regions which are not define as LVL exist in the study area would contain fluid.

Finally, we indicate that LVL might contain or generate silicic magma which will be ejected at the future large eruption (Aso5). The previous large eruption of Aso (Aso4) ejected a large amount of silicic magma [*Kaneko et al.* 2007], and the other large scale calderas (e.g. Crater Lake, Long Valley, Taupo, Yellowstone) are also estimated to be formed by large eruptions of silicic magma [*Petford et al.,* 2000; *Kaneko et al.* 2008]. Such a silicic magma is thought to be generated from the continental crust partially melted by mafic intrusion from the mantle [e.g. *Petford et al.,* 2000; *Kaneko et al.,* 2008]. From S-wave velocity structure, LVL is possible to be a partially molten crust. Although we do not obtain the structure which is interpreted as a path of mafic magma to the bottom of LVL, it might exist near the swarm of the deep low frequency earthquakes which are interpreted to be caused by fluid movement [*Ukawa and Ohtake*, 1987; *Nakamichi et al.,* 2003]. Partially molten crust is expected to keep fluid for several tens of thousands of years because partially molten crust whose melt fraction is less than 0.3-0.5 would not have fluidity and would be conductively cooled at a very low rate [*Kaneko et al.,* 2006]. Even if a path of mafic melt has disappeared now, therefore, partially molten region is possible to remain in the crust. We estimate from detected S-wave velocity structure that LVL can contain 150 km^3 of molten rocks at a maximum. This amount is comparable to the dense rock equivalent volume of pre-eruptive magma (>200km^3) estimated by *Kaneko et al.* [2007].

We add the crustal structure obtained from this study to the previously revealed information, and show schematic interpretation of the crustal structure beneath Aso caldera in Figure 29.

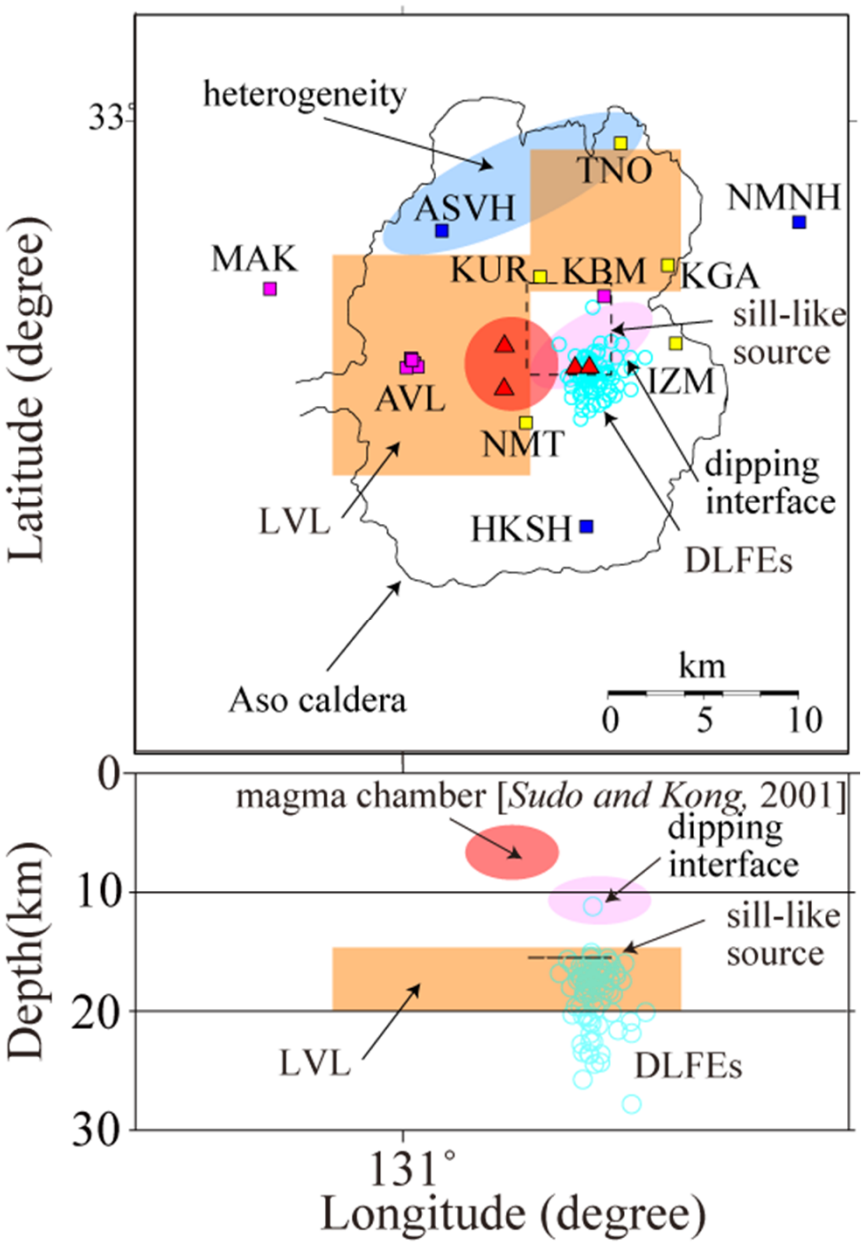

Figure 29 Schematic interpretation of the crustal structure beneath Aso caldera. Upper, map of Aso caldera. Lower, east-west vertical section. Purple ellipses indicate the dipping interface at a depth of about 10 km. The other symbols indicate the same as in Figure 21.

6. Conclusions

The crustal structure beneath Aso caldera has been estimated. The crust beneath northern part of Aso caldera might have a heterogeneous structure. The crust would have a low velocity portion whose upper boundary is dipping toward southeast beneath the eastern flank of the central cones and above the sill-like deformation source and the swarm of low frequency earthquakes. A very low S-wave velocity (2.5 km/s) layer is obtained at depths of 15-20 km beneath the western part and the northeastern part, and estimated to contain 30% of aqueous fluid or 15% of molten rocks at a maximum. The low velocity layer might generate or contain magma which will erupt at the next huge eruption cycle in the future.

IV. General Discussion

1. New insights into volcanism in Kyushu

The purpose of studies in this thesis is to contribute to revealing where and how magma is generated, conveyed and accumulated in Kyushu. Therefore, we execute receiver function analyses in Kyushu, and detect discontinuities in the uppermost mantle beneath Kyushu island and crustal seismic velocity structure beneath Aso caldera. We have detected seismic velocity discontinuities with a higher resolution than that with seismic tomography which has been applied in Kyushu in several previous studies [e.g. *Zhao et al.,* 2000; *Sudo and Kong,* 2001; *Honda and Nakanishi,* 2003; *Wang and Zhao,* 2006; *Nakajima and Hasegawa,* 2007; *Xia et al.,* 2008; *Hirose et al.,* 2008; *Tahara et al.,* 2008; *Saiga et al,.* 2010].

In chapter II, we have revealed water transportation through the oceanic crust of the PHS slab. The oceanic crust of the PHS slab is interpreted to be hydrated down to 70-90 km in depth beneath Kyushu. *Hirose et al.* [2008] estimated 3-d velocity structure beneath SW Japan with double-difference tomography. *Okamoto et al.* [2008] analyzed later-phases of the intermediate-depth earthquakes and detected existence of low velocity layer corresponding to the hydrated oceanic crust. They estimated that the oceanic crust of the PHS slab has lower velocity than surrounding portion down to about 60 km in depth. Therefore, we have revealed that the oceanic crust of the PHS slab would bring water deeper than the previous studies estimated.

We have also revealed that S-wave velocity of the mantle wedge beneath the forearc region decreases down to 2.8 km/s. Such a low velocity portion has not been

detected with seismic tomography [e.g. *Zhao et al.,* 2000; *Honda and Nakanishi,* 2003; *Wang and Zhao,* 2006; *Nakajima and Hasegawa,* 2007; *Xia et al.,* 2008; *Hirose et al.,* 2008; *Tahara et al.,* 2008]. RF analyses are able to detect a small size velocity anomaly with large perturbation which cannot be detected with seismic tomography. From our estimation of S-wave velocity, the forearc mantle beneath Kyushu is expected to be highly serpentinized and/or contains free fluids which have high pore pressure.

In chapter III, we have revealed that a low S-wave velocity layer with a large volume of about 1000 km^3 exists beneath Aso caldera at depths of 15-20 km. It is possible that the low velocity layer contains 150 km^3 of molten rocks at a maximum, which is about the same as dense rock equivalent volume of erupted magma (200 km^3 estimated by *Kaneko et al.* [2007]) at the latest large eruption of Aso. Magma which ejects at a caldera-forming eruption has been expected to be generated when mafic intrusion melts the continental crust [*Petford et al.,* 2000; *Kaneko et al.,* 2008].

As stated at the first paragraph in this chapter, the purpose of studies in this thesis is to contribute to revealing the processes of volcanic activity, where and how magma is generated, conveyed and accumulated in Kyushu. We have revealed where the hydrated oceanic crust of the PHS slab exists and where serpentinized mantle exists. Hydrous portion of the oceanic crust and serpentinized portion of the forearc mantle are important for understanding water transportation through the subducting slab. Water transportation through a subducting slab is important for understanding the volcanic activity in a subduction zone, because water supplied by a subducting slab is interpreted to cause arc volcanism [e.g. *Tatsumi,* 1986]. We have also indicated that a partially molten portion of the continental crust may exist beneath Aso caldera, and molten rocks in the portion might be ejected at the next caldera forming eruption. Therefore, our

results in chapters II and III should be essential evidences for revealing the processes of generation and accumulation of magma in Kyushu.

2. Overview of the processes of volcanic activity of Aso volcano

The water dehydrated from the slab is thought to decrease solidus of the mantle wedge and cause arc volcanism [e.g. *Tatsumi*, 1986]. *Nakada* [1993] analyzed trace elements of basalt erupted in the volcanoes in the Beppu-Shimabara graben, and concluded that basalt which was ejected after 5 Ma from volcanoes existing east from Kimpo volcano is contaminated by slab-derived material. *Zhao et al.* [2000] and *Honda and Nakanishi* [2003] revealed with seismic tomography that the forearc mantle beneath near the border between Oita and Miyazaki prefectures has low seismic velocity and interpreted that the forearc mantle is partially melted and causes the volcanic activity of Kuju and Aso. In this thesis, we have also obtained no evidence which indicate the PHS slab brings water just beneath Aso volcano. Therefore, fluid dehydrated from the PHS slab would move toward the backarc in the mantle wedge and reach the crust beneath Aso volcano.

The water transportation from the PHS slab to the continental crust beneath Aso caldera is interpreted as following, and the schematic interpretation of the water transportation is shown in Figure 30. The oceanic crust of the PHS slab brings water at a depth of 80 km and the water is released into the mantle wedge from the oceanic crust up to these depths. A part of the dehydrated water flows to the forearc mantle, and serpentinizes the mantle material and/or exists without combining mantle materials. If

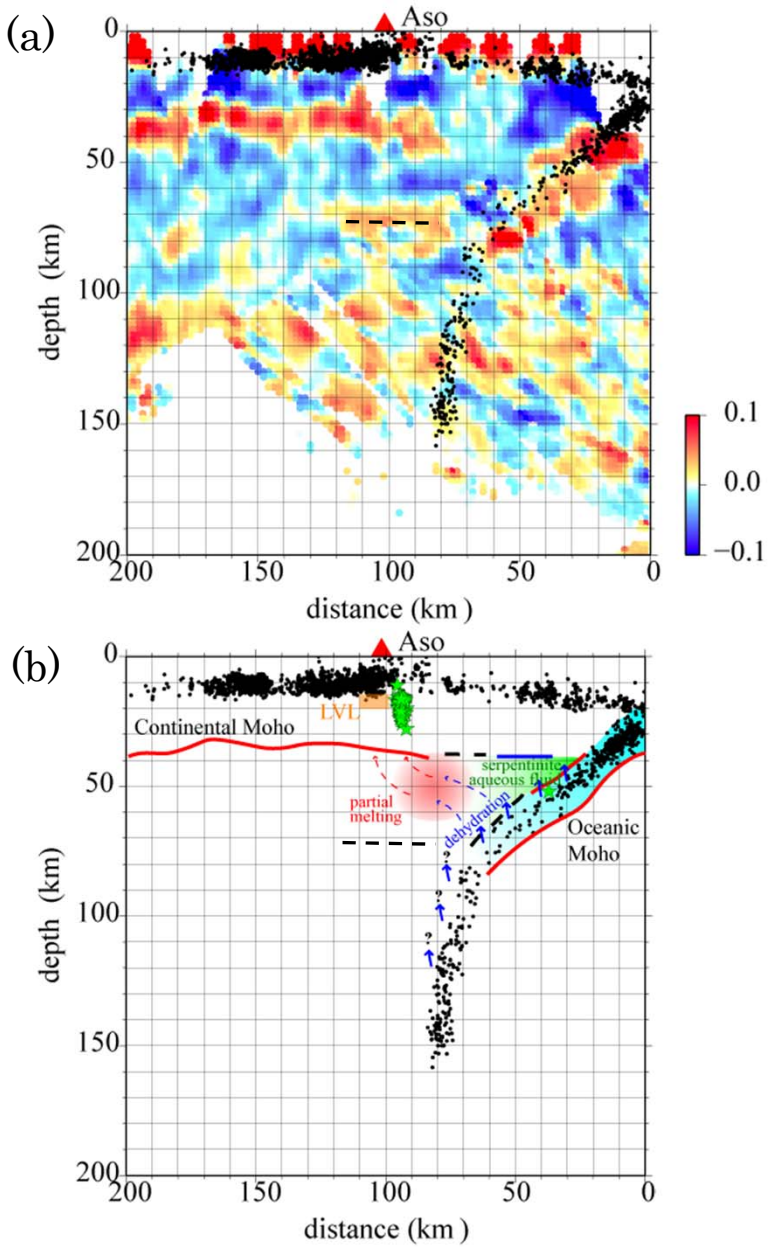

Figure 30 (a) Vectorial RF imaging along dashed line C in Figure 8. In this section, we eliminate RFs obtained from data of station ASVH and HKSH which locate in Aso caldera, because amplitudes of phases reverberated between surface and the upper boundary of LVL are large [*Abe*, 2009]. (c) Schematic interpretation of the structure beneath line C in Figure 8. Red (blue) lines indicate discontinuities with downward increasing (decreasing) velocity. The light blue area indicates the hydrated oceanic crust of the PHS slab. The green area indicates the region where serpentinized mantle and/or high pore fluid pressure would exist.

the bottom of the mantle wedge is enough cold to hydrate (<620ºC) at depths of 70-90 km, another part of the dehydrated water would combine with the mantle material and would be brought to deeper portion along the PHS slab. If the bottom of the mantle wedge is not enough cold, the water would not be brought to the deeper portion. Beneath NE Japan, *Kawakatsu and Watada* [2007] detected a discontinuity corresponding to the bottom of the serpentinized layer above the subducting Pacific plate with RFs. We do not detect such a discontinuity beneath Kyushu. The reason why we do not detect it is because such a discontinuity does not exist or cannot be detected with our analyses while it exists. *Iwamori* [2007] indicated that such a serpentinized layer would exist down to 150 km in depth beneath NE Japan where the old Pacific plate (130 Ma) is subducting while it would be dehydrated at 100 km in depth beneath North Kyushu where the young PHS plate (20 Ma) is subducting. Therefore, if the bottom of the mantle wedge shown in Figure 30 is enough cold to hydrate, the serpentinized layer constructed at the bottom of the mantle wedge would not bring water deeper than 100 km. In the mantle beneath Aso caldera, partial melting occurs due to decreasing in solidus by the dehydrated fluid and/or mantle upwelling. Whether or not the mantle upwelling is one of the cause to melt the mantle materials, the molten rocks are contaminated by the fluid dehydrated from the PHS slab. In Figure 30, positive RF peaks exist at depth of about 70 km beneath Aso caldera, and these peaks may be corresponding to the bottom of partial melting region although it is possible that they are generated by reverberation in the crust and do not correspond any discontinuity in the mantle. The melt intrudes into the continental crust and causes the low frequency earthquakes and partially melts the crustal materials. LVL would be corresponding to such a partially molten region.

3. Future works

For a deeper understanding of the processes, the following issues should be examined.

Although we have understood where the subducting oceanic crust brings water and a part of the water dehydrated from the oceanic crust would hydrate the forearc mantle, we have not completely understood how the water evolved from the oceanic crust moves toward the continental crust. In NE Japan, the bottom of the mantle wedge is interpreted to be hydrated by the evolved water and brings water deeper than the region where the water is evolved from the oceanic crust [*Kawakatsu and Watada,* 2007; *Iwamori,* 2007]. Although it is possible that the bottom of the mantle wedge brings water deeper than 100 km beneath Kyushu, we do not understand from our results whether or not such a path of water exists. The reason why we do not reveal water transportation deeper than 100 km is because resolution of our analysis is poor at these depths. To reveal the water transportation, therefore, we should collect more data by observing for longer period, or correctly estimate the depth of the Moho beneath each station and try to cancel the effect of crustal reverberations on RFs in order to reduce noise.

Okinawa trough is a backarc basin of Ryukyu subduction zone. *Tada* [1993] interpreted Beppu-Shimabara graben which transects the central part of Kyushu at ENE-WSW direction as a rift valley which extends from Okinawa trough. *Yoshida and Seno* [1992] also interpreted that volcanic activity of Aso is caused by the rifting of Beppu-Simabara graben. Therefore, we should determine whether or not the Beppu-Shimabara graben is a rift valley for better understanding of the magma genesis

of the volcanoes along the graben. The crust beneath a continental rift is thought to be thinned because of the crustal extension. For example, beneath a spreading axis in the central volcanic region in New Zealand, the depth of the Moho is estimated to be shallower than beneath the surrounding region [*Stratford and Stern*, 2006]. *Abe* [2009] estimated that the depth of the Moho beneath Aso caldera is 30-40 km, not shallower than the surrounding area. Aso caldera is not expected to exist in a rift valley from the depth of the Moho. This fact may imply that a spreading axis of the backarc basin does not reach Aso. It is important to estimate the geometry of the Moho around the Beppu-Shimabara graben west from Aso in order to verify where the spreading axis reaches.

We have estimated S-wave velocity structure of the curst beneath Aso caldera. We have detected a low S-wave velocity layer which would contain melt or aqueous fluid. We cannot determine which the low velocity layer contains, melt or aqueous fluid, and cannot estimate the amount of fluid contained in it, only from S-wave velocity structure. *Langston and Hammer* [2001] and *Mercier* [2006] suggested the method to obtain pure P-wave crustal multiples involved in teleseismic coda. If we estimate P-wave velocity anomaly of the low velocity layer using these methods, we can determine which the layer contains, melt or aqueous fluid, and can estimate the amount of the fluid.

For a better understanding of the process of huge pyroclastic eruptions, it is also important that the crustal structures beneath many calderas are revealed and compared with one another. In Figure 31, we show sections indicating standard deviations of amplitudes of 12 sets of stacked RFs (in Section 4 in Chapter II). *Abe* [2009] indicated that velocity anomaly in the crust beneath Aso caldera largely shifts the arrival times of Ps phases and generates large amplitude reverberated phases. This fact would cause

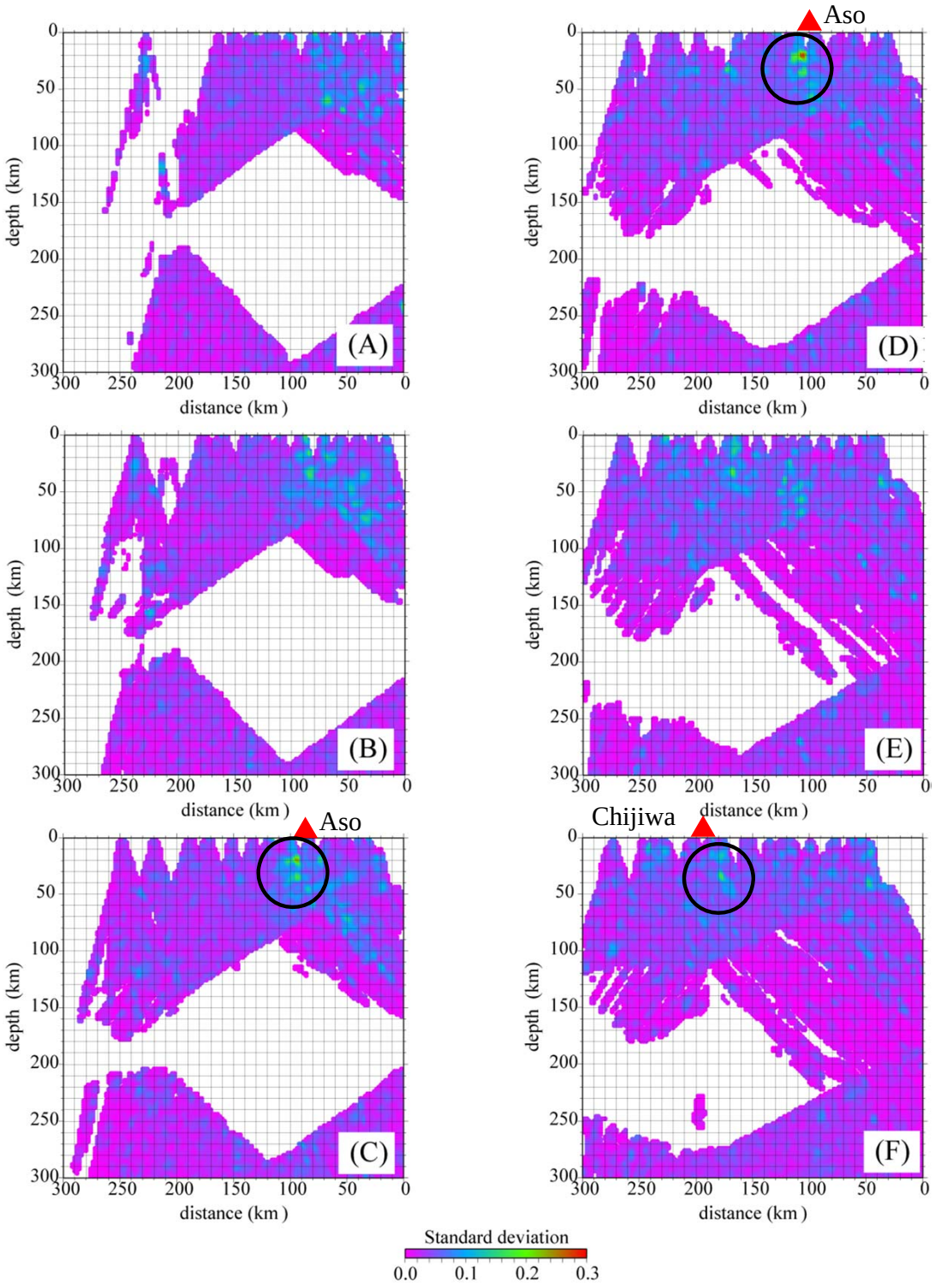

Figure 31 Standard deviations of amplitudes of the stacked RFs in Figure 13. Red triangle indicates locations of calderas and black circles indicate the area where standard deviations are high beneath the calderas.

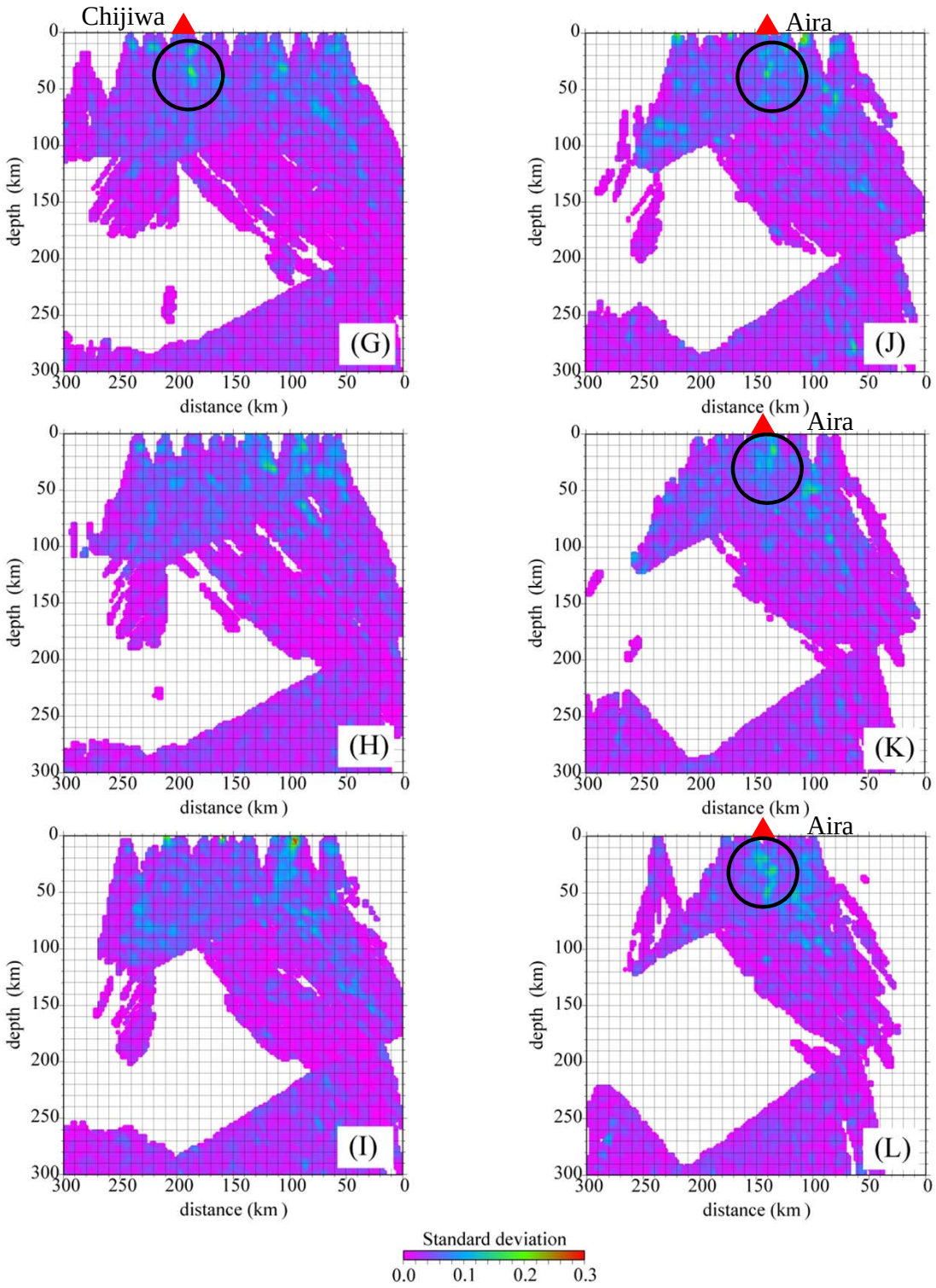

Figure 31 (Continued)

high standard deviations of RF amplitudes in the crust beneath Aso caldera (Figure 31b, c). In Figure 31, standard deviations are high in the crust beneath not only Aso caldera but also Chijiwa and Aira calderas, and it is possible that large velocity anomalies also exist beneath the calderas. Therefore, it is important to estimate the crustal structure beneath thees calderas.

Although our studies explained in this thesis contribute to revealing the process of generation and accumulation of magma in Kyushu, the process of transportation of magma (or fluid) in the mantle wedge is not well understood from our RF sections and it should also be revealed. Seismic tomography would be a useful technique to reveal the process. The portion which contains fluid is expected to have lower seismic velocity than the surround portion [*Watanabe*, 1994; *Takei*, 2002]. In NE Japan, velocity distribution of the upper mantle has been obtained with seismic tomography and the low velocity region of the mantle wedge is expected to be the pathway of the fluid [*Nakajima et al.*, 2001].

V. Conclusions

We have performed RF analyses in order to reveal the geometry of the seismic velocity discontinuities in the uppermost mantle beneath Kyushu and to estimate the crustal structure beneath Aso caldera. First, we have developed common-conversion-point stacking of RFs to estimate the geometry of dipping discontinuities. We have applied the method to observed data and revealed that the oceanic crust of the PHS slab beneath Kyushu would bring water deeper than previously revealed depth where the oceanic crust has been dehydrated, and forearc mantle wedge would be hydrated more than previously estimated and/or contain free water. We have also revealed that low S-wave velocity layer exists in the deep portion of the crust beneath Aso caldera. This layer may be a partially molten crust which generates magma, causing large eruption. These new findings are important for a better understanding of generation and accumulation of magma in Kyushu.

Citations to published works

A part of Chapter II has been published as follows:

Abe, Y., T, Ohkura, K, Hirahara, and T. Shibutani (2011), Common-conversion-point stacking of receiver functions for estimating the geometry of dipping interfaces, *Geophys. J. Int., 185,* 1305-1311, doi:10.1111/j.1365-246X.2011.05001.x.

A part of Chapter II has been accepted for publication as follows:

Abe, Y., T. Ohkura, K, Hirahara, and T. Shibutani, Water transportation through the Philippine Sea slab subducting beneath the central Kyushu region, Japan, as derived from receiver function analyses, *Geophys. Res. Lett.* in press, doi:10.1029/2011GL049688.

A part of Chapter III has been published as follows:

Abe, Y., T. Ohkura, T, Shibutani, K. Hirahara, and M. Kato (2010) Crustal structure beneath Aso Caldera, Southwest Japan, as derived from receiver function analysis, *J. Volcanol. Geotherm. Res., 195,* 1-12. doi:10.1016/j.jvolgeores.2010.05.011.

Acknowledgments

I’m grateful to Profs. Takahiro Ohkura, Kazuro Hirahara, Takuo Shibutani and Mamoru Kato for a lot of supports to my studies. I’m also grateful to Shin Yoshikawa and Hiroyuki Inoue for a lot of help for seismic observations. I’m thankful to Prof. Martha K. Savage for useful suggestions for my studies. I’m also thankful to Prof. Katsuya Kaneko for fruitful discussions about large-scale silicic volcanism.

I’m grateful to Profs. Tsuneomi Kagiyama, Keiji Takemura, Keiko Kuge, Tatsuhiko Kawamoto, Tomoyuki, Shibata, Mitsuru Utsugi, Junji Yamamoto, Masako Yoshikawa, and other researchers and students of Institute for Geothermal Sciences, Aso Volcanological Laboratory and Seismology group in Department of Geophysics for many suggestions and discussions.

I use seismic data of NIED, JMA, Kyushu University, Kagoshima University and Kyoto University, and hypocentral data of JMA. I use codes for estimating RFs, synthesizing RFs with generalized ray theory and genetic algorithm inversion of RFs coded by Prof. Takuo Shibutani. I use the multistage fast-marching code [*de Kool et al.*, 2006]. I use GMT (Generic Mapping Tools) by *Wessel and Smith* [1999] to generate figures.

References

Aoki, Y., and T. Kagiyama (2006), Crustal deformation and volcanism of the Kyushu islands, southwest Japan, *Chikyu Monthly, 28,* 98-102 (in Japanese).

Abe, Y., (2009), Crustal structure beneath Aso Caldera, Southwest Japan, as derived from receiver function analysis, *Master Thesis of Graduate School of Science, Kyoto University.*

Abers, G. A. (2005), Seismic low-velocity layer at the top of subducting slabs: observations, predictions, and systematics, *Phys. Earth Planet. Inter., 149,* 7-29.

Ando, M., T. Moriya, T. Iwasaki, T. Takeda, C. Piao, S. Sakai, T. Iidaka, A. Kubo, H. Miyamachi, K. Tashiro, T. Matsushima, and S. Suzuki (2002), Crustal structure beneath eastern Kyushu, Japan, derived from a wide-angle reflection and refraction experiment, *Bull. Earthq. Res. Inst. Univ. Tokyo, 77,* 277-285. (in Japanese with English abstract)

Ashi, J., H. Tokuyama, Y. Ujiie, and A. Taira (1999), Heat flow estimation from gas hydrate BSRs in the Nankai Trough, implications for thermal structure of the Shikoku basin, *supplement to EOS transactions, AGU, 80(46),* T12A-02

Audet, P., M. G. Bostock, N. Christensen and S. M. Peacock (2009), Seismic evidence for overpressured subducted oceanic crust and megathrust fault sealing, *Nature, 457,* 76-78.

Bostock, M. G., R. D. Hyndman, S. Rondenay, and S. M. Peacock (2002), An inverted continental Moho and serpentinization of the forearc mantle, *Nature, 417,* 536-538.

Boyd, O. S., M. K. Savage, A. F. Sheehan, and C. H. Jones (2007), Illuminating the plate interface structure beneath Cook Strait, New Zealand, with receiver functions,

J. Geophys. Res., 112, B06310.

Cassidy, J. F. (1992), Numerical experiments in broadband receiver function analysis, *Bull. Seismol. Soc. Am., 82(3),* 1453-1474.

Červený, V. (1985), The application of ray tracing to the numerical modeling of seismic wavefields in complex structures, in *Handbook of Geophysical Exploration, Seismic Shear Waves,* Vol. 15, edited by G. P. Dohr, pp. 1-124, Geophysical Press, London.

Christensen, N. I. (1989) Pore pressure, seismic velocities, and crustal structure, in *Geophysical framework of the continental United States: Geol. Soc. Am. Mem.,* vol. 172, edited by L. C. Pakiser, and W. D. Mooney, pp. 783-798, Boulder, Colorado.

Christensen, N. I. (2004), Serpentinites, peridotites, and seismology, *Int. Geol. Rev., 46,* 795-816.

Committee of Catalog of Quaternary Volcanoes in Japan (1999), Catalog of Quaternary Volcanoes in Japan. Ver. 1.0. The volcanological society of Japan, CD-ROM.

de Kool, M., N. Rawlinson, and M. Sambridge (2006), A practical grid-based method for tracking multiple refraction and reflection phases in three-dimensional heterogeneous media, *Geophys. J. Int., 167,* 253-270.

Geographical Survey Institute (2004), Crustal deformations around Aso Volcano. in *Report of Coordinating Committee for Prediction of Volcanic Eruption*, No.88, pp. 106-110. (in Japanese)

Goldberg, D. E. (1989), Genetic Algorithm in Search, Optimization, and Machine learning, Addison-Wesley, Reading, MA.

Hacker, B. R., G. A. Abers and S. M. Peacock (2003a), Subduction factory 1. Theoretical mineralogy, densities, seismic wave speeds, and H_2O contents, *J. Geophys. Res.*, 108(B1), 2029.

Hacker, B. R., S. M. Peacock, G. A. Abers and S. D. Holloway (2003b), Subduction factory 2. Arc intermediate-depth eathquakes in subducting slabs linked to metamorphic dehydration reactions?, *J. Geophys. Res., 108(B1),* 2030.

Hata, M., N. Oshiman, R. Yoshimura, Y. Tanaka, and M. Uyeshima (2011), Imaging of fluids and partial melt in the subduction zone with regional electrical resistivity structure by the network-MT data, **in** *Programme and Abstract: Volcanological Society of Japan 2011 fall meeting,* P63. (in Japanese)

Helffrich, G. (2006), Extended-time multitaper frequency domain cross-correlation receiver-function estimation, *Bull. Seismol. Soc. Am., 96(1),* 344-347, doi:10.1785/0120050098.

Helmberger, D. V. (1974), Generalized ray theory for shear dislocation, *Bull. Seismol. Soc. Am., 64(1),* 45-64.

Hilde, T. W. C., and C. Lee (1984), Origin and evolution of the west Philippine basin: a new interpretation, *Tectonophysics, 102,* 85-104.

Hirahara, K., T. Tonegawa, and T. Shibutani (2007), Gaussian-beam receiver function synthetics in a 3-D heterogeneous medium, *JpGU Meeting 2007,* S146-P001.

Hirose, F., J. Nakajima, and A. Hasegawa (2008), Three-dimensional seismic velocity structure and configuration of the Philippine Sea slab in southwestern Japan estimated by double-difference tomography, *J. Geophys. Res., 113,* B09315.

Holland, J. H. (1975), Adaptation in Natural and Artificial Systems, University of Michigan Press, Ann Arbor.

Honda, S. and I. Nakanishi (2003), Seismic tomography of the uppermost mantle beneath southwest Japan: Seismological constraints on modelling subduction and magmatism for the Philippine Sea slab, *Earth Planets Space, 55,* 443-462.

Hyndman, R. D, and S. M. Peacock (2003), Serpentinization of the forearc mantle, *Earth Planet. Sci. Lett.*, 212, 417-432.

Iwamori, H. (2007), Transportation of H_2O beneath Japan arcs and its implications for global water circulation, *Chem. Geol., 239,* 182-198.

Kaneko. K, T. Koyaguchi, and K. Furukawa (2006), Long-term evolution of magma plumbing system of Aso volcano, *Chikyu Monthly, 320, Vol.28,* 67-75. (in Japanese)

Kaneko, K., H. Kamata, T. Koyaguchi, M. Yoshikawa, and K. Furukawa (2007), Repeated large-scale eruptions from a single compositionally stratified magma chamber: An example from Aso volcano, Southwest Japan. *J. Volcanol. Geotherm. Res., 167,* 160-180.

Kaneko, K., T. Koyaguchi, and T. Takahashi (2008), Crustal processes of magmas in large-scale silicic volcanism- a review and new insights on Aso volcano-. *Chikyu Monthly,Gogai, No.60,* 187-197. (in Japanese)

Kawakatsu, H. and S. Watada (2007), Seismic evidence for deep-water transportation in the mantle, Science, 316, 1468-1471.

Kawakatsu, H., and S. Yoshioka (2011), Metastable olivine wedge and deep dry cold slab beneath southwest Japan, Earth Planet. Sci. Lett., 303, 1-10.

Kennett, B. L. N., and E. R. Engdahl (1991), Traveltimes for global earthquake location and phase identification, Geophys. J. Int., 105, 429-265.

Kennett, B. L. N, E. R. Engdahl, and R. Buland (1995), Constraints on seismic velocities in the Earth from travel times, Geophys. J. Int., 122, 108-124.

Kurita, T. (1973), Regional variations in the structure of the crust in the Central United States from P-wave spectra, *Bull. Seismol. Soc. Am., 63(5),* 1663-1687.

Langston, C. A. (1979), Structure under Mount Rainier, Washington, inferred from

teleseismic body waves, *J. Geophys. Res., 84(B9),* 4749-4762.

Langston, C. A., and J. K. Hammer (2001), The vertical component P-wave receiver function, *Bull. Seismol. Soc. Am, 91,* 1805-1819.

Matsumoto, A, K. Uto, K. Ono, and K. Watanabe (1991), K-Ar age determinations for Aso volcanic rocks-concordance with volcanostratigraohy and application to pyroclastic flows. in *Programme and Abstract: Volcanological Society of Japan,* vol.2, p.73. (in Japanese)

Matsumoto, Y. (1979), Some problems on volcanic activities and depression structures in Kyushu, Japan, *Mem. Geol. Soc. Japan., 16,* 127-139. (in Japanese with English abstract)

Mercier, J. P., M. G. Bostock, and A. M. Baig (2006) Improved Green's function for passive-source structural studies, *Geophysics, 71,* SI95-SI102.

Miyoshi, M., M. Shimono, T. Hasenaka, T. Sano, and T. Fukuoka (2008), Determination of Boron and other elements in volcanic rocks by prompt gamma-ray analysis: An application to magma genesis in Kyushu island, SW-Japan, *J. Radioanal. Nucl. Chem., 278(2),* 343-347.

Morita, Y. (1996), The characteristics of J-array seismograms, *J. Phys. Earth, 44,* 657-668.

Nakada, S., and H. kamata, (1991), Temporal change in chemistry of magma source under Central Kyushu, Southwest Japan: progressive contamination of mantle wedge, *Bull. Volcanol., 53,* 182-194.

Nakajima, J., T. Matsuzawa, A. Hasegawa, and D. Zhao (2001), Three-dimensional structure of *Vp, Vs,* and *Vp/Vs* beneath northeastern Japan: Implications for arc magmatism and fluids, *J. Geophys. Res., Vol. 106, No. B10,* 21,843-21,857.

Nakajima, J. and A. Hasegawa (2007), Subduction of the Philippine Sea plate beneath southwestern Japan: Slab geometry and its relationship to arc magmatism, *J. Geophys. Res., 112,* B08306.

Nakamura, M, S. Matsumoto, K. Uehira, and H. Shimizu (2002), Estimation of Moho discontinuity by using converted wave in seismograms of intermediate earthquakes beneath the Kyushu district, Japan, *Proceedings of meeting 13K-7, DPRI, Kyoto Univ.*, 246-255. (in Japanese with English abstract)

Nakamichi, H., H. Hamaguchi, S. Tanaka, S. Ueki, T. Nishimura, and A. Hasegawa (2003), Source mechanisms of deep and intermediate-depth low-frequency earthquakes beneath Iwate volcano, northeastern Japan. *Geophys. J. Int. 154*, 811-828.

Oda, H., and T. Ushio (2007), Topography of the Moho and Conrad discontinuities in the Kyushu district, Southwest Japan, *J. Seismol., 11,* 221-233.

Ohkura, T., and J. Oikawa (2008), GPS observation of crustal movements at Aso Volcano. in *Programme and Abstract: The Volcanological Society of Japan 2008 fall meeting*, P58. (in Japanese)

Okada, Y, K. Kasahara, S. Hori, K. Obara, S. Sekiguchi, H. Fujiwara, and A. Yamamoto, (2004), Recent progress of seismic observation networks in Japan Hi-net, F-net, K-NET and KiK-net, Earth, Planets and Space, Volume 56, p. xv-xxviii.

Okamoto, K., T. Ohkura, and T. Seno (2008), Seismicity within the Philippine Sea slab in the central and southern Kyushu, Japan, J. Seismol. Soc. Japan, No.2, 61, 77-90. (in Japanese with English abstract).

Okino, K., Y. Shimakawa, and S. Nagaoka (1994), Evolution of the Shikoku basin, J. Geomag. Geoelectr., 46, 463-479.

Park, J., and V. Levin, (2000), Receiver Functions from Multiple-Taper Spectral Correlation Estimates. *Bull. Seismol. Soc. Am., Vol. 90, No. 6,* 1507-1520.

Petford, N., A. R. Cruden, K. J. W. McCaffrey and J. L. Vigneresse (2000) Granite magma formation, transport and emplacement in the Earth's crust, *Nature, 408,* 669-673.

Research group for explosion seismology (1999a), Explosion seismic observations in eastern Kyushu, Japan I. Shonai-Kushima profile, *Bull. Earthq. Res. Inst. Univ. Tokyo, 74,* 123-140. (in Japanese with English abstract)

Research group for explosion seismology (1999b), Explosion seismic observations in eastern Kyushu, Japan II. Ajimu-Tano profile, *Bull. Earthq. Res. Inst. Univ. Tokyo, 74,* 141-160. (in Japanese with English abstract)

Rodgers, P. W., Martin A. J., M.C. Robertson, M. M. Hsu, and D. B. Harris (1995), Signal-coil calibration of electromagnetic seismometers, *Bull. Seismol. Soc. Am., Vol.85, No.3,* 845-850.

Saiga, A., S. Matsumoto, K. Uehira, T. Matsushima, and H. Shimizu (2010), Velocity structure in the crust beneath the Kyushu area, *Earth Planet Space, 58,* 1-12.

Sekiguchi, S. (1992), Amplitude distribution of seismic waves for laterally heterogeneous structures including a subducting slab, *Geophys. J. Int., 111,* 448-464.

Seno, T., S. Stein, and A. E. Gripp (1993), A model for the motion of the Philippine Sea plate consistent with NUVEL-1 and geological data, *J. Geophys. Res., 98(B10),* 17941-17948.

Sheehan, A. F., P. M. Shearer, H. J. Gilbert, and K. G. Dueker (2000) Seismic migration processing of P-SV converted phases for mantle discontinuity structure beneath the Snake River Plain, western United States, *J. Geophys. Res., 105(B8),*

19,055-19,065.

Shibutani T., M. Sambridge, and B. Kennett (1996), Genetic algorithm inversion for receiver functions with application to crust and uppermost mantle structure beneath Eastern Australia, *Geophys. Res. Lett, 23, No.14,* 1829-1832.

Shibutani, T., T. Ueno and K. Hirahara, (2008), Improvement in the extended-time multitaper receiver function estimation technique, *Bull. Seismol. Soc. Am., 98(2),* 812-816, doi:10.1785/0120070226.

Shiomi, K., M. Matsubara, Y. Ito, and K. Obara (2008), Simple relationship between seismic activity along Philippine Sea slab and geometry of oceanic Moho beneath southwest Japan, *Geophys. J. Int., 173,* 1018-1029.

Sodoudi, F., X. Yuan, G. Asch, and R. Kind (2011), High-resolution image of the geometry and thickness of the subducting Nazca lithosphere beneath northern Chile, *J. Geophys. Res., 116,* B04302.

Stratford, W. R, and T. A. Stern (2006), Crust and upper mantle structure of a continental backarc: central North Island, New Zealand, *Geophys. J. Int., 166,* 469-484.

Sudo, Y., L. S. L. Kong (2001), Three-dimensional seismic velocity structure beneath Aso Volcano, Kyushu, Japan. *Bull. Volcanol., 63,* 326-344.

Sudo, Y., T. Tsutsui, M. Nakaboh, M. Yoshikawa, S. Yoshikawa, and H. Inoue, (2006), Ground Deformation and Magma Reservoir at Aso Volcano: Location of Deflation Source Derived from Long-term Geodetic Surveys. *Bull. Volcanol. Soc. Japan 51,* 291-305. (in Japanese with English abstract)

Tada, T. (1993), Crustal deformation in central Kyushu, Japan and its tectonic implication –Rifting and spreading of the Beppu-Shimabara graben-, *Mem. Geol.*

Soc. Japan., 41, 1-12. (in Japanese with English abstract)

Tahara, M, K. Uehira, H. Shimizu, M. Nakada, T. Yamada, K. Mochizuki, M. Shinohara, M. Nishino, R. Hino, H. Yakiwara, H. Miyamachi, K. Umakoshi, M. Goda, N. Matsuwo, and T. Kanazawa (2008), Seismic velocity structure around the Hyganada region, southwest Japan, derived from seismic tomography using land and OBS data and its implications for interplate coupling and vertical crustal uplift, *Phys. Earth Planet. Inter., 167,* 19-33.

Takahashi, M. (1995), Large-volume felsic volcanism and crustal strain rate, *Bull. Volcanol. Soc. Japan, 40,* 33-42. (in Japanese with English abstract)

Takahashi, M. (2008), Magmatic system of the super caldera volcano, *Chikyu Monthly Gogai, No. 60,* 134-140. (in Japanese)

Takei, Y. (2002), Effect of pore geometry on V_P/V_S: From equilibrium geometry to crack, *J. Geophys. Res., 107(B2),* 2043.

Tatsumi, Y. (1986), Formation of the volcanic front in subduction zones, *Geophys. Res. Lett., Vol.13, No.8,* 717-720.

Ukawa, M. and M. Ohtake (1987), A monochromatic earthquake suggesting deepseated magmatic activity beneath the Izu-Ooshima volcano, Japan. *J. Geophys. Res., 92,* 12649-12663.

Wang, Z., and D. Zhao (2006), Vp and Vs tomography of Kyushu, Japan: New insight into arc magmatism and forearc seismotectonics, *Phys. Earth Planet. Inter., 157,* 269-285.

Watanabe, T. (1994), Melt beneath volcanoes –Inference from seismic velocities-, *Mem. Geol. Soc. Japan, No. 43,* 20-31. (in Japanese with English abstract)

Wessel, P. and W. H. F. Smith (1999), Free software helps maps and display data, *Abst.*

EOS, trans., AGU, 72, 445-446.

Xia, S., D. Zhao, and X. Qiu (2008), Tomographic evidence for the subducting oceanic crust and forearc mantle serpentinization under Kyushu, Japan, *Tectonophysics, 449,* 85-96.

Yagi, Y., and M. Kikuchi (2003), Partitioning between seismogenic and aseismic slip as highlighted from slow slip events in Hyuga-nada, Japan, *Geophys. Res. Lett., 30(2),* 1087.

Yamasaki, T. and T. Seno (2003), Double seismic zone and dehydration embrittlement of the subducting slab, *J. Geophys. Res., (108)B4,* 2212.

Yoshida, A. and T. Seno (1992), Tectonic origin of the Aso volcano, *Bull. Volcanol. Soc. Japan, Vol. 37, No. 6,* 297-301. (in Japanese with English abstract)

Yoshioka, S., M. Toda, and J. Nakajima (2008), Regionality of deep low-frequency earthquakes associated with subduction of the Philippine Sea plate along the Nankai Trough, southwest Japan, *Earth Planet. Sci. Lett., 272,* 189-198.

Yuan, X., S. V. Sobolev, R. Kind, O. Oncken, G. Bock, G. Asch, B. Schurr, F. Graeber, A. Rudloff, W. Hanka, K. Wylegalla, R. Tibi, Ch. Haberland, A. Rietbrock, P. Giese, P. Wigger, P. Rower, G. Zandt, S. Beck, T. Wallace, M. Pardo and D. Comte (2000), Subduction and collision processes in the Central Andes constrained by converted seismic phases, *Nature, 408,* 958--961.

Zhao, D., K. Asamori, and H. Iwamori (2000), Seismic structure and magmatism of the young Kyushu subduction zone, *Geophys. Res. Lett., Vol. 27, No. 14,* 2057-2060.